Backward erosion piping

Experiments on erosion and progression rate

W.F. van Klaveren

MSc Civil Engineering: Hydraulic Engineering (Master Thesis)

February 2020

TU Delft

Source photograph cover: Kennisplatform Dijkmonitoring, Livedijk Utrecht

Backward erosion piping:

Experiments on erosion and progression rate

By

W. F. van Klaveren

in partial fulfilment of the requirements for the degree of

Master of Science
in Civil Engineering

at the Delft University of Technology,

to be defended publicly on Friday, February 21, 2020, at 15:00 AM.

Supervisor:	Prof. dr. ir. S.N. Jonkman,	TU Delft
Thesis committee:	ir. J.C. Pol,	TU Delft
	dr. ir. Erik Mosselman	TU Delft

An electronic version of this thesis is available at http://repository.tudelft.nl/.

TU Delft

Preface

Hereby, I present my thesis for the Master Hydraulic Engineering at the Delft University of Technology. For the past nine months, I have been working on this thesis of which I spent six months in the geotechnical laboratory of Deltares. After the experiments in the laboratory, I finalised my thesis at Delft University of Technology where I focused on the analysis and writing this report. This Master thesis was the last part of my Master and I look back with gratitude for this opportunity.

First of all, I would like to thank my first supervisor Joost Pol for his patience and guidance during this thesis. I believe that during our cooperation, we made a difference by performing the experiments and processing the results. I hope that my assistance during his PhD project was of great help and wish him all the best.

Secondly, I would like to thank the rest of the committee for the critical views on the report and the discussions regarding the theory and observations. The committee meetings were very valuable and helped a lot in the process of this thesis. The planning was sometimes tight, but also necessary to go forward.

Furthermore, I would like to thank all the people from Deltares for the support and expertise during the experiments. It was very exciting to discover all the facilities in the laboratory and implementing this during the performing of the experiments. Many technical challenges were overcome while conducting the experiments.

Finally, I would like to thank my friends and family for the support during this chapter of my life. A special thanks to my parents for giving me the strength to complete this study.

Wouter van Klaveren

Delft, February 2020

Abstract

Backward erosion piping is a form of internal erosion where small pipes are formed below a dike. These pipes are formed in a direction opposite to the flow that transports sand particles. Piping is a very important failure mechanism in the protection of dikes, which can be unpredictable due to the different soil characteristics.

Piping is well managed in the Netherlands, but there is a lot to be discovered regarding the erosion processes inside the pipe. For example, how fast the pipe develops and what this is dependent on. The objective of this thesis is to monitor and study the development of the pipe, to extend the knowledge about the different processes that influence the progression rate of the pipe. The main research question is: *How do the different parameters and processes influence the progression and the sediment transport rate in laboratory experiments of backward erosion piping?*

To monitor the development of the pipe, different small-scale laboratory experiments were performed to obtain new data regarding piping and to study the influences of different parameters. The piping experiments were performed in three series: (1) configuration of the setup, (2) effect of grain size and (3) hydraulic loading. These experiments were performed in the previously developed setup of Vera van Beek (Van Beek, 2015). This setup was modified to measure the pore pressures and to guide the pipe through the middle of the setup. While conducting the experiments, different measurements were performed. This included measuring of the pipe length and geometry, collecting the sand boil and a dye injection to follow the flow.

The literature study performed for this thesis has shown that in the past many experiments were performed regarding piping, but these studies did not focus on the different processes and the sediment transport rate of the pipe. By focussing on the progression phase of the pipe (continuous transport), the experimental data is compared to existing models (primary and secondary erosion).

Sellmeijer's model (Förster et al., 2012) is the current rule that is applied in the Netherlands for dike safety, but this model does not include time-dependency. This research showed that the development of the pipe is not a stationary process but depends on various conditions, such as soil characteristics. The hypothesis formed at the beginning of this thesis listed several soil parameters which influence the progression rate of the pipe.

Concerning the sediment transport rate of the pipe, Cheng's model for bedload transport (Cheng, 2004) is evaluated and compared with the measured results. The analysis showed that the adapted formula of Cheng (Equation 2.24) overestimates the sediment transport rate in the pipe.

From the analysis of the experimental results, it can be concluded that two parameters play an important role in the progression and sediment transport rate of the pipe: the particle diameter and hydraulic permeability. These parameters showed an influence on the progression rate which can be used to study piping on a larger scale. The most interesting result is the fact that experiments with a larger particle diameter have an overall larger progression rate.

Contents

1. Introduction 1
1.1 Research introduction 1
1.2 Research objective 2
1.3 Research questions 2
1.4 Methodology 3
1.5 Research approach and strategy 4
1.6 Analyses and presentation of the results 5
2. Literature review 6
2.1 Overview of failure mechanisms 6
2.1.1 Piping phases 7
2.1.1.1 Phase 1: Seepage 8
2.1.1.2 Phase 2: Backward erosion 8
2.1.1.3 Phase 3: Widening of the pipe 8
2.1.1.4 Phase 4 and 5: Dike failure and breaching 9
2.1.2 Piping in the Netherlands 10
2.1.3 Piping models 11
2.1.3.1 Bligh 11
2.1.3.2 Lane 13
2.1.3.3 Sellmeijer 14
2.2 Overview of performed experiments 16
2.2.1 Experiments performed by Robbins (2017) 17
2.2.2 Experiments performed by Allan (2018) 19
2.2.3 Experiments performed by Vandenboer (2018) 21
2.2.4 Summary of available experiments 23
2.3 Sediment transport in piping 23
2.3.1 Equilibrium of forces 24
2.3.1.1 Shields parameter (1936) 25
2.3.1.2 White (1940) 27
2.3.2 Incipient motion in laminar flows 29
2.3.3 Transport mechanisms 30
2.3.4 Dilatancy 32
2.3.5 Sediment transport model 32
2.3.5.1 Cheng (2004) 32
2.4 Hypothesis 34

2.4.1 Parameters of influence 35
2.4.2 Equations for the progression and sediment transport rate 37
3. Experimental setup 39
3.1 Experimental setup 39
3.2 Sample preparation 41
3.3 Testing procedure 45
3.3.1 Soil sample 46
3.3.2 Configuration of the setup 47
3.3.3 Procedure of the reference test (B25-229) 48
3.4 Results of the reference test (B25-229) 49
3.4.1 Results of the pressure sensors (B25-229 and B25-232) 50
3.4.2 Results of the depth measurements (B25-229) 53
3.4.3 Dye injection (B25-229) 54
3.4.4 Collecting the sand boil (B25-229) 55
3.5 Implications of the experiments 57
4. Results and Analysis 58
4.1 Strategy of the analysis 58
4.2 Experimental results 59
4.2.1 Graphical presentation of the results 61
4.2.2 Calculation of the critical head (Sellmeijer) 64
4.2.3 Mass of the sand boil 65
4.3 Analysis of experiment FPH-235 66
4.3.1 Sediment transport rate of Experiment FPH 235 66
4.3.2 Primary erosion experiment FPH-235 67
4.3.3 Results of the bed shear stress of experiment FPH-235 69
4.3.4 Sediment transport rate experiment FPH-235 (Cheng, 2004) 71
4.3.5 Dilatancy results (Experiment FPH-235) 74
4.4 Comparison of the results with the hypothesis 76
5. Discussion 79
5.1 Limitations of this research 79
5.2 Applied models 79
5.3. Application of the progression rate related to a real dike 80
6. Conclusion 82
6.1 Answers to sub-research questions 82
6.2 Main research question 83
6.3 Recommendations 84
6.3.1 Formula to predict the progression rate 84

6.3.2 Medium-scale experiments 85
6.3.3 Experimental proposal small-scale experiments 86
Bibliography 87
Appendix A – Piping checklist 90
Appendix B – Sieve curve 92
B1. Baskarp B25 92
B2. FPH and FS35 sand 93
Appendix C – Reference experiment B25-229 94
C1. Observations experiment B25-229 94
C2. Results of the reference experiment B25-229 95
Appendix D – ΔH_c Sellmeijer calculation 98
D1. ΔH_c Sellmeijer (1) 99
D2. ΔH_c Sellmeijer (2) 100
Appendix E – Calculation of the crater mass 101
Appendix F – Observation sheet Experiment FPH – 235 103
Appendix G – Gradients of Experiment FPH – 235 104
G1. Measured data regarding the Shields parameter (Experiment FPH-235) 104
G2. Passing gradients for the dilatancy calculation (FPH-235) 105
List of symbols 108
List of figures 110
List of tables 113

1. Introduction

1.1 Research introduction

Piping is one of the most important failure mechanisms for the protection of dikes and embankments. Piping occurs as the result of a difference in water level on the inner and outer side of the defense. A schematic overview is given in the figure below.

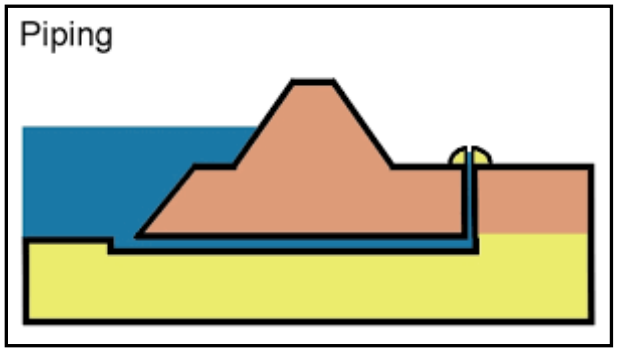

Figure 1.1: Overview of the piping mechanism.

Piping begins with seepage of water underneath the dike. When the pressure in the sand layer increases, the clay layer on the side of the hinterland will lift and eventually crack. The result of this is the forming of a well. This is shown on the right side of the dike in Figure 1.1.

As the time and the internal erosion of the pipe further proceed, a fully developed pipe under the dike is obtained. The outcome is the total failure of the dike. If the dike protects a major city or an important part of a polder the consequences are larger.

In this thesis, it is the task and objective to research the effects of time dependence on dike safety. Time dependence can be characterized in 3 components: hydraulic load, pore pressure response and the growth of the pipe. The main focus of this research is the growth of the pipe. Currently, there is a time-dependent numerical model (Rotunno et al., 2017) which calculates the erosion, but this model has not been well validated.

Sellmeijer's model (Förster et al., 2012) is a stationary model which is used in the Netherlands for dike safety. This model does not predict the time scale of the pipe growth. For a correct prediction of the temporal development of piping in dikes, a complex model is required. But before more complex models can be applied more research should be performed on the piping process itself to understand the processes based on hydraulic loads and soil properties.

1.2 Research objective

The main objective is the assessment of the erosion process and progression rate in the pipe under a dike. Several small-scale experiments are performed at the laboratory of Deltares for the assessment of this problem.

Sellmeijer's model (Förster et al., 2012) is a stationary model. In a real high-water situation Sellmeijer's model is not completely representative since high water can be maintained for days. Therefore, the time-dependent influences on the processes of piping and erosion have been researched insufficiently (Förster et al., 2012).

The expected outcome in this research would be a quantitative conclusion about the progression rate in the pipe. This could be used to study on a more general level the influences of the dike geometry, soil properties and loading on the progression rates.

In the future, this must lead to a more simplified model which includes the time dependence effects for dike safety.

1.3 Research questions

The overall research question for this thesis project is:

The assessment of the erosion process and the progression rate under a dike. *How do the different parameters and processes influence the progression and the sediment transport rate in laboratory experiments of backward erosion piping?*

To answer the overall research question, sub-objectives are formed. The sub-questions are summed up below:

- *Which experiments have already been performed concerning the progression rate of piping?*
- *How can the erosion process and the flow conditions be determined in the laboratory setup (adjusted setup of Van Beek)?*
- *How can the progression rate be modelled?*

A literature study and discussions with experts in the field are conducted to see whether a connection can be made to the progression rate of piping in backward erosion piping laboratory experiments. If not, a model or experimental research should be performed to obtain results and find relations for the different parameters concerning piping.

The research thus focuses on quantification and the assessment of the sediment and progression rate, but also the benefits of implementing the results in combination with time dependence on dike safety.

1.4 Methodology

The methodology for this thesis is divided into five different phases to answer the main research question. The phases are a literature review, experimental setup, results and analysis of the data, discussion and conclusion. Figure 1.2 shows a schematized overview of the different phases.

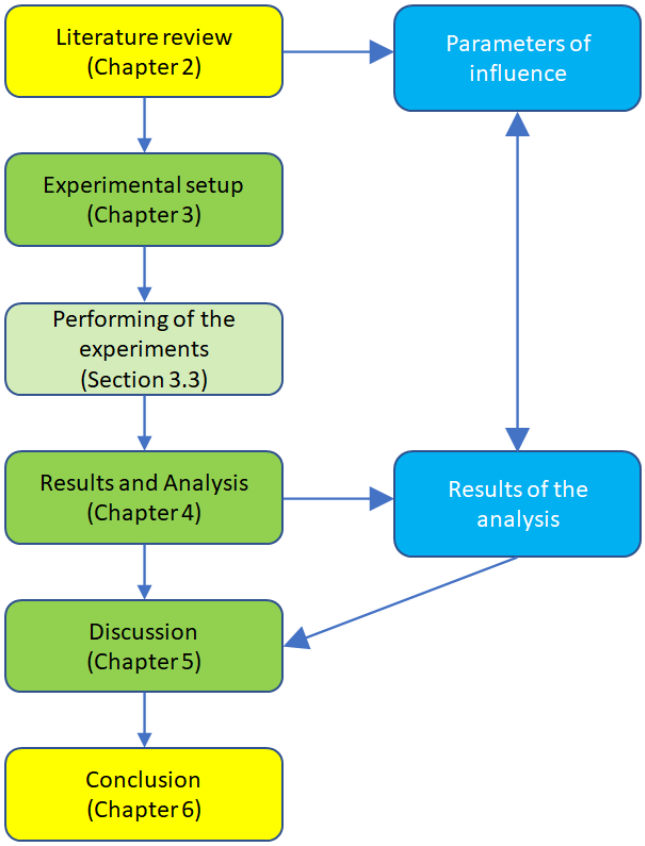

Figure 1.2: Overview of the methodology.

First, a literature study is performed for a better understanding of the topic. The literature study provides insights into the piping mechanism, formerly performed experiments and the different parameters which play an important role. Another part of the literature study is the study of sediment transport in the pipe. This is necessary to assess which parameters are important for the progression and the sediment transport rate inside the pipe. At the end of this chapter, a hypothesis is formulated with knowledge from the literature study.

When the literature study is completed, the series of experiments can be performed. In this chapter, it is described which and how the different experiments are executed. Therefore, a description of the setup is followed by an overview of the experimental series and the characteristic results of a reference experiment (B25-229).

In the next phase, all experimental results are presented and analysed. This phase is one of the most important ones to understand the problem and see which correlations can be made between the different parameters and their influences on the progression rate. Also, are the results compared to the hypothesis which is made at the beginning of the project (chapter 2).

The discussion focusses on the results from the data analysis and the applied models. The discussion also evaluates the method and limitations of this thesis.

The answers to the sub-questions and main question are presented in the last chapter. Additionally, multiple recommendations for further investigation are drawn.

1.5 Research approach and strategy

The research approach consists of different steps. First, the topic of experimental research on piping processes was selected, from here the research approach could be formed.

The research approach uses the following steps:

- Literature study: Books, papers, articles regarding piping, failure of dikes due to piping, modelling of backward erosion piping including small-scale experiments and sediment transport (laminar flow).
- Schedule meetings with experts: regarding people who work within the field of experimental research of piping. To find more information about the topic and to answer the first sub-question.
- Formulate a hypothesis: Before the start of the experiments, it is required to formulate a hypothesis, which explains the progression rate.
- The experimental research is completed at Deltares where the laboratory tests are performed during a period of six months.
- During the experimental tests, data is collected and processed to answer the different research questions. In the experiments gradients (ΔH/L), pressures, velocities, dimensions of the pipe and the hydraulic conductivity are measured. This information is analysed with different plots and fit functions. By this approach, relations were found for the different parameters regarding the progression rate.

Strategy of the experiments

To quantify the progression rate of the pipe three series of lab experiments are performed. An overview of the different series is given in Figure 1.3.

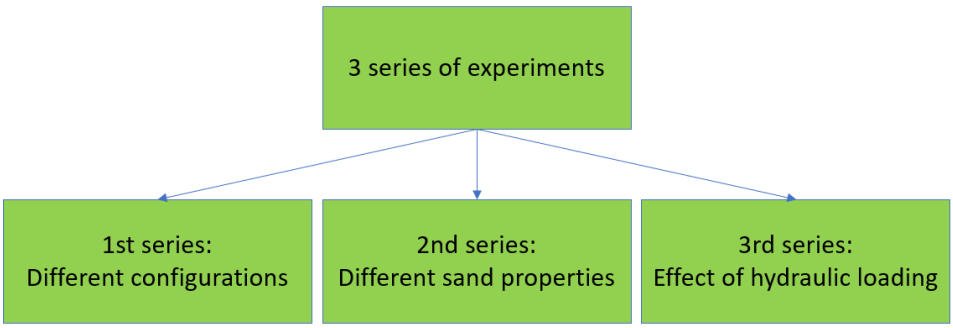

Figure 1.3: Flowchart of the different experimental series.

The first series of experiments focuses on the comparison of different setups. Changing the configurations and comparing this to the available experimental data presents the effects of the different setups. For the second series, the effects of the sand properties are studied. This is

done by adapting the grain size and relative density. These parameters have been chosen because in existing models, these parameters play an important role.

For the last series of tests, the strategy is to quantify the effect of local gradients on the progression rate. With this approach, the different phases during a flood event can be simulated. For example, applying an instant hydraulic load or a stepwise increase of the hydraulic head difference.

1.6 Analyses and presentation of the results

The results of this research are compared to simple models made in the beginning to find several correlations between the different configurations during the laboratory tests. One of the main goals is to research which processes can explain the progression rate.

The computational software MATLAB is used to obtain quantitative results from the several experiments and compared. These results are processed, analysed and compared to the hypothesis. The results from the laboratory experiments may correspond to the theoretical model, but this does not mean necessarily that the experiments were performed correctly or that the theory matches the practice. There is always room for optimization or improvement. This is written in the last chapters as a discussion point.

The expected outcome is a conclusion about the quantity of the progression rate in the pipe. The results obtained and analysed with the use of MATLAB are presented in graphs and tables with corresponding legends. With this method, the results are clearly presented and show how the different parameters influence the progression rate.

As an external validation, the results were monitored by the laboratory experts from Deltares and people who work on a daily basis with the modelling of piping.

2. Literature review

This literature research is based on the knowledge of the different performed experiments and the theory behind piping and sediment transport. Therefore, a distinction is made in the literature between the different performed experiments, the theory behind the piping processes and the relation with sediment transport.

In the literature study, the analysis of three different topics is made:

- Analysis of the failure mechanism itself and the required local conditions (soil parameters)
- Analysis of the different performed experiments regarding the modelling of piping
- Analysis of the experiments and theory concerning sediment transport (laminar flow) for piping modelling

For the last part of the literature study, a hypothesis is formulated related to the parameters that influence the progression and sediment transport rate.

2.1 Overview of failure mechanisms

As already mentioned in the last chapter, piping is one of the most important failure mechanisms for dikes and levees. A dike can fail due to different mechanisms. If a dike is not fulfilling the water-retaining function anymore it is termed as failure. In Figure 2.1 the different failure mechanisms are schematized. This thesis focuses on the piping failure mechanism.

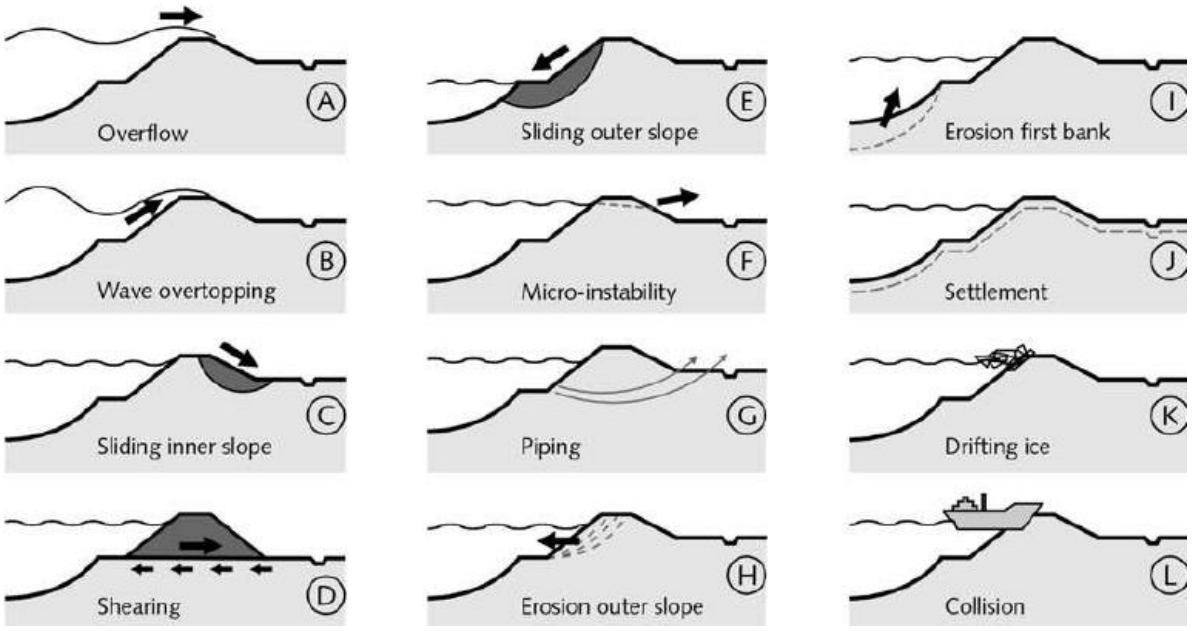

Figure 2.1: Schematic overview of the most common failure mechanisms (TAW, 1998).

2.1.1 Piping phases

Piping or backward erosion is a process where channels (pipes) are formed below the dike. It consists of an internal erosion mechanism, which is transporting sandy material in the opposite flow direction. Once piping is initiated due to high waters, sand boils are present on the lower side of the dike. These sand boils indicate the presence of piping (Figure 2.2).

Figure 2.2: Sand boil in a ditch (TAW, 1994).

Piping is a process which has different phases (Van Beek, 2015). Before a dike fails due to piping, several phases have to be completed. Figure 2.3 shows the different phases of piping.

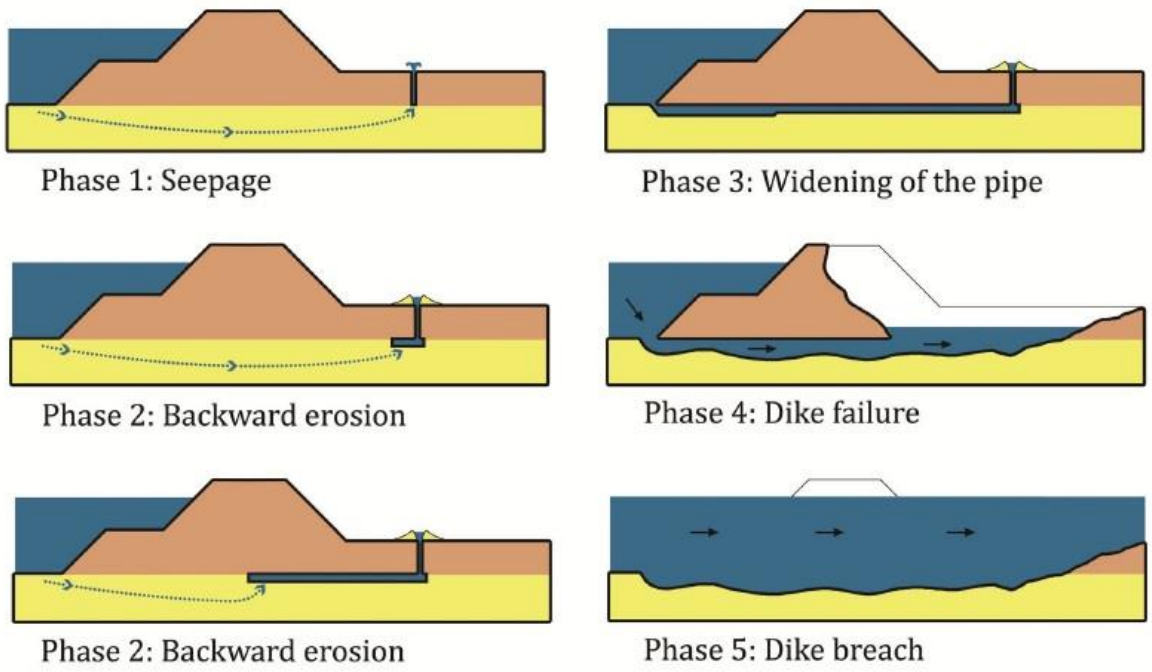

Figure 2.3: The different phases of piping (Van Beek, 2015).

2.1.1.1 Phase 1: Seepage

In the first phase of the piping, the phenomenon seepage occurs. Seepage is the start of piping and occurs due to the head difference between the high-water side and the low water side (hinterland). The groundwater starts flowing from the sandy aquifer through the blanket layer on top (light brown layer). In the beginning, the top layer has enough resistance to prevent an outflow of water, but when the overpressure is sufficient an exit point is formed.

2.1.1.2 Phase 2: Backward erosion

When the opening is formed in phase 1, there is an opening for sand particles to flow out. In this phase upward forces are formed on the sand particles near the exit due to the hydraulic gradient. Once particles start to pile up in the surroundings of the exit point, it is considered that piping is initiated (Vandenboer, 2018). The sand boils are formed by soil particles which are transported by flow. If the flow is high enough soil particles are push out and sand boils occur (Figure 2.4 (r)). This is the situation when the hydraulic gradient is larger than the critical gradient. While the water level drops on the higher side of the dike, the gradient is smaller than the critical gradient. In this situation, the flow velocity drops and the sand boils are not increasing in size (diameter), but there is still a flow of 'clean' water (Figure 2.4 (l)). See Figure 2.4 for the two types of sand boils.

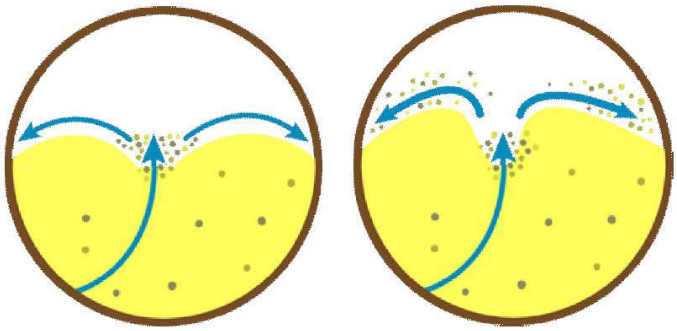

Figure 2.4: Sand boil without soil particles (l), Sand boil with soil particles (r) (Vandenboer, 2018).

Once the erosion process develops and more particles are eroded (Figure 2.4 (r)), shallow pipes are formed in the upstream direction. This is called the progression phase. These two phases, initiation and progression are the two main elements of backward erosion piping.

2.1.1.3 Phase 3: Widening of the pipe

In the third phase, the pipe continues to grow until it reaches the outer water level. Compared to phase 2, the pipe is more widened now and forms a direct connection between the up and downstream side of the dike. Between phase 2 and 3, the pipe continues to grow due to an adequate head difference between the high and low water levels. When it arrives at the third phase a direct connection is formed, and the pipe is completely developed. An effect of the fully developed pipe is an increase in the flow velocity. After the pipe reached the higher water level there is a drastic increase in the flow velocity due to the loss of the hydraulic resistance (Jonkman, Jorissen, & Schweckendieck, 2017).

2.1.1.4 Phase 4 and 5: Dike failure and breaching

From the moment the pipe is fully developed, transportation of water and erosion is enabled, which results in further deepening and widening of the pipe. After a certain moment in time, the pipe reaches to unbridgeable dimensions which results in partial collapse and failure (Vandenboer, 2018).

When a dike breaches there is a forceful flow of sand, mud (fountains) and water. This flow of water is accompanied by cracks in the dike and subsidence (Van Beek et al., 2011). The period from the transport of sediment until the moment of failure can be as short as 20 minutes but can also take a few days. This is related to the widening of the pipe and settlements which causes the pipe to close.

The abrupt transformation from seepage and sand boils to a dike breach shows the importance of the failure mechanism piping. Figure 2.5 displays a dike breach during a full-scale experiment (Van Beek et al., 2011).

Figure 2.5: Dike breach in the IJkdijk experiments (Van Beek et al., 2011).

2.1.2 Piping in the Netherlands

Piping is a process which has been observed in the Netherlands for many years. The combination of high-water levels and heavy precipitation fosters the development of piping. During high waters in the Dutch rivers (such as the Rijn, the Waal, the Ijssel and the Maas), many observations of sand boils were reported. However, the last dike breach was almost 100 years ago (Förster et al., 2012).

Overview of the last dike breaches due to piping:

- Dijkdoorbraak van de Heidijk te Nieuwkuijk (1880);
- Dijkdoorbraak polder Nieuw-Strijen te Tholen (1894);
- Dijkdoorbraak te Zalk (1926).

Figure 2.6: The mud fountain as observed at the location of the sand boil, Zalk 1926 (Van Beek et al, 2011).

When piping is detected, measures are often taken to prevent further development of the pipes. Although the effects of piping are manageable, the causes of piping remain unclear, as demonstrated in the studies conducted by TAW (1999) (Förster et al., 2012). During this research, the sand boils of several dikes could not be verified through piping simulations.

Figure 2.7 gives an overview of the observed sand boils in the past. The map shows that most of the sand boils were found in river areas of the Netherlands.

Figure 2.7: Observations of piping boils in the Netherlands (Zwang & Bos, 2009).

2.1.3 Piping models

During the years of experiencing the failure mechanism piping, different types of models were developed to assess the safety of dikes. In the following sections, an overview is given of the most common models which are used to assess and prevent piping.

2.1.3.1 Bligh

Bligh was a British engineer from the Royal Navy who developed one of the first piping models in the year 1910. Bligh's piping model was based on the failure of different weirs in India. These weirs were built on a shallow foundation (Förster et al., 2012). Bligh listed the several failure cases and the following empirical rule was derived:

$$\Delta H \leq \Delta H_c = \frac{L}{C_{Bligh}} \tag{2.1}$$

With:

ΔH = Head difference
ΔH_c = Critical head difference (maximum hydraulic load for which the weir is stable)
L = Seepage length (length of the erosion path)
C_{Bligh} = Bligh factor (depending on the material)

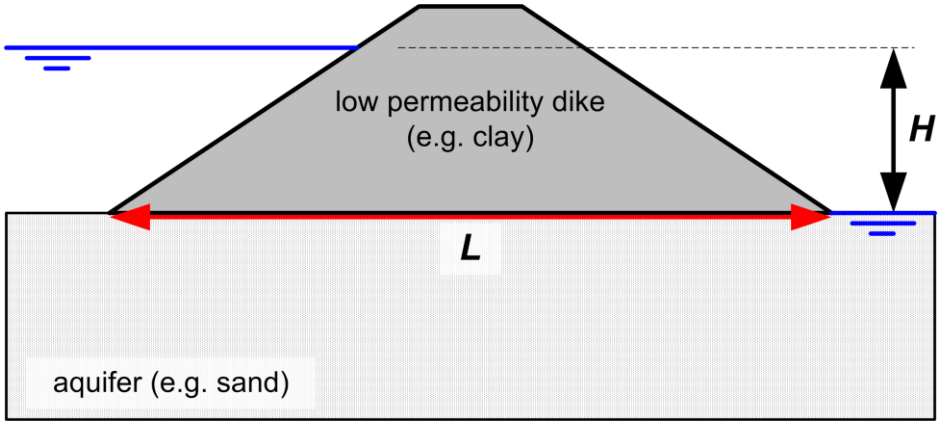

Figure 2.8: Schematization of Bligh's rule (Jonkman et al., 2017).

The Bligh factor is also called the percolation factor, which means the amount of filtration. Table 2.1 gives an overview of the different factors (percolations) and the type of foundation material.

Type of foundation	**C_{Bligh}**
Fine silty sand	18
Moderate fine sand	15
Coarse sand	12
Fine gravel	9
Coarse gravel	4

Table 2.1: C_{Bligh} factor related to foundation material (Vandenboer, 2018).

The table shows that a coarser foundation has a lower C_{bligh} factor. A lower C_{Bligh} factor is more preferred to prevent piping.

From the empirical rule (1) a global factor of safety was formed. The global safety factor is defined as:

$$F = \frac{\Delta H_c}{\Delta H} \tag{2.2}$$

The safety factor increases by a lower C_{bligh} factor (increase in grain size) or by a larger seepage length (Vandenboer, 2018). Literature study showed that Bligh's model formed the basis for further models regarding the assessment and safety of piping already at the beginning of the 20th century.

2.1.3.2 Lane

In 1935 Lane formulated a new piping model which was related to the empirical relation of Bligh. Lane adapted Bligh's empirical rule to consider vertical flow lines as well. This resulted in the following equation:

$$\Delta H \leq \Delta H_c = \frac{\frac{1}{3} * L_h + L_v}{C_{Lane}} \tag{2.3}$$

With:

ΔH =	Head difference
ΔH_c =	Critical head difference (maximum hydraulic load for which the weir is stable)
L_h , L_v =	Seepage length (length of the erosion path vertical or horizontal)
C_{Lane} =	Bligh factor (depending on the material)

The vertical seepage length (L_v) is the total length of the vertical flow. In Figure 2.9 a schematization is given of a hydraulic structure on a sandy foundation. To prevent piping and increase the seepage length, seepage screens (in Dutch: 'kwelschermen') are used. The vertical seepage length is calculated by two times the length of the seepage screen (line of creep).

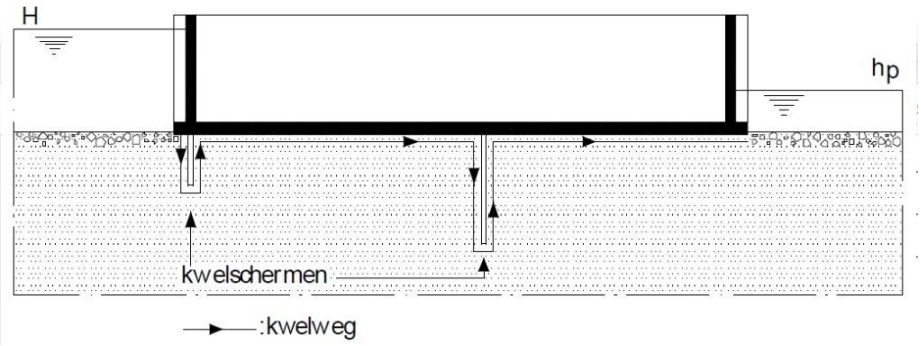

Figure 2.9: Schematization of Lane's rule (Förster et al., 2012).

Lane also used a percolation factor based on the type of foundation. In Table 2.2 an overview is given of the different factors (percolations) and the type of foundation material.

Type of foundation	C_{Lane}
Fine silty sand	8.5
Moderate fine sand	7
Coarse sand	5
Fine gravel	4
Coarse gravel	3

Table 2.2: C_{Lane} factor related to foundation material (Vandenboer, 2018).

If there is no vertical seepage, C_{Lane} should be 1/3 of C_{Bligh} however, in Table 2.2 it can be observed that the values for C_{lane} are higher than 1/3 of the values in Table 2.1. This shows that Lane's criterion is safer for horizontal flow than Bligh's empirical rule.

2.1.3.3 Sellmeijer

Sellmeijer derived the first analytical model describing the process of piping in 1988. Sellmeijer based his model on the combination of flow through an aquifer, flow in the pipe and the balance of forces on the grains (Förster et al., 2012). The starting point for his model is schematized in Figure 2.10. Sellmeijer assumes the formation of a pipe (length of l) due to a head difference.

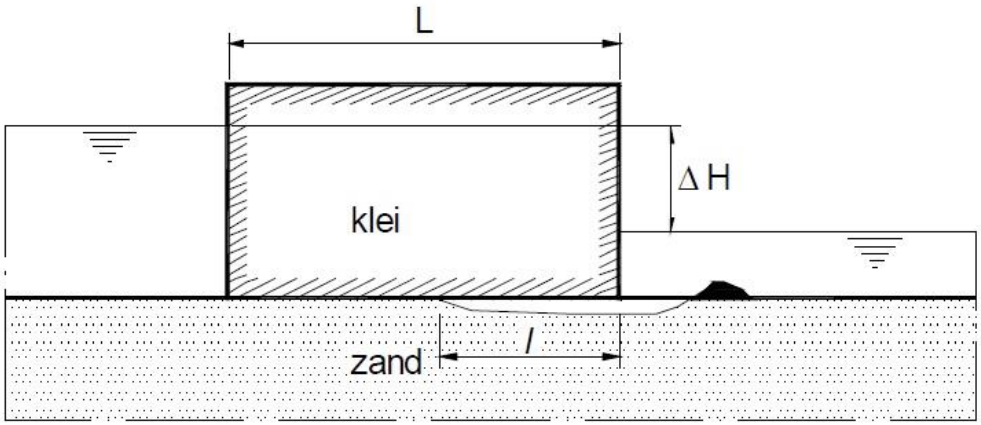

Figure 2.10: Schematization of the model of Sellmeijer (Sellmeijer, 1989).

In the model of Sellmeijer 3 equations are linked together: A equation for the description of groundwater flow, an equation for laminar flow in the pipe and an equilibrium equation on the inflow of particles due to flow and the resistance of the bed (Vandenboer, 2018). With the combination of these equations, the maximum head difference can be calculated. The head difference depends on the ratio of l/L, the permeability, diameter of the grains, and the rolling resistance. This forms the basis of the formula modelled by Sellmeijer (Förster et al., 2012).

In Figure 2.11 a graph is presented combining the head difference with the ratio l/L. Sellmeijer's idea presents that there is an equilibrium in the growth of the pipe depending on the head difference. The pipe will reach an equilibrium situation when the head difference does not exceed the critical head. If the critical head is exceeded the pipe progresses till the failure of the structure. Figure 2.11 shows that the critical head difference is obtained at 50% of the length of the structure (l/L≈0.5).

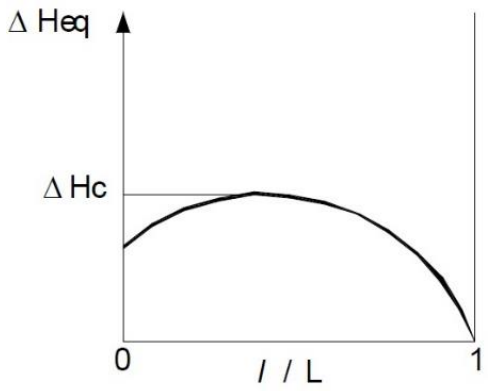

Figure 2.11: Equilibrium head difference as a function of the l/L ratio (Förster et al., 2012).

Sellmeijer combined the different parameters and equations to the following expressions (Förster et al., 2012):

$$\Delta H_c = L\, F_r\, F_s\, F_g \tag{2.4}$$

$$F_{resistance} = \eta \left(\frac{\gamma'_p}{\gamma_w}\right) tan(\theta) \left(\frac{RD}{RD_m}\right)^{0.35} \tag{2.5}$$

$$F_{scale} = \frac{d_{70m}}{\sqrt[3]{kL}} \left(\frac{d_{70}}{d_{70m}}\right)^{0.4} \tag{2.6}$$

$$F_{geometry} = 0.91 * \left(\frac{D}{L}\right)^{\frac{0.28}{\left(\frac{D}{L}\right)^{2.8}-1}+0.04} \tag{2.7}$$

With:

ΔH_c =	Critical head difference (m)
L =	Horizontal seepage length (m)
γ'_p =	Submerged volumetric weight sand (kN/m^3)
γ_w =	Volumetric weight water (kN/m^3)
θ =	Bedding angle (°)
D =	Aquifer thickness (m)
η =	Constant of white (-)
κ =	Intrinsic permeability of the aquifer (m^2)
RD =	Relative density $((e_{max}-e)/(e_{max}-e_{min}))$ (-)
RD_m =	Averaged relative density in small-scale tests (0,725)
$d70$ =	70%-fractile of grain size distribution (m)
$d70_m$ =	Reference value for d_{70} in small-scale tests ($2.08*10^{-4}$ m)

From the expression (4) a factor of safety was formed. The safety factor for the expression of Sellmeijer is defined as:

$$F = \frac{\Delta H_c}{h - h_p - 0.3\, d_1} \tag{2.8}$$

With:

ΔH_c =	Critical head difference (m)
h =	Water level at the entry point (high water side) (m)
h_p =	Water level at exit point (low water side) (m)
d_1 =	Thickness of the hinterland aquitard (m)

The head difference in the factor of safety is reduced by a factor of 0.3d (Equation 2.8) when the sand layer is covered by a clay layer (Förster et al., 2012). This is related to the fluidization of sand particles in the exit channel. When the sand boil is growing an additional resistance for the flow is considered and therefore the actual head difference is reduced.

The expressions (2.4-2.7) represent the current Sellmeijer equations. Later studies show that there are some slight changes to the current expressions including the KAS parameter. The KAS parameter includes the angularity of the grains (Sellmeijer et al., 2011) (Van Beek et al., 2010). However, a theoretical explanation for these adjustments was not given (Vandenboer, 2018).

2.2 Overview of performed experiments

During the last decades, several experiments were performed on backward erosion piping, on small, medium and large-scales. This thesis focusses on small-scale experiments. The table below gives an overview of the different types of performed experiments regarding backward erosion piping and the relation to the progression rate.

In addition to the experiments listed in Table 2.3, are the most recent experiments briefly described in the following sections.

Source	Type of research	Information about the progression rate
Pietrus (1981)	Effect of artificially created pipe length and radius on the critical head.	No
De Wit (1984)	Effect of scale, type of exit point and sand properties on the critical head.	No
Hanses (1985)	Erosion mechanism, pressure development in pipe and effect of scale on the critical head.	Yes, although experiments performed with a different configuration.
Townsend et al. (1988)	Effect of sand characteristics on the critical head.	No
Silvis (1991)	Investigation of scale effects.	No
Yao et al. (2007)	Investigation of effect of configuration on piping process and critical head.	No
Ding et al. (2007)	Investigation of piping in sand samples with multiple layers.	No
Van Beek et al. (2008)	Lateral heterogeneity.	No
Van Beek et al. (2011)	Effects of scale and sand properties on the critical head.	No
Van Beek (2015)	Initiation and progression of backward erosion piping (Doctoral Thesis).	Many tests performed regarding small-scale experiments, but no information about the progression rate.
Robbins (2017)	A new type of laboratory test measuring the local hydraulic conditions required for progression.	Yes, although experiments performed experiments in a cylinder (different set-up).
Allan (2018)	Cycling and overloading tests in a medium-scale flume (Doctoral Thesis).	Yes, although experiments were performed in a medium-scale set-up with a strong focus on the exit geometry and gradients.
Vandenboer (2018)	A study on the mechanism of backward erosion piping (Doctoral Thesis).	Yes, small-scale experiments although with supercritical loading on the sandy aquifer.

Table 2.3: Overview of performed experiments related to the progression rate (Van Beek, 2015).

2.2.1 Experiments performed by Robbins (2017)

In 2017 Bryant Robbins developed a new type of test for measuring local hydraulic conditions in backward erosion piping (Robbins et al., 2017). The testing equipment consisted of three 1.53 m long acrylic cylinders with internal diameters of 25.4 (tube A), 76.2 (tube B) and 152.4 mm (tube C). During the tests, it was concluded that the small tube may have been too small for the analysis of backward erosion piping (Robbins et al., 2017). Robbins measured with his experiment the local gradient for two types of sand. In the figures below the cross-section and a photograph of the experimental set-up is presented.

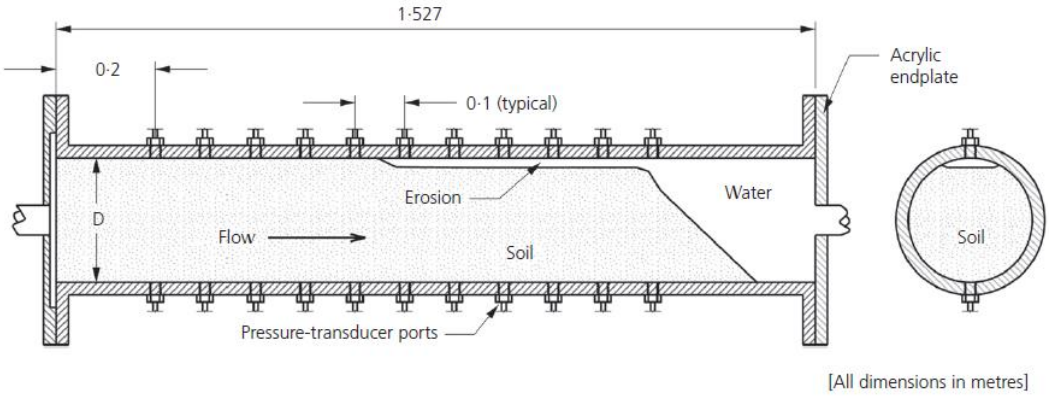

Figure 2.12: Dimensions of experimental tubes and locations of pressure transducers (Robbins et al., 2017).

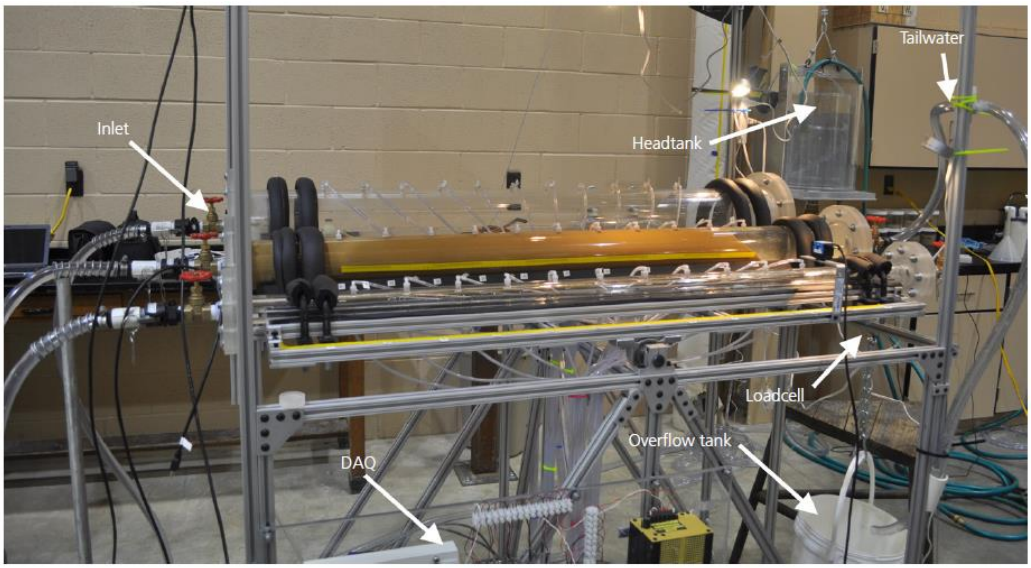

Figure 2.13: Photograph of experimental set-up (Robbins et al., 2017).

Robbins also studied the progression rate of the pipe. In a flood situation, this could be very interesting for engineers, to be able to assess the rate of the development of the pipes during a short flood (Robbins et al., 2017). In Figure 2.14 a relationship is found for the erosion rate and the maximum Darcy velocity (Robbins et al., 2017). It shows that an increase in erosion rate was found for an increase in the Darcy velocity. It should also be mentioned that the Darcy velocity is an averaged value over a distance of 10 cm (distance between two transducers) and

this was smaller than the local velocity at the tip of the pipe. The pipe development is approximately 4-5 times faster than the estimated Darcy velocity.

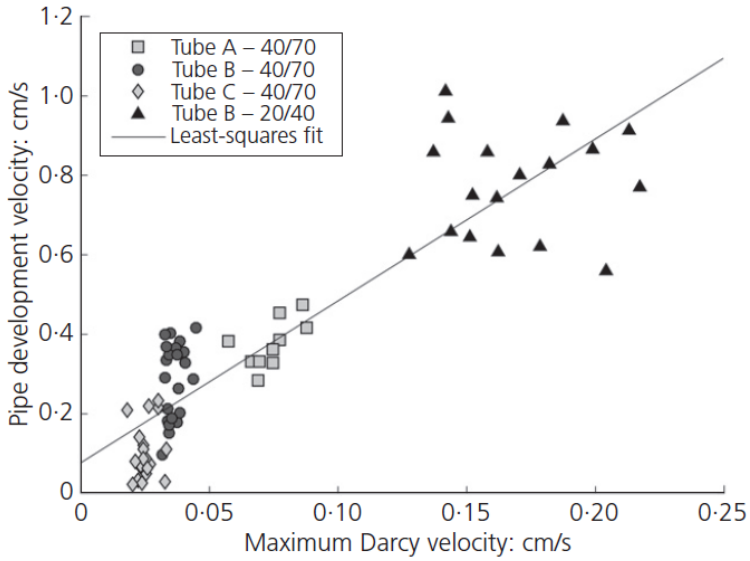

Figure 2.14: Relation between maximum Darcy velocity and progression rate (Robbins et al., 2017).

Figure 2.15 shows the progression rate as a function of the void ratio. It can be observed that the pipe development velocity is not only a function of the gradient but also of the void ratio. The increase of the progression rate with the gradient was much more significant for experiments conducted with a high void ratio (Robbins et al., 2017).

At the lower void ratio's (denser sand) the variation of the data points is smaller than for the higher void ratio's (loose sand). For example, the green data points (e=0.61) show a large variation. In this case, the relation between the different points is rather small, to immediately draw a line and link it to a certain gradient. Perhaps is the large variation of datapoints the cause of measurement uncertainties.

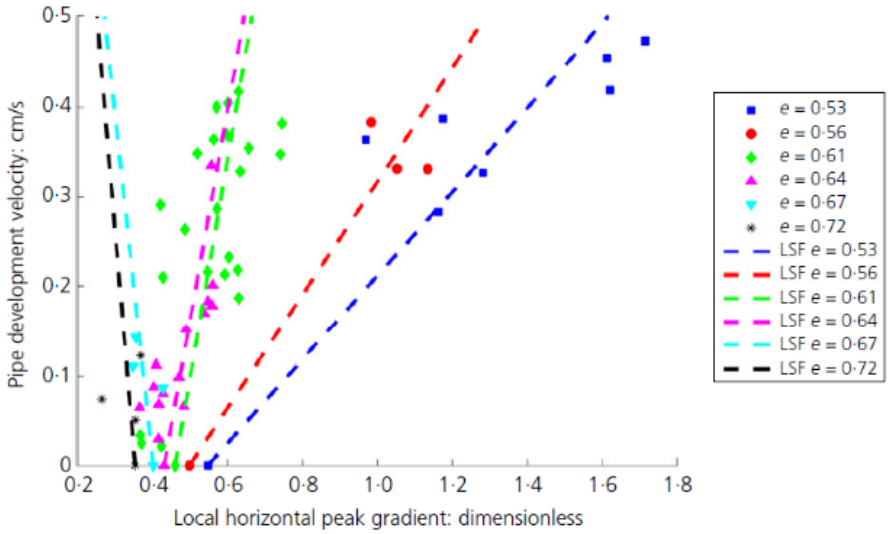

Figure 2.15: Pipe development velocity as a function of different void ratio's (Robbins et al., 2017).

What could be improved in further tests are the influences of different soil types and the configuration of the tests on the measurements of the local critical gradient (Robbins et al., 2017). As an addition to the experimental work of Robbins, more research could be performed on the progression rate itself. The experiments of Robbins focus mainly on the local gradients and the development of the pipe depth. In the paper of Robbins (Robbins et al., 2017) only one graph is presented of the pipe development velocity related to the void ratio. The progression rate related to the head difference and the sediment transport rate over time is not studied by his cylindric setup.

2.2.2 Experiments performed by Allan (2018)

Rebecca Allan performed for her Doctoral thesis at The University of New South Wales (Australia) five groups of tests (92 tests total) using a medium-scale flume. In these tests' different aspects of experimental research for backward erosion piping were studied. The experimental set-up variables included exit geometry, soil density, seepage length, soil grading and hydraulic loading sequence (Allan, 2018).

For the laboratory tests, a medium-scale flume was used as shown in Figure 2.16. The flume consists of a rectangular aluminium box with a Perspex cover on top. By placing a hydraulic head difference across the flume, seepage would occur as a first stage which in the end will result in backward erosion piping (Allan, 2018).

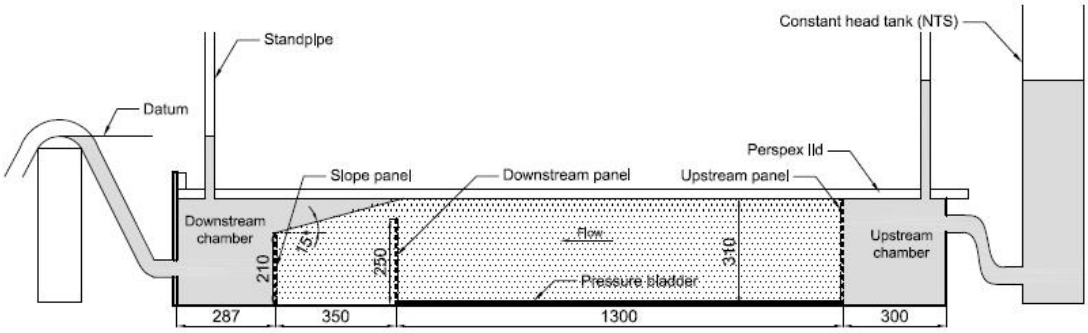

(a) Longitudinal section through centreline

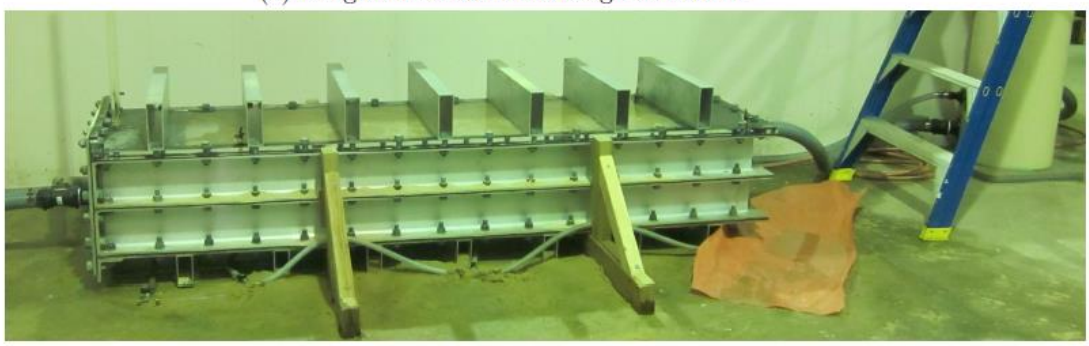

(b) Photo

Figure 2.16: Medium-scale flume set-up (Allan, 2018).

Allan studied as a part of her experiments also the progression gradient due to loading. In this last group of experiments (group five), Allan applied a head difference to the flume which was raised and dropped in a series of cycles to model successive flood events (Allan, 2018). To

determine if the tip progression speed increases with a head difference above the critical head difference, the hydraulic load had to be raised beyond the critical head level (tests 83-92) (Allan, 2018). The results of these experiments are plotted in Figure 2.17. The input for Figure 2.17 is shown in Table 2.4.

Test	Head difference		End channel length (mm)	Duration of active tip progression (hrs)	Avg. progression speed (mm/minute)	Duration of forward deepening (hrs)
	(mm)	% of avg. crit. head of 206mm				
83	347	168	1300	0.35	62	3.60
84	367	178	1300	0.42	51	1.10
85	330	160	1300	0.35	62	1.08
86	305	148	1146	0.57	34	1.27
87	309	150	1300	0.47	46	1.22
88	271	132	1276	1.03	21	2.40
89	259	126	1300	0.75	29	1.42
90	230	112	1112	0.48	39	0.75
91	216	105	1300	4.83	4	-
92	225	109	1300	2.15	10	5.63

Table 2.4: Results of the experiments above critical loading (Allan, 2018).

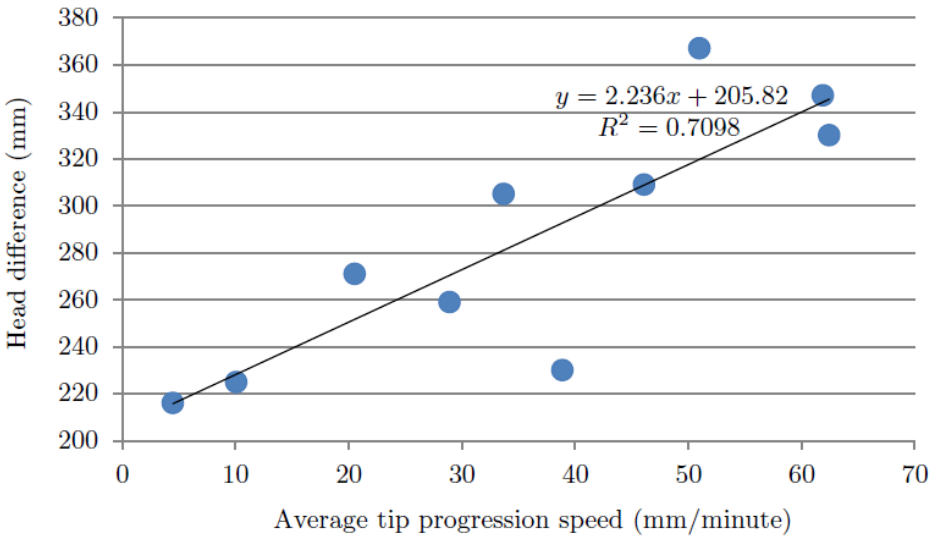

Figure 2.17: Tip progression speed with applied head difference above critical loading (Allan, 2018).

Figure 2.17 presents a linear relationship for the progression speed against the head difference, with 2 outliers. The experimental results show that an increase of 10% in head difference, increases the progression speed approximately three times (Allan, 2018).

As a recommendation, Allan would perform additional experiments to obtain more knowledge about the increase of the progression speed. For this reason, testing with other scales could be very useful, to determine whether such large increases in the progression speed would occur in the field as well. (Allan, 2018).

2.2.3 Experiments performed by Vandenboer (2018)

Backward erosion piping is an important failure mechanism for cohesive water-retaining structures founded on a sandy aquifer (Vandenboer, 2018). Kristine Vandenboer studied for her Doctoral thesis the effects of hydraulic overloading including sudden critical and supercritical hydraulic loading. For a better understanding of the behaviour of backward erosion piping Vandenboer performed different small-scale experiments. A cross-section of the experimental set-up is presented in Figure 2.18.

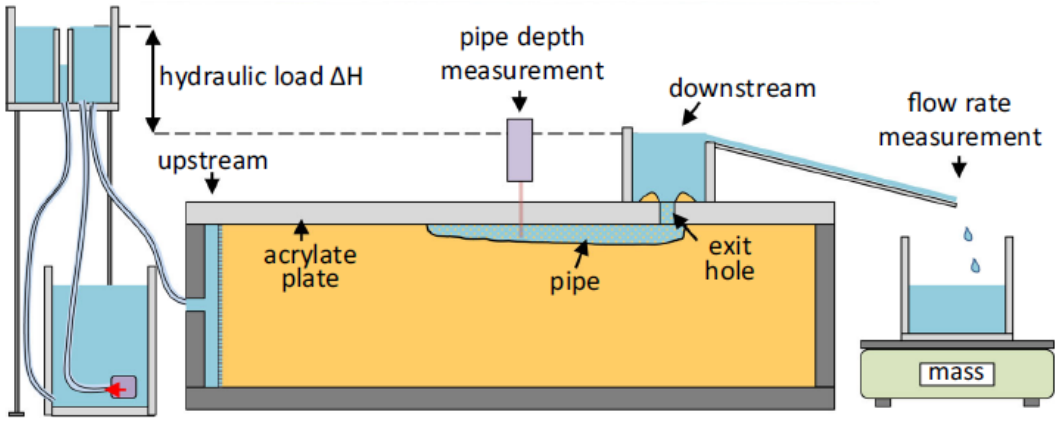

Figure 2.18: Set-up for small-scale experiments (Vandenboer, 2018).

The small-scale box is made of PVC material and filled with sandy material. On top of the box an acrylate plate is placed with a circular opening, this is called the exit hole. When a hydraulic load is applied (the difference between upstream and downstream reservoir) there is a flow of water and sediment. This results in a crater of sand around the circular exit point. On top of the exit point, an acrylate cylinder was placed to collect the eroded sand (Vandenboer, 2018). In Figure 2.19 two photographs are shown of the experimental set-up.

Figure 2.19: Top view of the small-scale box filled with sand (l), Overview of the full experimental set-up (r) (Vandenboer, 2018).

In the research of Vandenboer (Vandenboer, 2018) the erosion rate of the pipe was studied concerning different supercritical loads. In these experiments, a constant head ($\Delta H > \Delta H_c$) was suddenly applied at the start. This resulted in backward erosion piping without any indication of equilibrium (Vandenboer, 2018).

The experiments were performed with different $\Delta H/\Delta H_c$ ratio's (from 1 till 5). Vandenboer found a critical head of 60 mm. With a ratio of 5, the maximum applied head difference was 300 mm.

The table below gives an overview of the applied hydraulic loads. It can be observed that a higher ratio of applied head to critical head, reduces the time duration of the test significantly.

Applied sudden hydraulic head	ΔH [mm]	60	80	100	120	180	240	300
Ratio applied head to critical head	$\Delta H/\Delta H_{crit}$ [-]	1	1.4	1.7	2	3	4	5
Number of tests	# [-]	2	1	2	2	2	1	1
Time duration of test	T_{max} [min]	68.8	12.5	6.8	3.8	1.6	1.1	0.8

Table 2.5: Overview experiments with supercritical hydraulic loads (Vandenboer, 2018).

Vandenboer plotted the results of Table 2.5 into Figure 2.20. Figure 2.20 shows the erosion velocity of the pipe tip (downstream to upstream) over the ratio of hydraulic loading.

In the left figure (a) it can be observed that the velocity increases linearly with the ratio of the applied load.

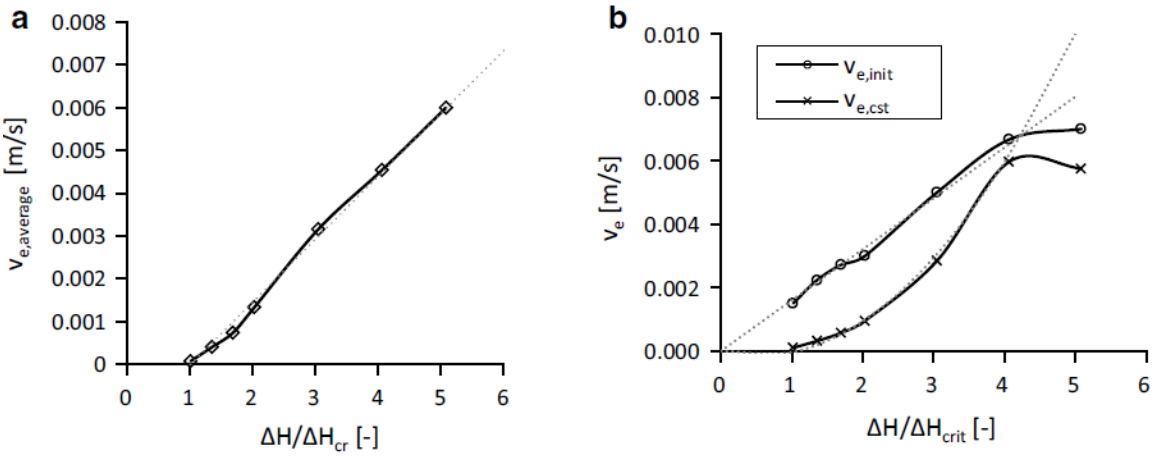

Figure 2.20: Progression rate of the pipe related to the applied ratio (Vandenboer, 2018).

In the right figure (b) the initial erosion velocity and the final erosion velocity are plotted. The initial erosion velocity is the velocity measured from T=0 until the first measurement, the final erosion velocity is defined as the erosion velocity measured from T=0.1 till T= 1 ($v_{e,cst}$ more or

less constant) (Vandenboer, 2018). At the ratio of $\Delta H/\Delta H_c$= 4, an intersection point is found with $v_e \approx 0.006$ m/s. Beyond this point, erosion velocities become relatively constant. The erosion velocity may be limited due to the width of the box (Vandenboer, 2018).

In reality, the time required for the development of the pipe decreases with the intensity of the flood. Which results in less time available to perform preventive measures (Vandenboer, 2018).

2.2.4 Summary of available experiments

In the last sections (2.2.1-2.2.3) the most recent experiments of backward erosion piping were reviewed. The experiments from Robbins (Robbins et al., 2017), Allan (Allan, 2018) and Vandenboer (Vandenboer, 2018) form a good base for the overview of the different types of performed experiments regarding backward erosion piping. The differences between the experiments can be found in the type of set-up. For example, Robbins used a cylindrical set-up and Allan used a medium-scale box with the focus on overloading. With these differences in shape, but also in size it is difficult to compare all the experimental results. On the other hand, the results of the recently performed experiments are available and can be used as a start for a better understanding.

The recent experiments consider the hydraulic load, although the experiments were never stopped at the moment of equilibrium to study the erosion processes. The past three experiments focussed more on the different hydraulic gradients than on the sediment transport from the pipe. Information on sediment transport regarding piping is very limited, and it was never studied using piping experiments.

The objective of this thesis is to research which parameters and processes influence the progression and sediment transport rate in laboratory experiments of backward erosion piping. To discover more relations the tests are stopped at the moment of equilibrium ($\Delta H=\Delta H_c$). For example, when the equilibrium situation is found, observations can be made regarding the transport of sediment.

This research could, therefore, make a valuable contribution to the experiments performed in the past.

2.3 Sediment transport in piping

In the second phase of the different piping phases (Figure 2.3) the first movement of particles can be observed. In this phase, the first grains/particles are being transported through the exit point at the toe of the dike. The figure below illustrates the first developments in backward erosion piping regarding the transport of particles.

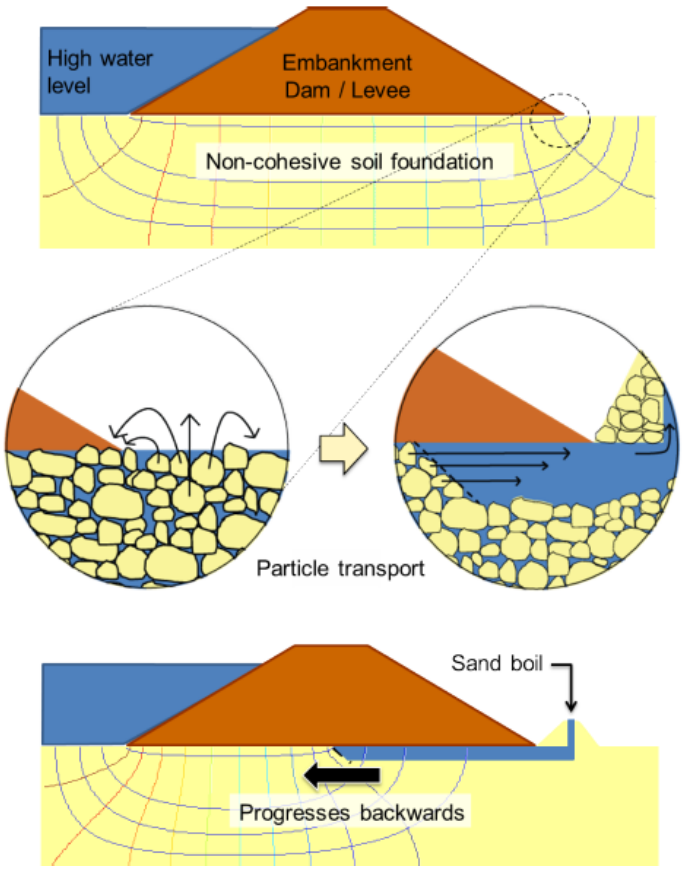

Figure 2.21: Process of particle transport for backward erosion piping (Vandenboer, 2018).

2.3.1 Equilibrium of forces

Sediment transport can be defined as the movement of solid grains or particles. Usually, the movement of particles is caused by the flow of water. When a particle is subjected to flow different forces are acting on the particle itself. Whether particles are eroded depends on the critical shear stress and the forces acting on the grain (Van Beek, 2015). The different forces acting on a particle are schematized (Jansen, 1979) in Figure 2.22.

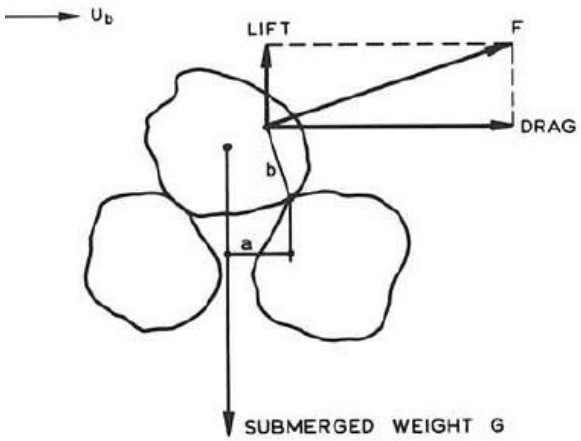

Figure 2.22: Forces acting on a particle on the bed (Jansen, 1979).

The acting forces on the grain are the submerged weight (G), the drag and lift forces (Jansen, 1979). In the equilibrium situation (ΣM = 0) the moment of forces (2.9, 2.10) around the point of rotation must be zero (Jansen, 1979).

$$\Sigma M = 0 = Fb - Ga \tag{2.9}$$

or

$$C_F \; 1/2 \; \rho_w \; U_b^2 \; \frac{\pi}{4} d^2 \; b = \frac{\pi}{6} d^3 (\rho_s - \rho_w) \; g \; a \tag{2.10}$$

With:

F =	Resultant force (N)
C_F =	Drag coefficient of force F (-)
ρ_w =	Density of water (kg/m^3)
U_b =	Flow velocity (m/s)
d =	Particle diameter (m)
b =	Distance from force till point of rotation (m)
ρ_s =	Particle density (kg/m^3)
g =	Acceleration of gravity (m/s^2)
a =	Horizontal distance from force till point of rotation (m)

The flow velocity is proportional to the shear velocity ($u_* = (\tau_b/\rho_w)^{1/2}$). The shear velocity is a parameter with the dimension of the velocity, but it expresses the shear stress. Therefore it is not a velocity which can be measured (Schiereck, 2012).

The equation of the acting forces (2.10) can be reduced to the ratio of the flow force to the gravity force (G). This gives the following ratio:

$$\Psi = \frac{u_*^2}{\Delta \; g \; d} \tag{2.11}$$

With:

u_* =	Shear velocity (m/s)
Δ =	Relative density $(=(\rho_s - \rho_w)/\rho_w)$ (-)
g =	Acceleration of gravity (m/s^2)
d =	Particle diameter (m)

The parameter (Ψ) from expression 2.11 is also known as the Shields parameter.

2.3.1.1 Shields parameter (1936)

Shields (Shields, 1936) performed experiments in rectangular flumes filled with sediment to research the influence of the weight and shape of the grains on the movement of river beds (Allan, 2018). Shields created a relation between the dimensionless shear stress and the particle Reynolds number considering the friction force caused by the water on the bed (Schiereck, 2012). This is also called the shear stress approach.

In Figure 2.23 are the results plotted of the dimensionless shear stress and the particle Reynolds number. For the points above the curve, particles will move and for points below the curve, the particles will be stable.

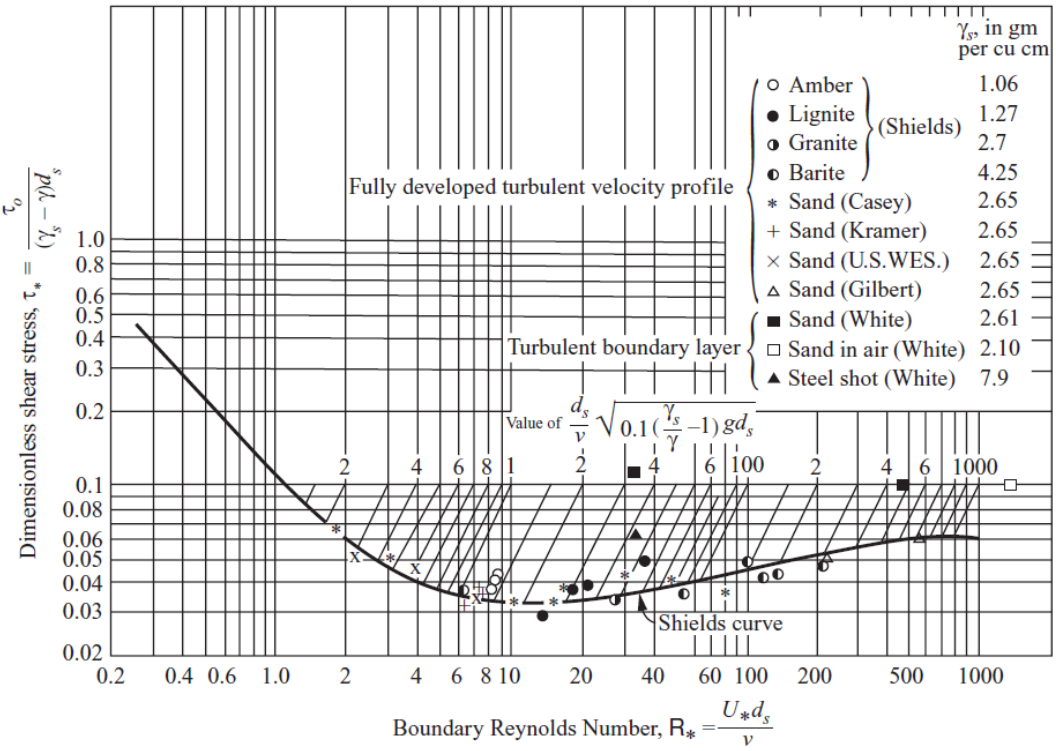

Figure 2.23: Shields curve (Vanoni et al., 2006).

Shields created the critical Shields parameter (Schiereck, 2012). This parameter (2.12) is used for the assessment of the incipient motion.

$$\Psi c = \frac{\tau_c}{(\rho_s - \rho_w)\, g\, d} = \frac{u{*}_c^2}{\Delta\, g\, d} = f\left(\frac{u{*}_c\, d}{\upsilon}\right) \qquad (2.12)$$

With:

Ψ_c =	Critical Shields parameter (-)
τ_c =	Critical shear stress (N/m^2)
ρ_s =	Particle density (kg/m^3)
ρ_w =	Density of water (kg/m^3)
g =	Acceleration of gravity (m/s^2)
d =	Particle diameter (m)
$u{*}_c$ =	Critical shear velocity (m/s)
Δ =	Relative density $(=(\rho_s - \rho_w)/\rho_w)$ (-)
ν =	Kinematic viscosity $(=\mu/\rho)$ (m^2/s)

The critical Shields parameter is a stability parameter which is defined using a critical value of the shear velocity. The particle Reynolds parameter indicates if the particle extends to the turbulent boundary layer or stays in the viscous sublayer (Schiereck, 2012). The combination of these two parameters determines if a particle is transported or not.

The transport of particles can also be classified with different transport stages. From the point when particles show the first signs of movement (incipient motion) till general transport of the grains. The incipient motion (start of movement) is researched during experiments in a flume (Delft Hydraulics, 1969). As a result, the different stages of transport were categorized (Schiereck, 2012):

0. No movement at all.
1. Occasional movement at some location.
2. Frequent movement at some location.
3. Frequent movement at several locations.
4. Frequent movement at many locations.
5. Frequent movement at all location.
6. Continuous movement at all locations.
7. General transport of the grains.

Shields researched the threshold of motion in 1936 (Shields, 1936) and found experimentally that there is a minimum Shields stress required to move a particle. The Shields curve and the different transport stages were plotted in the same graph and are shown in Figure 2.24.

The black line represents the Shields curve and shows that the Shields criterion has a very good fit with stage 6 (continuous movement at all locations) (Schiereck, 2012).

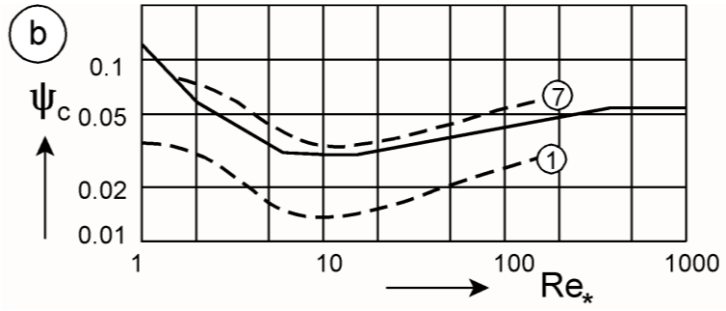

Figure 2.24: The 7 stages of motion presented in the Shields diagram (Schiereck, 2012).

2.3.1.2 White (1940)

White performed different experiments to determine when particles were eroded and transported from the bed. For his experiments, White used three types of flow: viscous steady, steady inviscid and turbulent flow (Van der Zee, 2011).

For the viscous steady flow White illustrates the equilibrium of forces for an individual grain. Sellmeijer assumes viscous steady flow in his work of backward erosion piping and uses the model of White. From former experiments (Nikuradse, 1933) it is clear that viscous or tangential stress predominate when the particle Reynolds number ≤ 3.5 (White, 1940). The equilibrium of an individual grain including the tangential stresses is schematized in Figure 2.25.

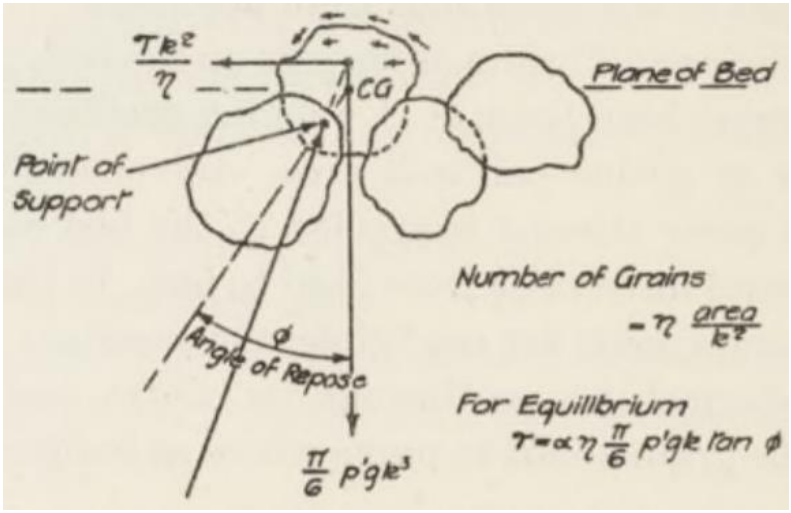

Figure 2.25: Equilibrium of forces on a soil particle (White, 1940).

Based on the equilibrium of forces the critical shear stress is defined as:

$$\tau_c = \alpha\,\eta\frac{\pi}{6}\gamma_p' d\ tan\ (\theta_1) \tag{2.13}$$

With:

τ_c =	Critical shear stress (N/m^2)
α =	Particle/eccentricity coefficient (-)
η =	Constant of white (-)
γ'_p =	Submerged volumetric weight sand (kN/m^3)
d =	Particle diameter (m)
θ_1 =	Angle of repose (°)

White used different coefficients to include effects of the drag force regarding the eccentricity of the grains and the packing coefficient. The fact that the drag force is not equally applied to all grains is included with the packing coefficient (Allan, 2018). White suggests a combination of both coefficients (αη) of 0.31 (Allan, 2018). Sellmeijer (section 2.1.3.3) did not use the parameter α for his model due to its uncertainty (Allan, 2018). Therefore Sellmeijer used a conservative value of η=0.25 based on two experiments for laminar flow (Van Beek, Bezuijen, & Sellmeijer, 2013; Van der Zee, 2011).

The relation (2.13) of White (White, 1940) displays that the critical shear stress is proportional to the sediment diameter. White conducted two experiments in 1940 with a different sand diameter, sand with a mean grain size of 0.21 mm and 0.9 mm in the fully laminar flow regime (Reynolds number < 1000) (Hoffmans & Van Rijn, 2018). The value of the laminar Shields parameter ($\Psi_{lam,c}$) ranged from 0.15-0.3. The results of White are presented in the Shields diagram (Figure 2.26) combined with other experimental results.

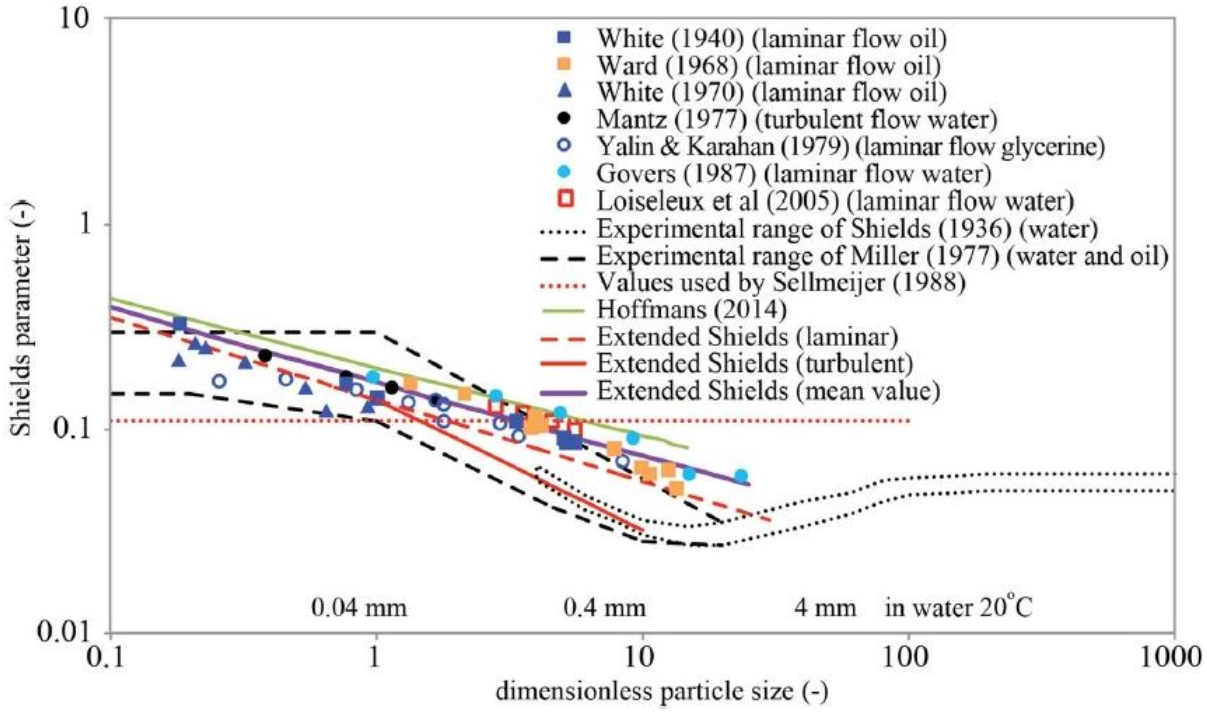

Figure 2.26: Shields diagram for laminar and turbulent flows (Hoffmans et al., 2018).

In Table 2.6 an overview is given of the incipient motion for particles in laminar flow of the added experiments from Figure 2.26 (Van Beek et al., 2019).

Source	Material	Mean grain size [mm]	Fluid
White (1940)	Sand	0.21 / 0.90	Oil
Ward (1968)	Sands / glass beads / taconite / plastics	0.240–2.29	Oil
White (1970)	Natural sands and silts / plastics / lead glass / crushed silica	0.016–2.2	Water / oil
Mantz (1977)	Natural grains / crushed silica	0.015–0.066	Water
Yalin and Karahan (1979)	Sieved river sands	0.56–2.85	Glycerine / water mixture
Govers (1987)	Silt and quartz sands	0.045–1.098	Water
Loiseleux et al. (2005)	Glass beads	0.110–0.220	Water
Ouriemi et al. (2007)	Polystyrene / PMMA / glass spheres	0.132–0.538	Oil / water mixture

Table 2.6: Overview of different types of particles in laminar flow (Van Beek et al., 2019).

2.3.2 Incipient motion in laminar flows

Most studies about the transport of sediment in rivers and coastal waters are related to turbulent conditions. The uncommon element of sediment transport in pipes are the laminar flow conditions. The pipes in backward erosion are relatively small (depth in the order of millimetres), so it is usually assumed that the flow is laminar (Van Beek et al., 2019). The laminar flow in the pipe was confirmed by the calculated Reynolds numbers, which did not exceed the critical Reynolds number of 2800 for parallel plates (Fox et al., 2009).

Due to the relatively low flow velocities and pipe depth laminar flow conditions are applicable. For this reason, different transport formulas are more suitable than the traditional transport formulas for rivers (Engelund-Hansen & Meyer-Peter-Müller).

Figure 2.27 presents the different experiments plotted in the Shields diagram. Most experiments are plotted on the left side of the graph.

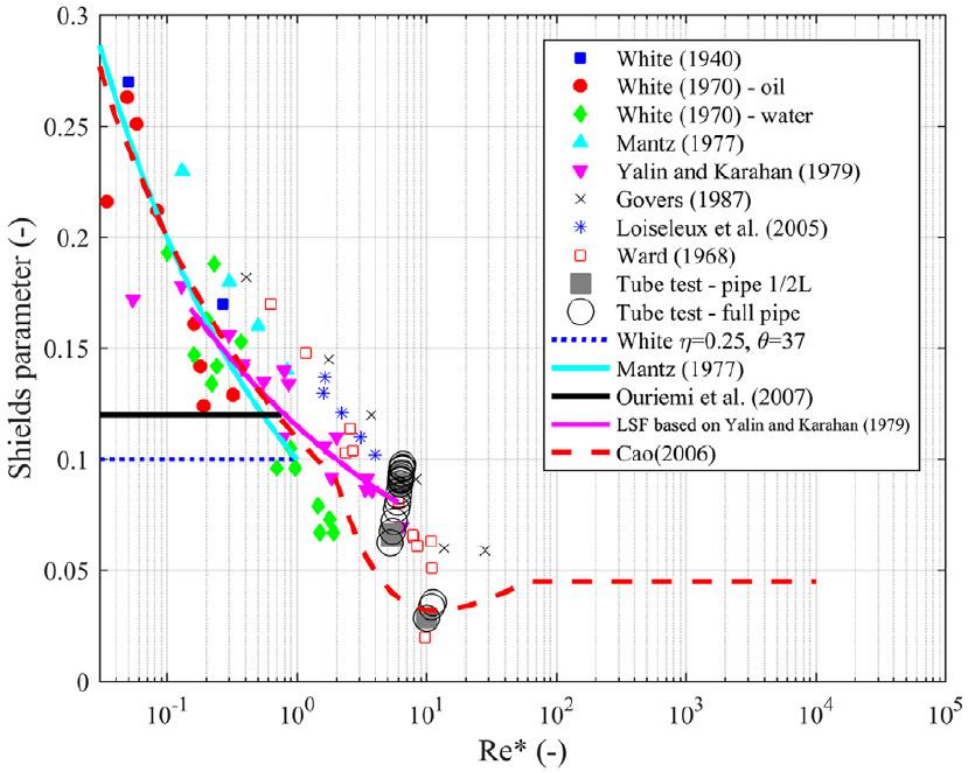

Figure 2.27: Shields parameter related to the particle Reynolds number for laminar flow (Van Beek et al., 2019).

2.3.3 Transport mechanisms

Before the particles are transported there is fluidization required at the tip of the pipe. When the voids are filled the particles can be transported. As a result of the transport of particles, small pipes are formed including a slope. Schmertmann (Schmertmann, 2000) suggests that the detachment of particles occurs due to the combination of horizontal and vertical seepage gradients (Allan, 2018). The horizontal gradients lead to regressive slope failure and the vertical gradients to fluidization of the sand particles. Figure 2.28 presents a schematisation of regressive slope failure due to horizontal gradients.

The mechanism of the horizontal gradient is supported by observations from Hanses (Hanses, 1985), Townsend (Townsend et al., 1988) and Van der Zee (Van der Zee, 2011) where cycles of grains slide into the channel. When the cycle of slope failure continues the erosion continues into the propagation of the pipe channel (Allan, 2018).

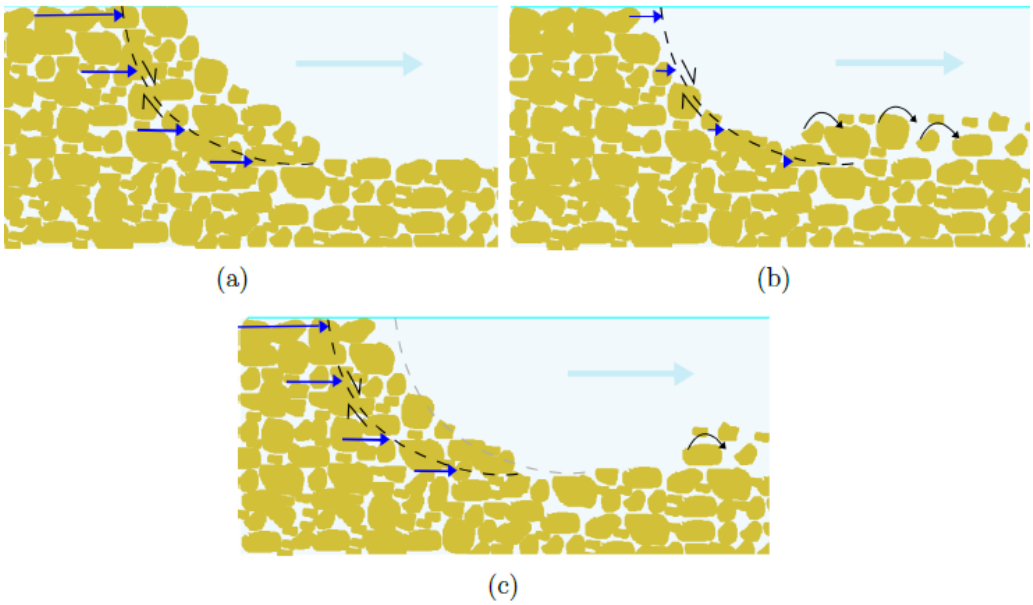

Figure 2.28: Slope failure due to horizontal gradient (Allan, 2018).

The schematization of the vertical gradient is presented in Figure 2.29. Schmertmann (Schmertmann, 2000) describes the vertical gradient as the mechanisms which lead to fluidisation of the sand grains at the tip of the pipe. In this mechanism, there are four different stages to be distinguished according to Schmertmann. In the left figure (a) the gradient is large enough to suspend the particles, but when the particles are lifted (b) the gradient reduces (smaller arrows).

When the particles are in suspension (c), the particles roll along the bed with the direction of the flow. In this stage, the particles are removed from the toe of the slope, which accommodates space for particles to slide down and replace the transported particles. In the bottom right figure (d) a new slope and bed are formed. The dotted grey-line presents the former slope, the new slope shifted to the left in the direction of the progression of the pipe (Allan, 2018).

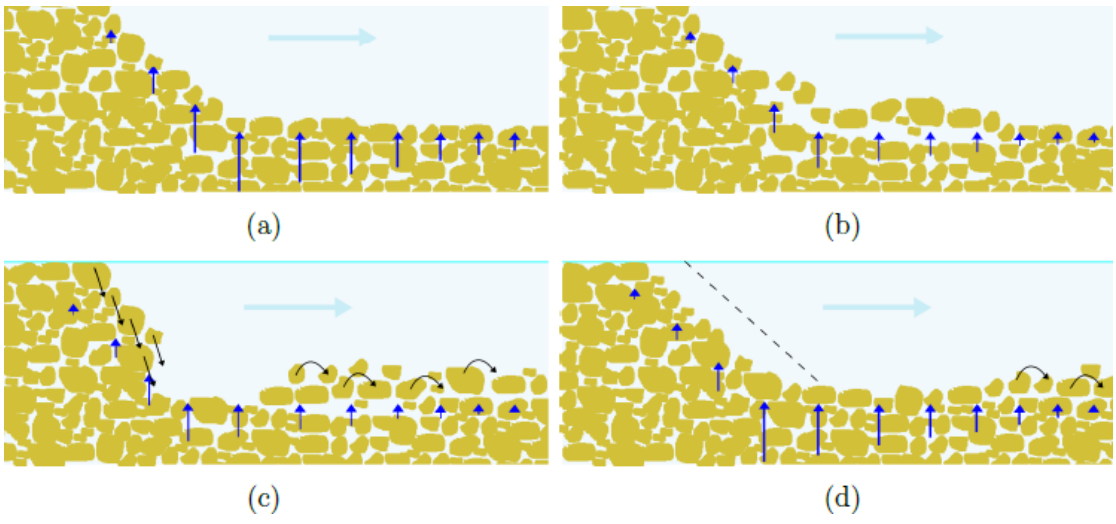

Figure 2.29: Mechanism of the vertical gradient (Allan, 2018).

2.3.4 Dilatancy

Sand consists of grains and voids. When a shear stress is applied, the volume changes from a compact sample to a more open sample. This increases the porosity and enhances the flow through the soil. Figure 2.30 presents the dilatancy principle.

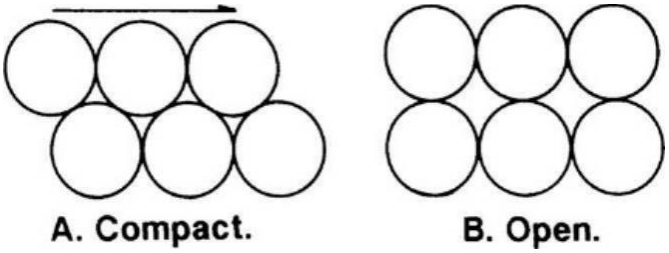

Figure 2.30: Dilatancy principle change in volume (Acsess library: Soil survey horizons, 2015).

Before all voids can be filled with water, the porosity needs to increase to a critical value (De Groot et al., 2009). When this value is reached the particles can be transported. Equation 2.14 presents the wall velocity as a function of the hydraulic conductivity, the gradient and the porosity (De Groot et al., 2009). The dilatancy of the sand influences the progression rate. A soil sample with a higher relative density (RD), has a lower void ratio and gives a lower progression rate.

$$v_{wal} = k \cdot i_{loc} \cdot \frac{1-n_{max}}{n_{max}-n_0} \approx 10 \cdot k \cdot i \tag{2.14}$$

With:

v_{wal}	Wall velocity (m/s)
k =	Hydraulic conductivity (m/s)
i_{loc} =	Local peak gradient (dh/dx) (-)
n_0 =	Initial Porosity (-)
n_{max} =	Maximum porosity (-)

2.3.5 Sediment transport model

2.3.5.1 Cheng (2004)

The available formulas for bedload transport often relate the dimensionless bedload transport rate (Φ) to the dimensionless shear stress or the Shields parameter (Ψ) (Cheng, 2004). In equation 2.15 the sediment transport rate is given based on Einstein's bedload definition (Einstein, 1950). Knowledge about sediment transport in laminar flows is still very limited (Cheng, 2004).

$$\Phi = \frac{q_v}{d\sqrt{\Delta g d}} \tag{2.15}$$

With:

Φ =	Bedload transport rate (-)
q_v =	Volumetric sediment transport rate per unit width (m^2/s)

d = Particle diameter (m)
Δ = Relative density $(=(\rho_s - \rho_w)/\rho_w)$ (-)
g = Acceleration of gravity (m/s^2)

Due to the limited knowledge, Nian-Sheng Cheng studied bedload transport under laminar flow conditions. The objective of his studies was to find an expression for the dimensionless transport rate in combination with exploring the viscous effects on sediment transport (Cheng, 2004). Cheng used a stochastic approach in combination with the characteristic time, t which is the time of exchange between the particles and the bed (Cheng, 2004).

The stochastic approach originated from Einstein (Einstein, 1950) relates the sediment transport rate to the probability of erosion in combination with the diameter of the grains and the characteristic time. Combined with the expression for time, which is proportional to the particle diameter divided by the settling velocity (d/w) a new equation (2.16) was found for the bedload transport rate. The stochastic approach (Einstein, 1950) is based on the saltating of grains. In piping processes, the grains are more rolling and sliding. Equation 2.16 could be applicable but is it possible that the coefficients are not suitable for piping processes. τ

$$\Phi = 0.773\, D_*^{2.66}\ \tau_*^{4} \tag{2.16}$$

$$D_* = \left(\frac{\Delta g}{v^2}\right)^{1/3} d \tag{2.17}$$

$$\Psi = \frac{u_*^{\,2}}{\Delta g d} \tag{2.18}$$

With:

Φ = Bedload transport rate (-)
d = Particle diameter (m)
Δ = Relative density $(=(\rho_s - \rho_w)/\rho_w)$ (-)
g = Acceleration of gravity (m/s^2)
D_* = Dimensionless particle diameter (-)
Δ = Relative density $(=(\rho_s - \rho_w)/\rho_w)$ (-)
g = Acceleration of gravity (m/s^2)
v = Kinematic viscosity $(=\mu/\rho)$ (m^2/s)
Ψ = Shields parameter (-)
u_* = Shear velocity (m/s)

Cheng used the dimensionless particle diameter (D_*) to account for the viscosity and the density of the particle. D_* is a parameter which is often used in the Shields diagram (Figure 2.26). Because the Shields parameter and the particle Reynolds number are a function of the particle diameter and the shear stress, the Shields parameter is often displayed as a function of the dimensionless particle diameter (D_*) (Van Beek, 2015).

Cheng compared his equation with the empirical results from researcher A. Girgis. Girgis researched the transport of fine bed sand by laminar and turbulent flows (Girgis, 1977). The results are presented in Figure 2.31. It shows that the equation is generally supported by the

measurements but deviates for very low values. Cheng did not include the critical shear stress in equation 2.16, therefore is the transport rate always larger than zero.

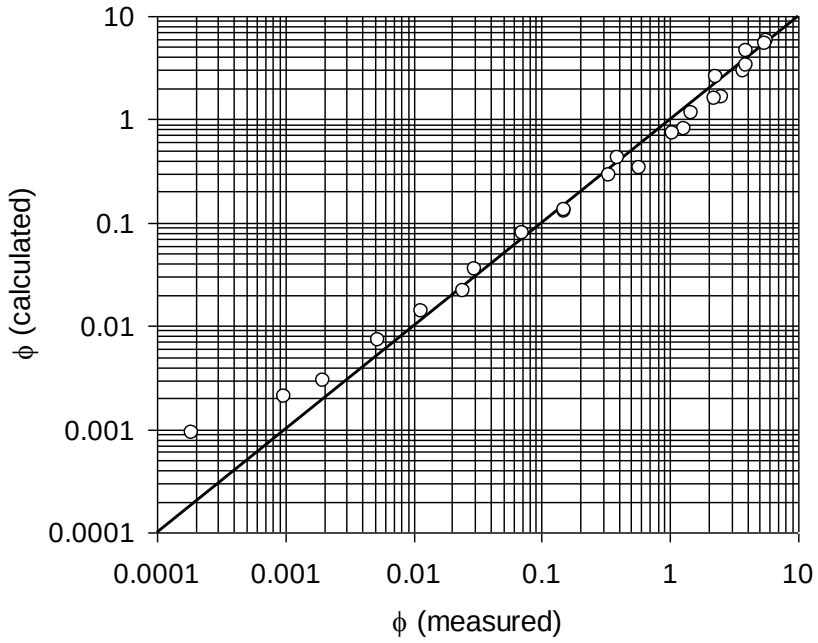

Figure 2.31: Comparison of predicted and measured dimensionless transport rate (Cheng, 2004).

2.4 Hypothesis

A hypothesis is used for experiments to construct an idea or explanation for a phenomenon. In this research, the main target is to determine which processes and parameters influence the progression and sediment transport rate in laboratory experiments of backward erosion piping. This includes a prediction & quantification of the progression and sediment transport rate however, to forecast were the progression and sediment transport rate depends on it is essential to focus first on the development of flow.

For the progression rate of the pipe, sand particles have to be transported. For the transportation of sand, there are two processes which are important to consider: primary and secondary erosion (Van Beek, 2015). Figure 2.32 gives an idea of the two different processes, primary erosion at the tip of the pipe (3) and secondary erosion at the bottom of the pipe (4).

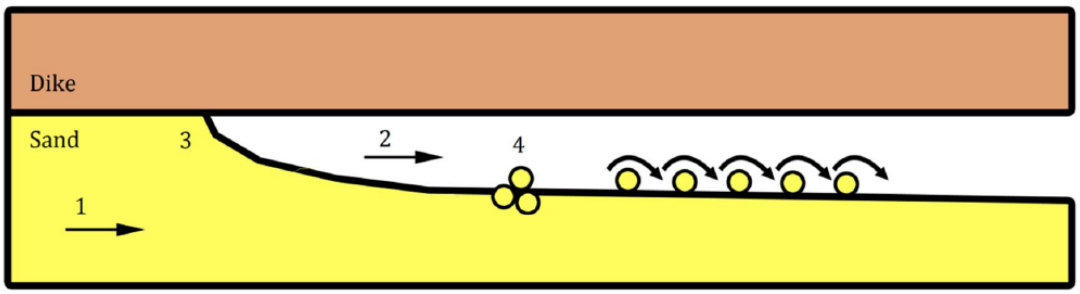

Figure 2.32: Schematization of the processes governing the progression of the pipe (Van Beek, 2015).

Primary erosion describes the process at the tip of the pipe. After the voids are filled with water the particles can be separated and transported. During this stage a slope is formed and before the tip gradient can recover a new slope failure occurs. At that moment the second mechanism is introduced: secondary erosion. Before the pipe can increase in the length the pipe needs to be widened/deepened otherwise the pipe won't be able to transport more sediment. For this reason, more sand is eroded from the bottom of the slope which has formed. Because the flow of water has a smaller depth due to the slope formed by the primary erosion, the bed shear stresses increases (depth <<, bed shear stress >>) to overcome the resistance. For this reason, the depth of the pipe increases, and sand erodes in the vertical direction (secondary erosion).

2.4.1 Parameters of influence

For the erosion of sediment, a certain flow and transport capacity is required. But even if these two requirements are met, the progression rate of the pipe can be limited for example by the pressure dissipation of the tip of the pipe.

Therefore, it is key to find the relative importance of the following parameters to determine which processes and parameters influence the progression/sediment transport rate in laboratory experiments. The parameters of influence are listed below.

Parameters:

- Particle diameter *(d)*
- Gradient *(ΔH/L)*
- Relative density *($RD=(e_{max}-e)/(e_{max}-e_{min})$)*
- Bed shear stress *(τ)*
- Hydraulic conductivity *(k)*
- Head difference *(ΔH)*
- Hydraulic loading (gradually or instant)
- Porosity/void ratio *(e)* (Robbins et al., 2017)

These parameters can be divided into two categories: soil properties and loading or flow. Table 2.7 presents the different parameters categorized by group.

Soil properties	**Loading/flow**
Particle diameter *(d)*	Head difference *(ΔH)*
Porosity/void ratio *(e)* (Robbins et al., 2017)	Gradient *(ΔH/L)*
Hydraulic conductivity *(k)*	Hydraulic loading (gradually or instant)
Relative density *(RD)*	Bed shear stress *(τ)*

Table 2.7: Parameters categorized by group.

The influence of the different parameters can also be schematized using an influence chart. Figure 2.33 presents the influence of the different parameters related to the progression and sediment transport rate.

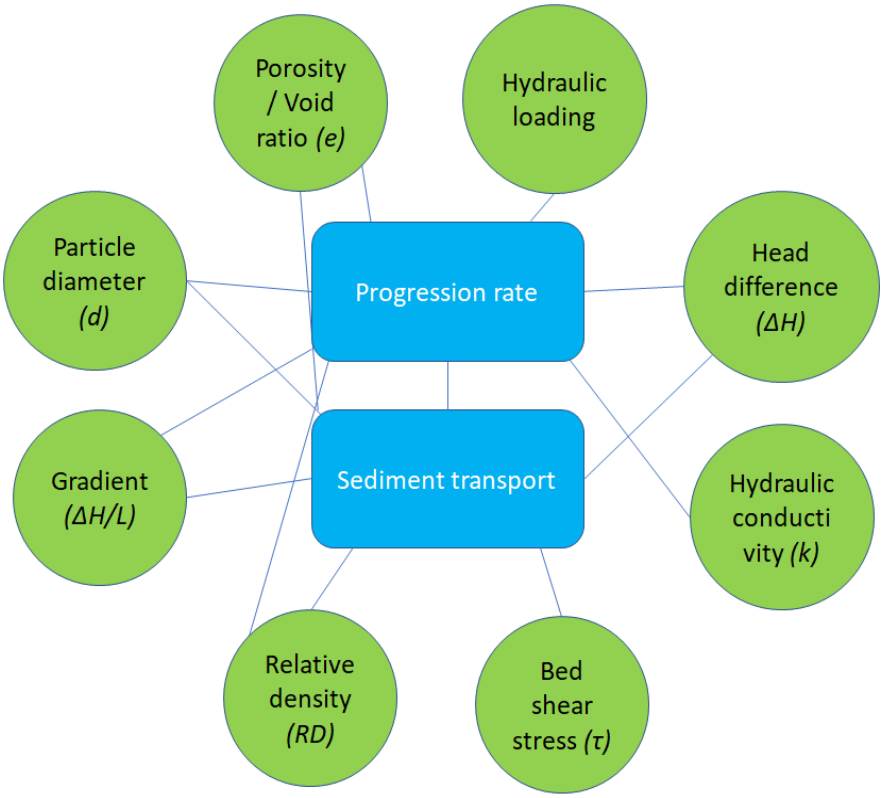

Figure 2.33: Influence chart of the different parameters.

After performing the experiments, the influence of the parameters should be seen from the progression and sediment transport rate. For example, if a test is performed with a larger hydraulic head, the progression rate should increase due to a larger hydraulic load. The basis for the hypothesis is derived from literature studies and results from past experiments.

The table below gives an overview of the different expected effects. A positive sign is given to those variables that enhance the progression rate, while a negative sign is given to those variables that reduce the progression rate. A plus/minus sign is given to the parameters which are balancing between an increase and a decrease of the progression rate.

	Effect on the progression rate	**Effect on the sediment transport rate**
Parameters		
Particle diameter *(d)* ↑*	+/-	+/-
Gradient *(ΔH/L)* ↑	+	+
Relative density *(RD)* ↑	-	-
Bed shear stress *(τ)* ↑	+	+
Hydraulic conductivity *(k)* ↑	+	+
Hydraulic head *(ΔH)* ↑	+	+
Hydraulic loading ↑	+	+
Porosity/void ratio *(e)* ↑	+	+

↑* (Increase of parameters)

Table 2.8: Overview of expected effects for the different parameters.

2.4.2 Equations for the progression and sediment transport rate

From the literature studies, different expressions were found for the progression and sediment transport rate. To show how the different parameters are related the following equations are given.

A general equation for the progression rate:

$$v_{c,avg} = \frac{dL}{dt} = \frac{(L - L_c)}{T_{progression}} \tag{2.19}$$

With

$v_{c,avg}$ = Averaged progression rate (m/s)
L = Horizontal seepage length (m)
L_c = Critical pipe length (cm)
$T_{progression}$ = Time of the progression phase (min)

The progression rate is defined as the difference in length divided by the progression time. Figure 2.34 presents the different parameters in a sketch of the setup (J. C. Pol et al., 2019).

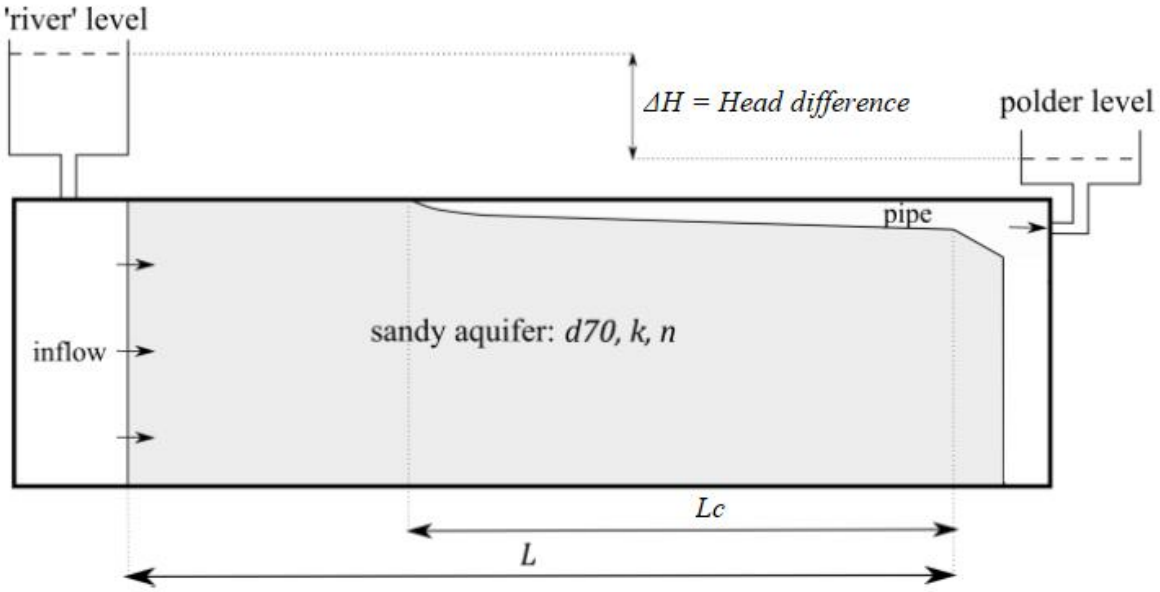

Figure 2.34: Experimental setup (Pol et al., 2019).

The equation for the sediment transport rate (m^2/s) is given by equations 2.20 and 2.21 (Cheng, 2004). The shear velocity can be expressed as a function of the bed shear stress and substituted in equation 2.22 (Schiereck, 2012).

(Cheng, 2004)
$$q_{v,C} = \Phi\, d\sqrt{\Delta g d} = 0.773\, D_*^{2.66}\, \Psi^4\, d\sqrt{\Delta g d} \tag{2.20}$$

or

$$q_{v,C} = 0.773 \left(\frac{d}{0.00004}\right)^{2.66} \left(\frac{u_*^{\,2}}{\Delta g d}\right)^4 d\sqrt{\Delta g d} \tag{2.21}$$

or

$$q_{v,C} = 0.773\left(\frac{d}{0.00004}\right)^{2.66}\left(\frac{\frac{\tau_b}{\rho_w}}{\Delta g d}\right)^4 d\sqrt{\Delta g d} \quad (2.22)$$

Once the formula for the bed shear stress is substituted in equation 2.23, equation 2.23 can be reduced to equation 2.24 (adapted formula). It shows that the sediment transport is a function of the particle diameter and the hydraulic radius (2.24).

$$q_{v,C} = 0.773\left(\frac{d}{0.00004}\right)^{2.66}\left(\frac{\frac{\cancel{\rho_w} \cancel{g} RS}{\cancel{\rho_w}}}{\Delta \cancel{g} d}\right)^4 d\sqrt{\Delta g d} \quad (2.23)$$

$$q_{v,C,adapted} = 0.773\left(\frac{d}{0.00004}\right)^{2.66}\left(\frac{RS}{\Delta d}\right)^4 d\sqrt{\Delta g d} \quad (2.24)$$

With:

$q_{v,C}$ =	Volumetric sediment transport rate per unit width (m^2/s) (Cheng)
$q_{v,C,adapted}$ =	Adapted volumetric sediment transport rate per unit width (m^2/s)
Φ =	Bedload transport rate (-)
d =	Particle diameter (m)
Δ =	Relative density $(=(\rho_s - \rho_w)/\rho_w)$ (-)
g =	Acceleration of gravity (m/s^2)
ρ_w =	Density of water (kg/m^3)
D_* =	Dimensionless particle diameter (-)
u_* =	Shear velocity (m/s)
R =	Hydraulic radius (area/perimeter) (m)
S =	Local slope of the pipe (dh/dx) (-)

The equation for the sediment transport (2.24) can be validated with the results from the experiments. The bed shear stress and the hydraulic radius can be calculated and substituted in equation 2.24. With the weight from the sand boil, which is formed during the piping experiments it is known how much sediment is transported.

The previous two sections give an overview of the different parameters which could be related to the progression and sediment transport rate. Analysis of the experimental results and observations during the experiments show if the ideas beforehand were correct.

3. Experimental setup

The former chapter highlighted the different performed experiments regarding backward erosion piping. After the literature studies, several questions remained concerning the progression and sediment transport rate. This chapter describes the experimental setup for the different small-scale experiments. In this thesis, three series of experiments were performed:

- Comparison of different configurations
- Study the effect of sand type (particle diameter, porosity)
- Study the effect of the hydraulic load (gradual increase)

The small-scale experiments were performed at the geotechnical laboratory of Deltares. In the following sections, the testing procedure is described and the results of the reference test (B25-229). The experiments are designed to examine the influence of various parameters. The last section (section 3.5) describes the challenges and strengths of the experimental setup.

3.1 Experimental setup

Figure 3.1 and Figure 3.2 provide an overview of the experiment setup. The setup consists of different parts: a PVC box, an acrylate plate with a circular opening as an exit point, and a cylinder placed on top where the eroded sand is collected. At the inflow side of the PVC box, a filter is placed to distribute the flow of water through the sand. This filter is also placed to prevent clogging up the inflow point. In the preparation phase, the setup is placed vertically with a filter at the bottom, so the sand sample is separated from the inflow point. This keeps the inlet point clean of sand.

The mentioned parts are the basic elements of the setup.

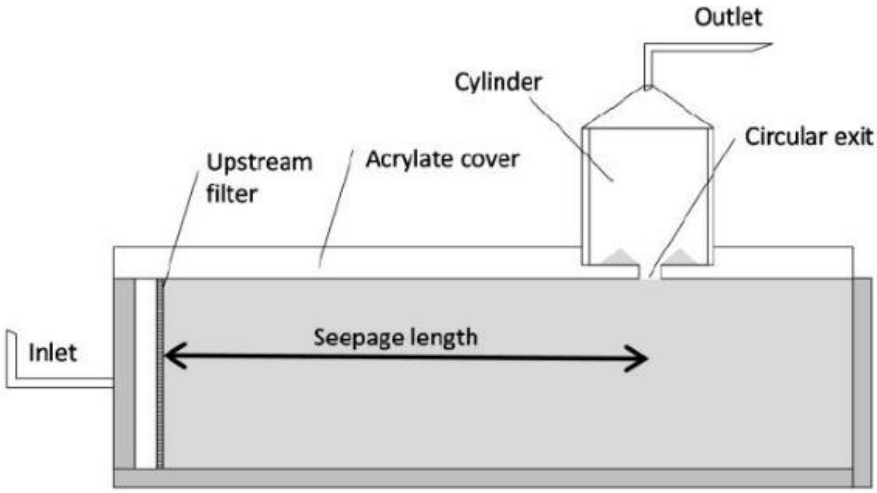

Figure 3.1: Cross-section of the experimental setup with the cylinder placed on top (Van Beek, 2015).

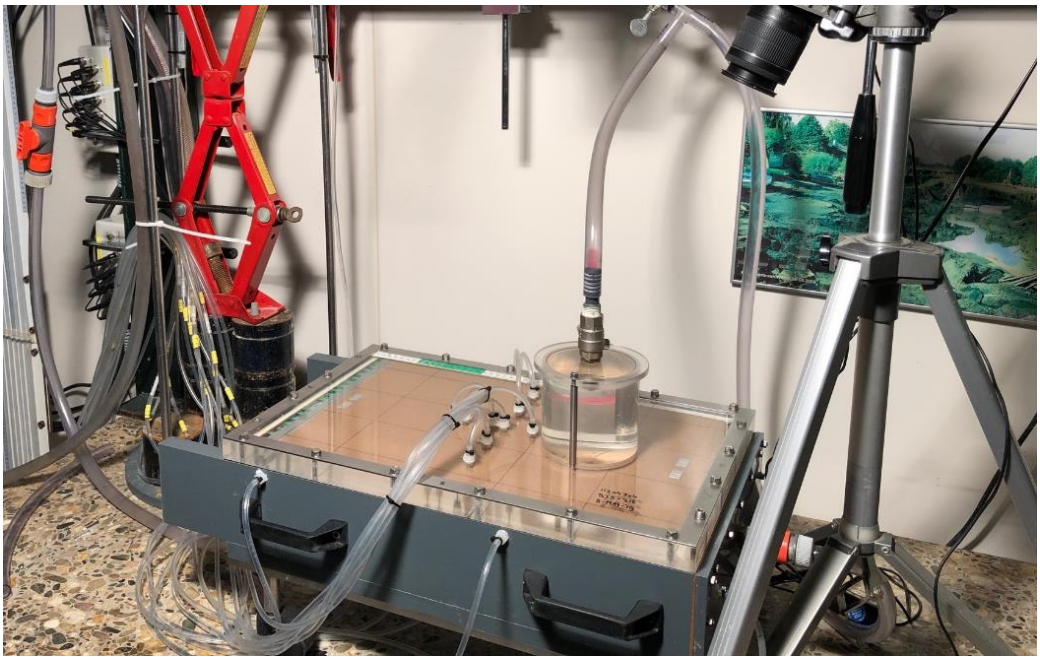

Figure 3.2: Photograph of the experimental setup filled with sand (Photographed by Van Klaveren, 2019).

On the left side of the setup, there is a water level reservoir which is kept constant by a pump during the experiments. The setup is connected to this level by a hose on the left side of the box. A bit further to the right on top of the acrylate plate, a cylinder is placed. The cylinder collects the eroded sand and serves also as the outflow point of the setup. When the level of the outflow point is equal to the water level of the reservoir there no flow of water through the setup. Once the downstream level is lowered a head difference is applied to the setup and the water starts to flow through the setup. Figure 3.3 gives a schematisation of the water flow through the setup.

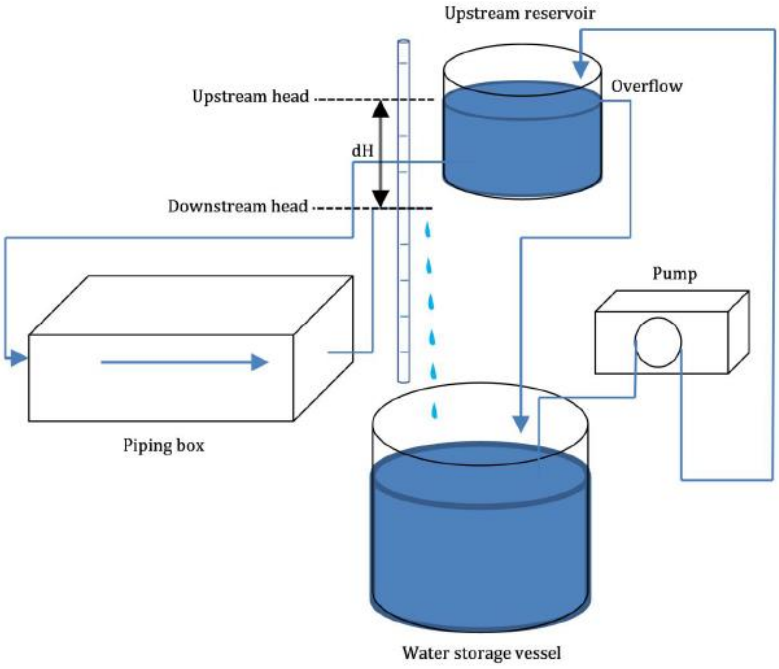

Figure 3.3: Schematisation of the water flow through the setup (Van Beek, 2015).

The cylinder placed on top of the acrylic plate is connected by a hose which transports the outflow of water to a bucket. The bucket is placed on top of a scale to measure the water flow. By measuring the mass of the water inside the bucket, the flow rate can be calculated over time (Figure 3.4).

Figure 3.4: Outflow point of the experimental setup (Photographed by Van Klaveren, 2019).

3.2 Sample preparation

The preparation of a new experiment starts with placing the box in a vertical position. When the box is placed vertically, the box is filled with de-aired water to around 50 - 60% of the total volume. This enhances the saturation of the sand and reduces the effect of trapped air. Before the sand sample is installed, the weight of the sand grains is constantly recorded to monitor the relative density (%) of the soil.

For the filling of the box, a small shovel is used to sprinkle the weighted sand carefully on top of the bottom filter. Once filled with sand, the sample is compacted to obtain the required

relative density percentage (≈ 80%). The compacting of the soil is performed by tapping with a hammer on the edge of the box. With this method, the grains settle and are more pushed towards each other. The sprinkling of the sand, the compacting, and the monitoring of the weight is a continuous process until the box is filled and the required relative density percentage is reached.

When the box is filled the lid can be placed on top of the box. The lid of the box is water tightened by a rubber seal. By this moment the sample preparation is completed, and the box can be positioned horizontally. Figure 3.5 presents two photographs of the filling process.

Figure 3.5: Sprinkling of the sand grains into the box (l), Filled setup with the lid on top (r) (Photographed by Van Klaveren, 2019).

When the box is placed horizontally (Figure 3.6) the lid on top of the cylinder can be installed. This connects the cylinder and the outflow of water to a bucket (Figure 3.4).

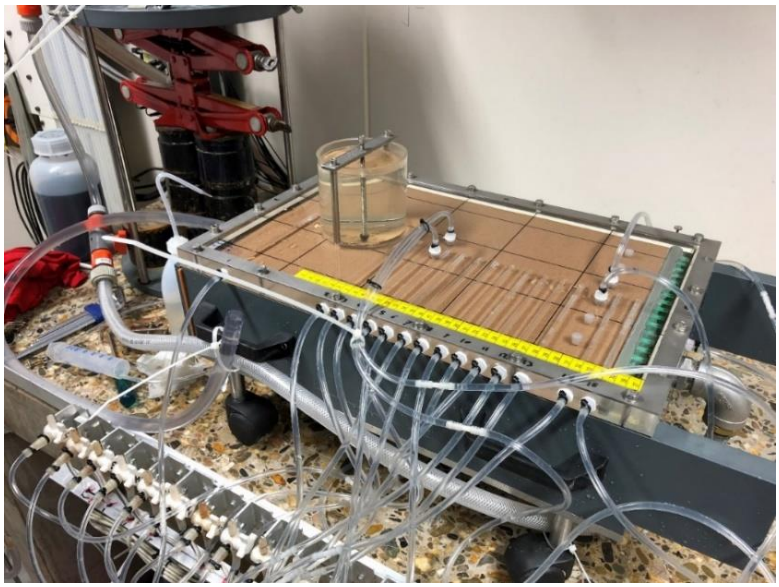

Figure 3.6: Box filled with sand and placed horizontally (Photographed by Van Klaveren, 2019).

After placing the lid on the cylinder, the measurement equipment can be installed around the setup. This contains the single-lens reflex cameras, an aluminium frame with laser and photographic lighting. The photographic lighting is installed to reduce reflection and shade on the numerous photographs taken by the cameras.

The laser is used to measure the depth of the pipe. A laser-diode sends a signal through the acrylate plate which is then reflected and received by a detector. By using the triangulation principle, the height can be calculated, which is the vertical distance from the diode to the deepest point of the pipe (Figure 3.7). What should be kept in mind is the measuring range. The laser has a measuring range from 70-170 mm and cannot be positioned too high. When the laser is positioned too far away from the setup, the signal cannot be received and no distance is measured.

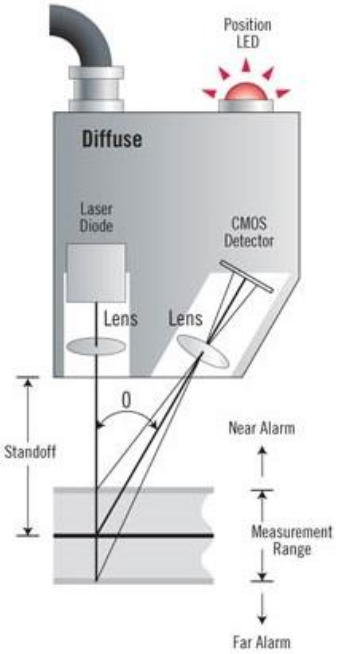

Figure 3.7: Laser triangulation principle (Azosensors, 2014).

Finally, the different tubes are de-aired, the pressure sensors are opened, and the hydraulic head is set to zero (ΔH=0 equals no flow). When the pressures are measured there must be no trapped air inside the tubes, this influences the results. The pressure sensors are connected to a computer where the instantaneous pressure is shown. Section 3.4.1 explains the application of the pressure sensors.

The setup is now prepared and equipped for experimenting (Figure 3.8). Appendix A gives a more elaborated checklist for the preparation phase.

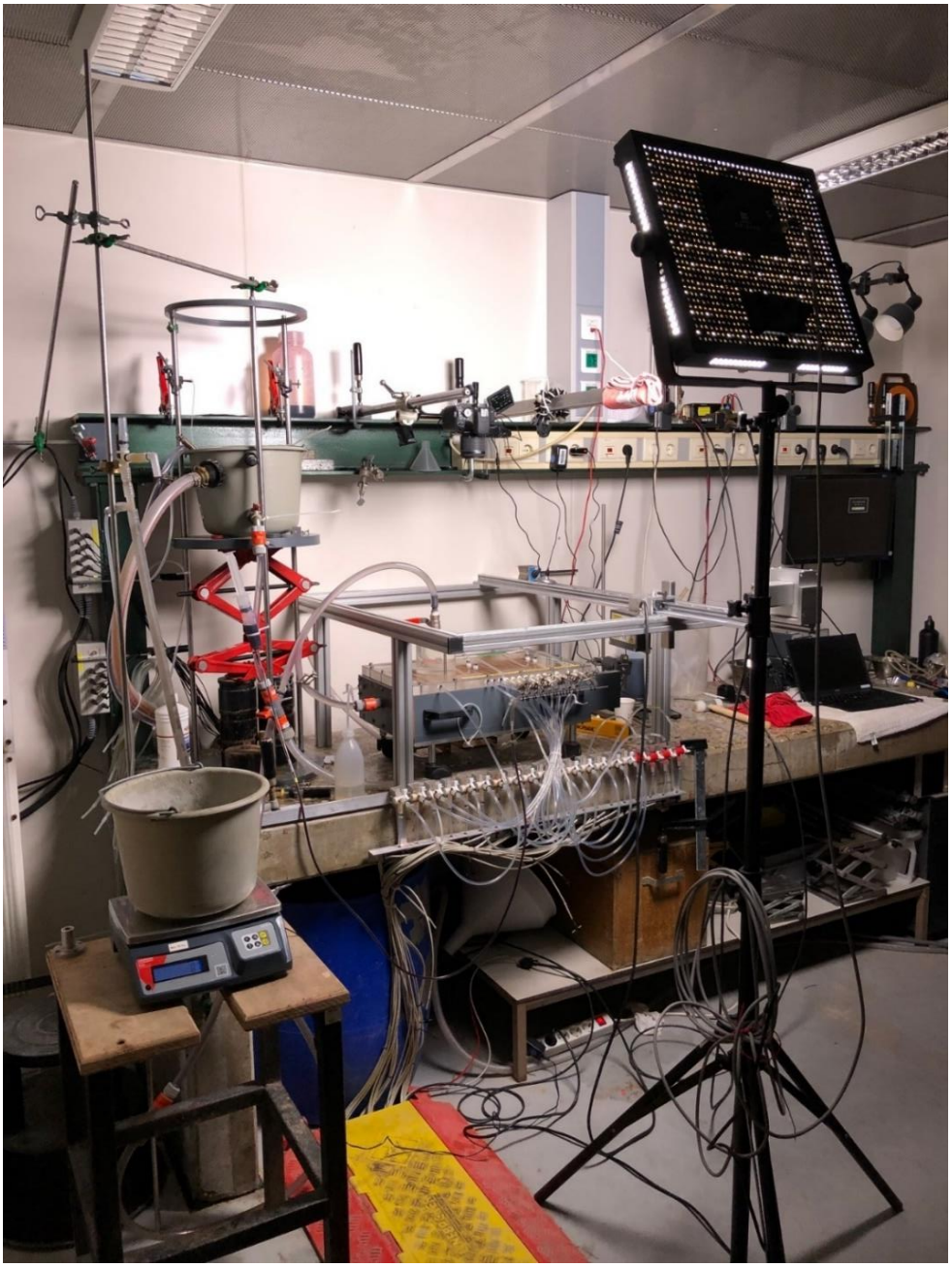

Figure 3.8: Experimental setup including measuring equipment (lights, cameras, scale, laser including frame) (Photographed by Van Klaveren, 2019).

3.3 Testing procedure

The experimental programme consists of 34 experiments which are divided into three series of experiments. The first series is designed to compare the effects of different configurations. The second series studies the effect of different sand properties and the last series examines the effect of hydraulic loading. Table 3.1, Table 3.2 and Table 3.3 give an overview of the different experimental series.

1st series of experiments: different configurations				
Test	**Date**	**Time**	**Code**	**Subject**
1	20-5-2019	14:22	B25-217	Reference to test silicone (new cover with pressure sensors)
2	22-5-2019	09:52	B25-218	Reference to test silicone
3	28-5-2019	09:43	B25-219	Reference to test silicone
4	3-6-2019	13.07	B25-220	Reference to test silicone
5	5-6-2019	10:25	B25-221	Test effect of silicone, smooth surface
6	2-7-2019	14:00	B25-222	Test effect of silicone, smooth surface
7	5-7-2019	13:47	B25-223	Smooth surface with filter cloth in the middle, first experiment with installed filter cloths
8	10-7-2019	11:30	B25-224	Silicone coating on the acrylic plate, but smooth surface between the two filter cloths
9	17-7-2019	15:10	B22-225	Silicone coating on the acrylic plate, but smooth surface between the two filter cloths
10	19-7-2019	10:37	B25-226	Silicone coating on the acrylic plate, but smooth surface between the two filter cloths
11	6-8-2019	14:40	B25-227	An extra layer of silicone coating with sand installed on both filter cloths and installation of injection points in every pressure sensor
12	9-8-2019	13:21	B25-228	Removed a bit of the extra layer of silicone coating with sand installed on both filter cloths
13	14-8-2019	08:57	B25-229	A small layer of silicone coating with sand installed on both filter cloths and installation of injection points in every pressure sensor (base experiment)
14	16-8-2019	14:10	B25-230	A small layer of silicone coating with sand installed on both filter cloths and installation of injection points in every pressure sensor (base experiment)
15	20-8-2019	14:07	B25-231	A small layer of silicone coating with sand installed on both filter cloths and installation of injection points in every pressure sensor (base experiment)
16	23-8-2019	09:45	B25-232	Experiment with an extra modification silicone.

Table 3.1: Overview of the first set of experiments: Comparing different configurations of the setup.

2nd series of experiments: different sand properties				
Test	**Date**	**Time**	**Code**	**Subject**
17	26-8-2019	13:09	B25-233	Reduction of the layer of silicon sand on the strip, new colour injection points at each pressure sensor, extra lines of silicone between the two filter cloths, *RD*=0.545.
18	30-8-2019	13:17	B25-234	**Base experiment** with extra layer silicone below each pressure sensor, *RD*=0.545.
19	12-9-2019	13:18	FPH-235	Base experiment with *RD*=0.74 and FPH sand, d_{50}=0.18 mm, sand from testing ground in Delft.
20	17-9-2019	09:43	B25-236	Base experiment with Baskarp B25 and *RD*=0.77.
21	19-9-2019	11:50	FPH-237	Base setup with FPH sand and *RD*=0.791, sand from testing ground in Delft.
22	1-10-2019	12:20	FS35-238	Base experiment with FS35 sand (d_{50}=0.42 mm)
23	3-10-2019	10:52	FS35-239	Base experiment with FS35 sand (d_{50}=0.42 mm)
24	8-10-2019	13:06	FS35-240	Base experiment with FS35 sand (d_{50}=0.42 mm) & *RD*=0.49
25	11-10-2019	12:57	FS35-241	Base experiment with FS35 sand (d_{50}=0.42 mm) & *RD*=0.49
26	22-10-2019	10:15	B25-243	Base setup with B25 sand and *RD*=0.79
27	05-11-2019	11:09	B25-244	Extra experiment with B25 sand and *RD*=0.55
28	08-11-2019	11:00	B25-245	Extra experiment with B25 sand and *RD*=0.55
29	11-11-2019	10:03	FS35-246	Base experiment with FS35 sand and *RD*=0.72

Table 3.2: Overview of the second set of experiments: Comparing different sand properties.

3rd series of experiments: effect of hydraulic loading				
Test	**Date**	**Time**	**Code**	**Subject**
30	17-10-2019	14:10	FS35-242	FS35 Overloading experiment (1.2 * ΔH_c) & *RD*=0.71
31	15-11-2019	10:00	B25-247	B25 Overloading experiment (1.2 * ΔH_c) & *RD*=0.8
32	15-11-2019	14:00	B25-248	B25 Overloading experiment (1.2 * ΔH_c) & *RD*=0.8
33	19-11-2019	11:00	B25-249	B25 Overloading experiment (1.1 * ΔH_c) & *RD*=0.8
34	19-11-2019	14:00	B25-250	B25 Overloading experiment (1.1 * ΔH_c) & *RD*=0.8

Table 3.3: Overview of the third series of experiments: Effect of hydraulic loading.

3.3.1 Soil sample

Baskarp B25 is the type of sand which is used in the first set of experiments. It has a d_{50} of 0.22 mm and can be classified as slightly silty. This type of sand originates from Sweden and is often used in laboratory experiments (Appendix B). The sieve curve shown in Appendix B1 displays that rather fine sand is used in the first experiments. In further experiments, a coarser and a finer sand type are used to compare the progression and sediment transport rate.

Appendix B2 presents the grain size distribution of the two other sand types (FS35 and FPH). FPH sand is very fine sand which originates from the testing ground in Delft and FS35 is a coarser standard filter sand type. Table 3.4 shows the three different types of sand.

Sand type	***d_{50} (mm)***	***No. of experiments***
FPH	0.18	2
Baskarp B25	0.22	26
FS35	0.42	6

Table 3.4: Overview of used sand types.

The testing ground (in Dutch= ‘proeftuin’) is a location in Delft where a large-scale piping experiment was performed in 2019 (J. Pol et al., 2020). A dike with a height of 1.8 metres was built on top of a clay blanket layer and a sandy aquifer. The sandy aquifer represents the FPH-sand layer with a d_{50} of 0.18 mm. This experiment was performed to study the process of piping under realistic conditions.

3.3.2 Configuration of the setup

The goal of the first series of experiments is to compare different test configurations and to obtain a base experimental setup for the remaining series. In the first series of experiments, the configuration of the setup is changed regularly. Table 3.1 describes the changes in the setup from experiment 4 to 18. When the configuration was changed one or two reference tests were performed to study the effect of the changes. In experiment 18 the last configuration changes were performed and the base setup was found.

The application of the silicone layer and the filter cloths were the two major changes in the configuration of the setup. The silicone layer on the acrylate plate was initially installed to represent the clay layer inside the dike however, the results showed that there was no significant effect on the critical head.

The filter cloths positioned in the middle of the acrylate plate played an important role in the configuration of the setup. Initially, the experiments were performed without the filter cloths and affected the development of the pipe. Figure 3.9 presents the development of the pipe in an experiment setup without filter cloths.

Without the filter cloths, the pipe has a wider meandering shape and does not develop below the pressure sensors.

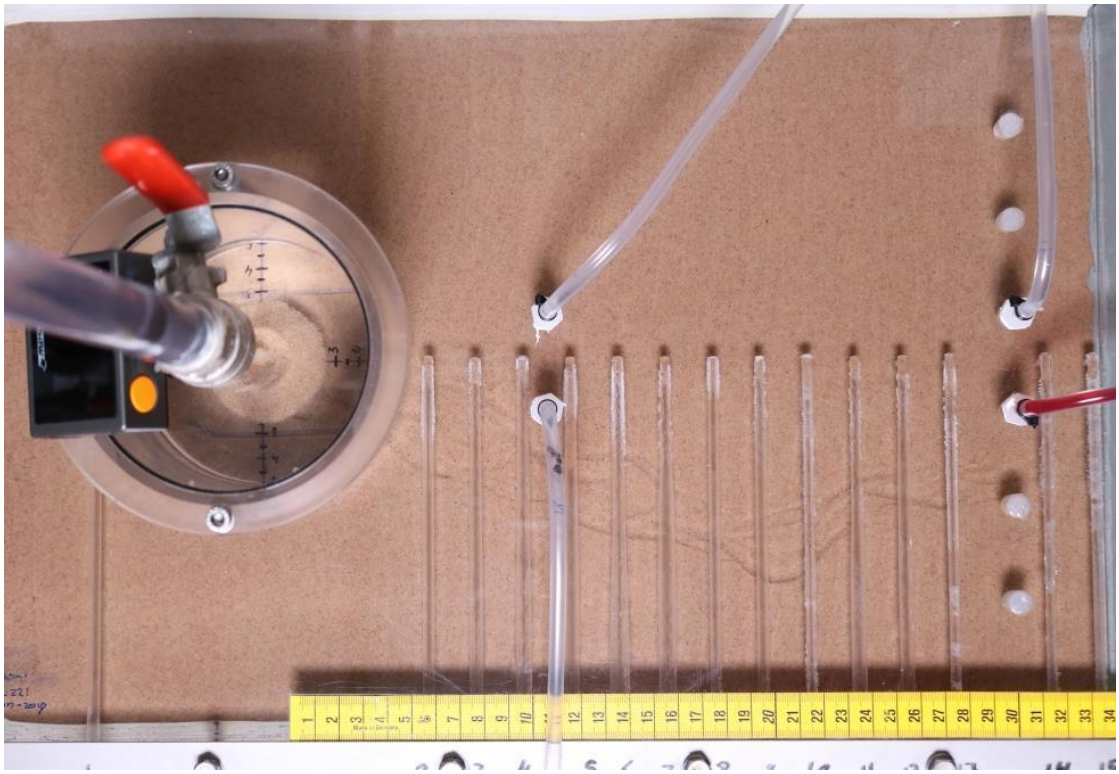

Figure 3.9: Top view of the pipe without filter cloths in the middle (Experiment B25-221).

The filter cloths were designed to guide the pipe through the middle of the box. When the pipe grows through the middle of the box the pressure sensors can measure the pressure inside the pipe. Figure 3.10 presents a top view of the box where the cloths and pressure sensors are shown.

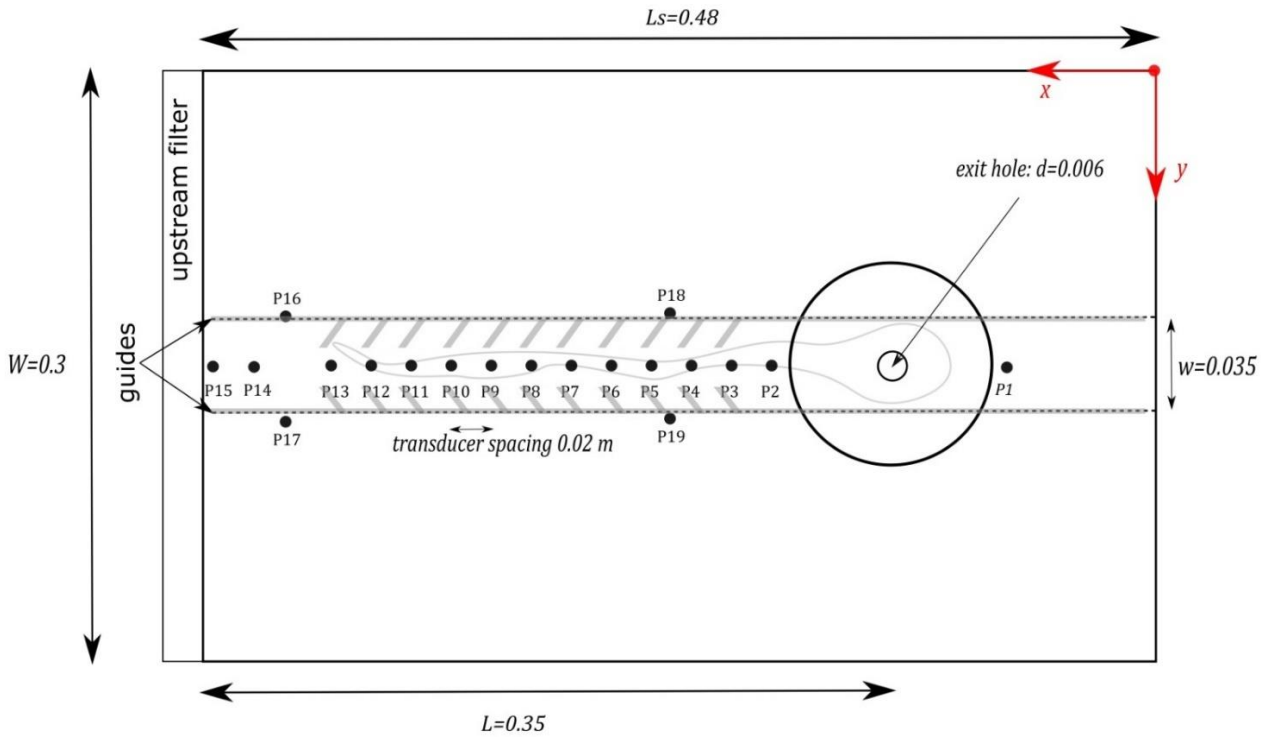

Figure 3.10: Schematization of the acrylate plate including two filter cloths and 19 pressure sensors (Drawn by Pol).

After the installation of the filter cloths (experiment 7) the pipe was guided through the middle, but still not growing below the pressure sensors. Instead, the pipe developed along the filter cloth due to its relatively smooth surface. To solve this, the filter clothes were adapted with a small layer of silicone and a thin layer of sand to increase the resistance. Subsequently, a new experiment was performed with the pipe growing below the pressure sensors.

Section 3.3.3 presents the first results of experiment B25-229 and is chosen as the reference test from the first series of experiments.

3.3.3 Procedure of the reference test (B25-229)

Experiment B25-229 starts with the standard procedure:

1. Preparation of the sample
2. The positioning of the lights
3. The positioning of the cameras
4. The positioning of the laser including frame
5. De-air the tubes
6. Levelling of the inflow and outflow levels

The experiment starts with creating a head difference of one cm every five minutes. When a head difference is applied, the water starts to flow from high to low and the pipe develops over

time. After approximately one or two centimetres of head difference, an outflow of water is observed and captured by the bucket on the scale. These are the first observations and measurements of the flow rate.

In every experiment, the head difference is stepwise increased until the critical head difference is obtained. When the head difference is increased, the grains are transported and the pipe length increases. After some minutes an equilibrium is found and the pipe stops growing (no sediment transport). This is the moment when the head difference is increased again. The critical head difference of experiment B25-229 is found at 7.05 cm. At this head level, the length of the pipe continuously grows until the pipe is fully developed (breakthrough). The head difference is not raised any further.

Each experiment consists of four parts:

1. Measuring the pipe length
2. Depth measurement (laser)
3. Dye injection to follow the flow
4. Collecting the sand boil

During an experiment, the observations are reported to follow every development in time. Appendix C1 shows the observations of experiment B25-229. When the pipe is fully developed (L≈34 cm), the head difference is lowered and the experiment is finished. From this moment a depth measurement can be performed (laser) and a dye injection to follow the flow. As a final step, the valves are closed, and the lid of the cylinder can be removed. The sand boil is collected in a small bucket and placed inside the oven to dry.

The total performance time including preparation and cleaning up is approximately five hours per experiment.

3.4 Results of the reference test (B25-229)

This section presents the characteristic results (pipe length, flow rate, progression rate, pipe depth) from experiment B25-229. The results are presented in different graphs to illustrate the development of the pipe over time (Appendix C2).

Figure 3.11 presents the development of the pipe related to the head difference. The pipe is fully developed after 83 minutes with a critical head of 7.05 cm. After 55 minutes the head difference remains constant at the level of 7.05 cm. It can be observed that the pipe length further progresses until failure (after 83 minutes).

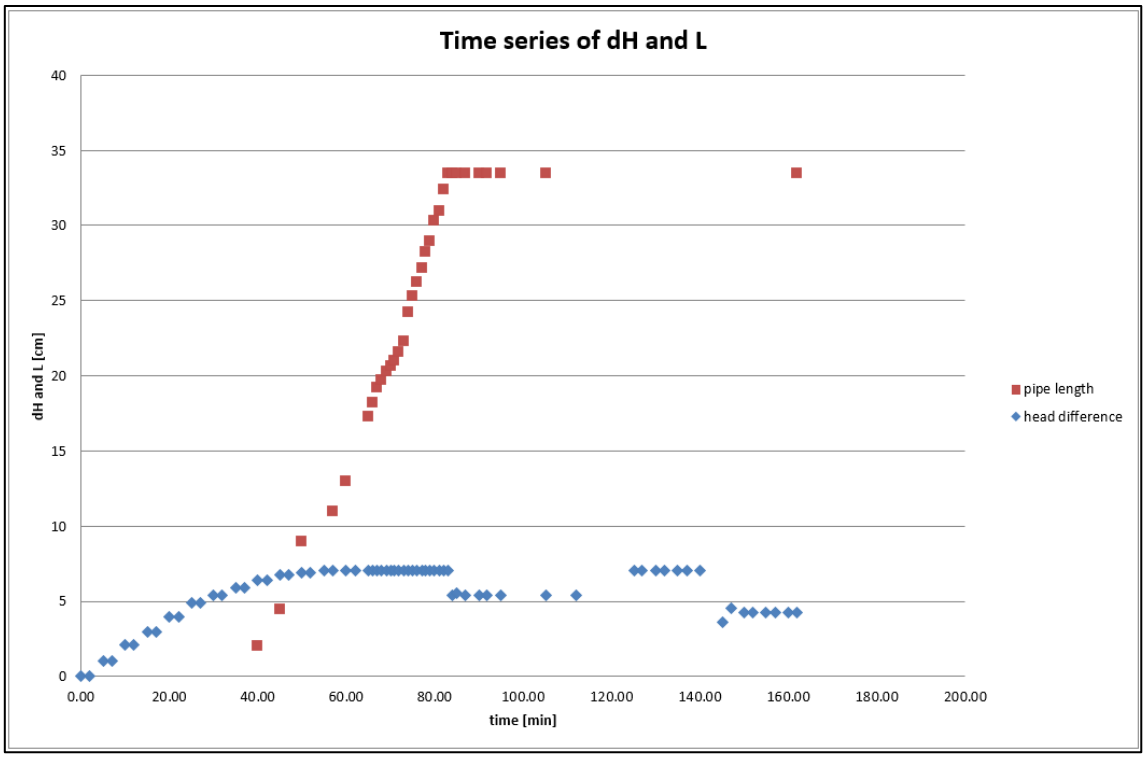

Figure 3.11: Development of the pipe length related to the head difference (B25-229).

Further results of the reference test (B25-229) are presented in the next sections. This contains the results of the pressure sensors, depth measurements, dye injection and collecting of the sand boil.

3.4.1 Results of the pressure sensors (B25-229 and B25-232)

The pressure sensors are positioned every 2 cm in the acrylate plate. This has the advantage to measure the pressure inside the soil sample and preferred inside the pipe. Pressure sensor 2 (P2) is the first sensor outside the cylinder and pressure sensor 15 (P15) is the last sensor at the end of the PVC box. Figure 3.12 presents a top view of the setup including the numbering of the pressure sensors (metal strip).

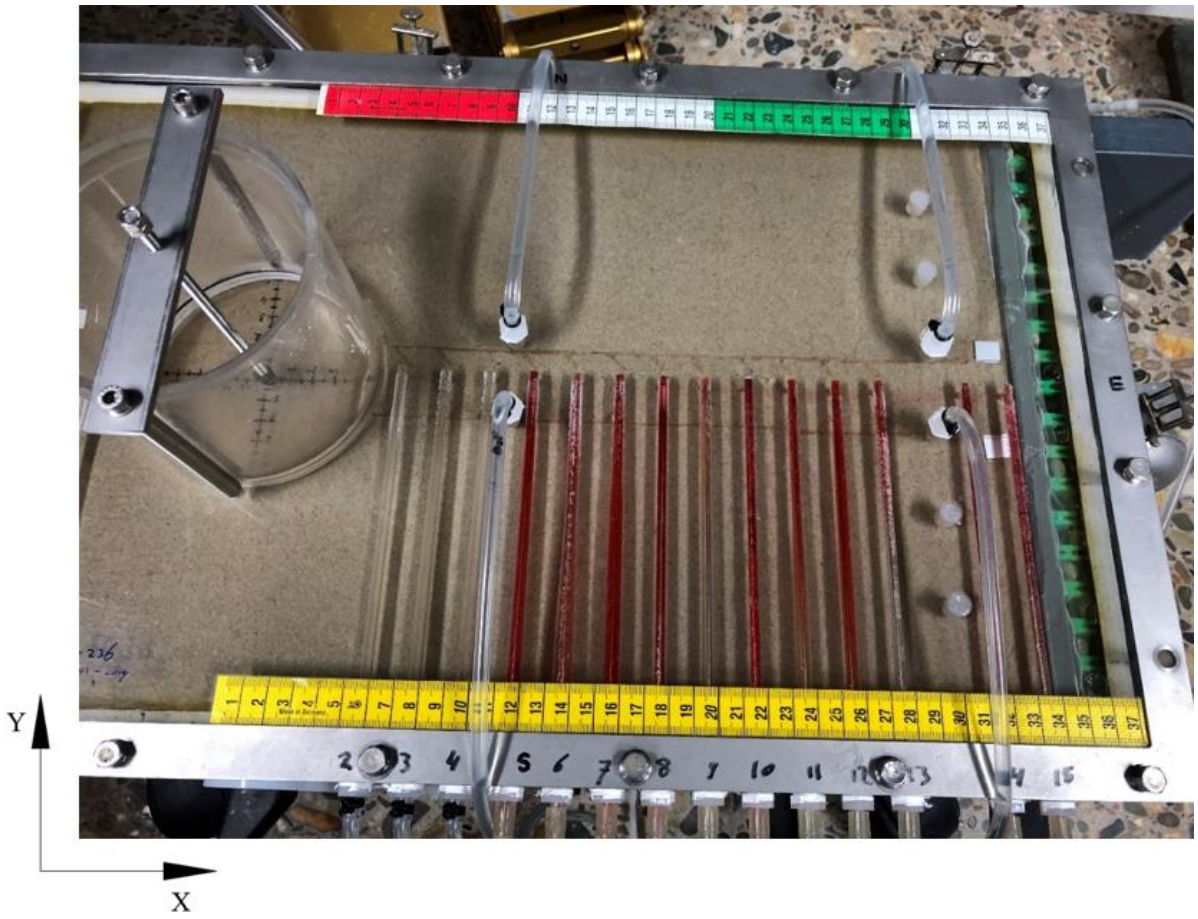

Figure 3.12: Top view including the location of the pressure sensors (bottom metal strip).

Figure 3.13, Figure 3.14 and Figure 3.16 present the characteristic graphs of the pressure sensors. This contains the head difference and the gradients on the soil sample.

Figure 3.13 shows the pressures (by applying a head difference 1-6 cm) inside the soil sample during the experiment. The stepwise increase of the head difference (y-axis) can be observed in the period from 0-3000 seconds (x-axis).

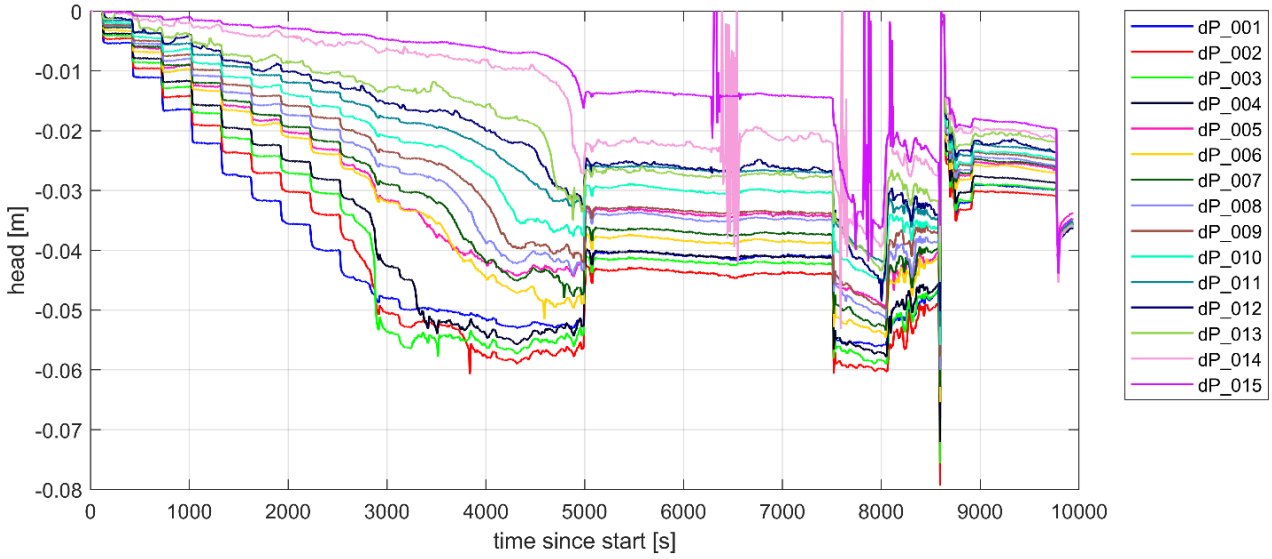

Figure 3.13: Measured head difference by the pressure sensors (B25-229).

Figure 3.14 shows the hydraulic gradient between two pressure sensors. The hydraulic gradient is defined as dh/dx between two transducers (y-axis). The pipe in experiment B25-229 grows below pressure sensor 3 and 4, and this can be observed by two peaks at ***t≈3000*** and ***t≈3400 s***. If the pipe grows below the sensor a peak is generated.

The x-axis presents the time since the start of the experiment. The column at the right side of the figure shows all the different gradients, coupled to all the 15 sensors (metal strip).

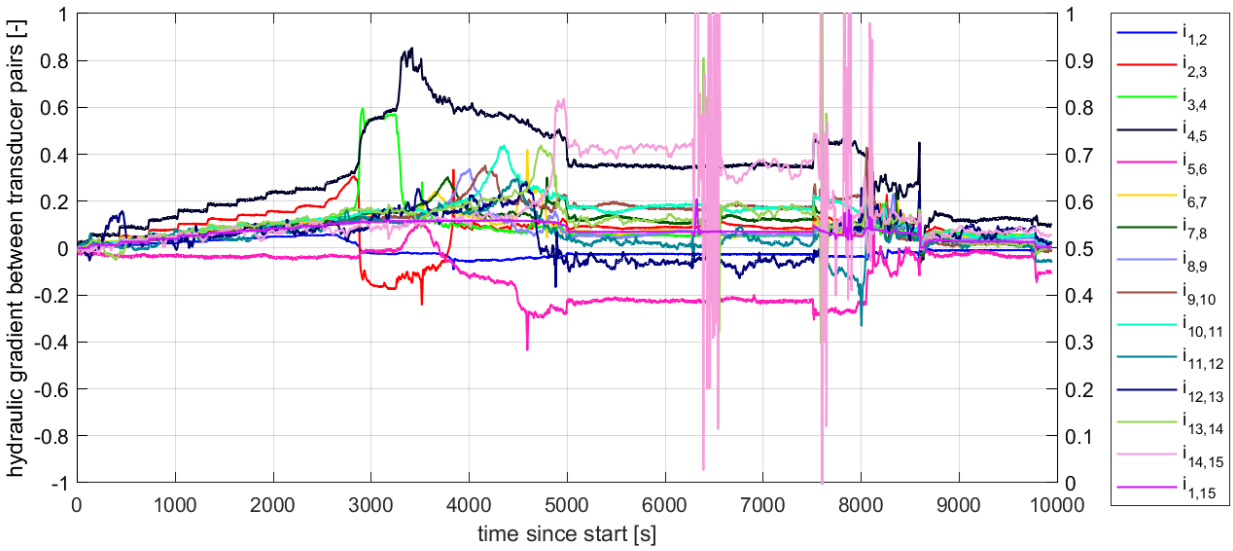

Figure 3.14: Hydraulic gradient between two transducers (B25-229).

For a better understanding of the two previous graphs (Figure 3.13 and Figure 3.14) the head difference and the hydraulic gradient are explained by an example. Figure 3.15 presents the hydraulic head difference and gradient for two pressure sensors. The left graph shows the measured pressures inside the soil sample. The right graph presents the gradient, which is defined by $\Delta H/\Delta x$.

The distance between the pressure sensors is two centimetres. Therefore, a head difference of one-centimetre results in a hydraulic gradient of 0.5.

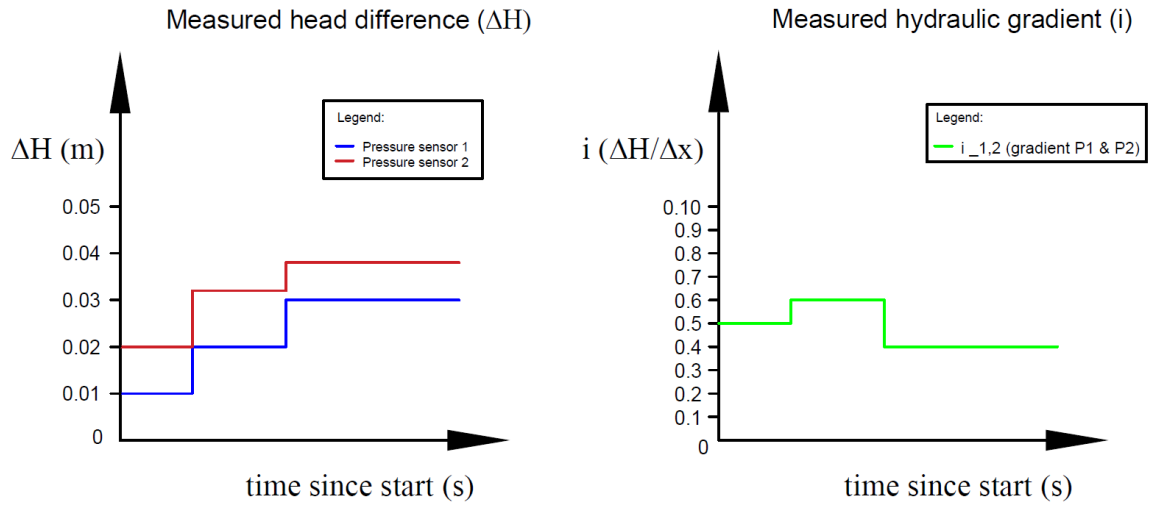

Figure 3.15: Example of measured head difference (l) and hydraulic gradient for 2 sensors (r).

In experiment B25-229 the pipe did not completely follow the sensors. For comparison with Figure 3.14, a graph of experiment B25-232 (Figure 3.16) is presented. In experiment B25-232 the pipe developed below five sensors. More peaks can be observed at sensor 2, 6, 9, 13 and 14.

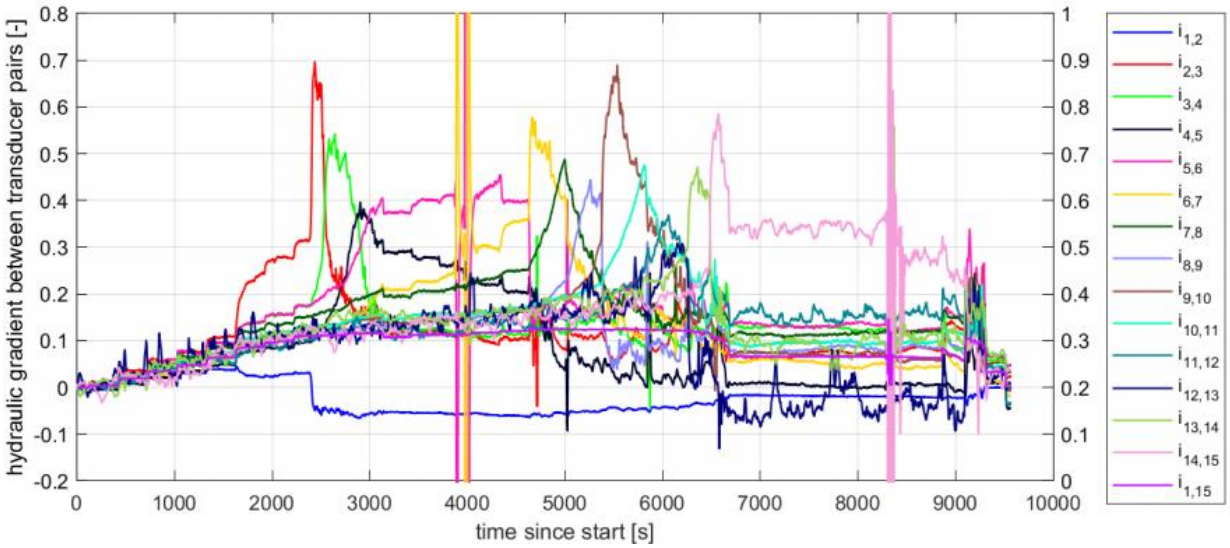

Figure 3.16: Hydraulic gradient between two transducers (B25-232).

3.4.2 Results of the depth measurements (B25-229)

For the depth measurement of the pipe, a laser is used. During an experiment, one or two laser measurements were performed to measure the depth of the pipe. Figure 3.17 presents the cross-section of the pipe at two locations. The laser scan was performed at 10:30, right after the pipe was fully developed.

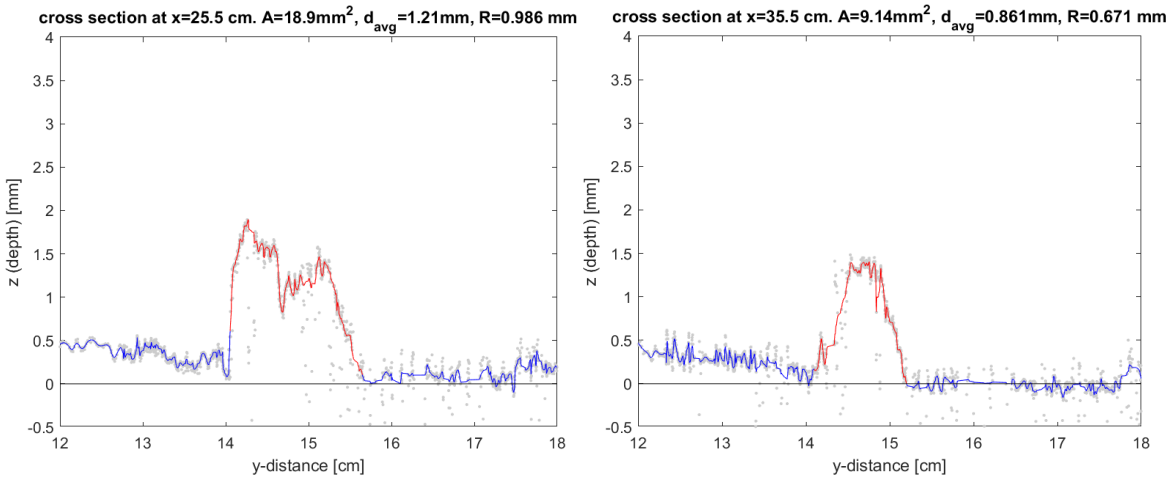

Figure 3.17: Cross-section of the pipe at location x=25.5 (l) and x=35.5 (r).

The red line in the figures above is used to calculate the cross-sectional area, the average depth, and the hydraulic radius of the pipe. The blue line presents the total measurement from the laser. During the laser scan, 12 cross-sections were made at 12 different locations, from the beginning of the pipe until the end. These locations all have a graph as presented above.

From these graphs: the area, average depth, and the hydraulic radius (area/perimeter) are calculated. Figure 3.18 presents the averaged depth, hydraulic radius, and the cross-sectional area of the pipe at each location.

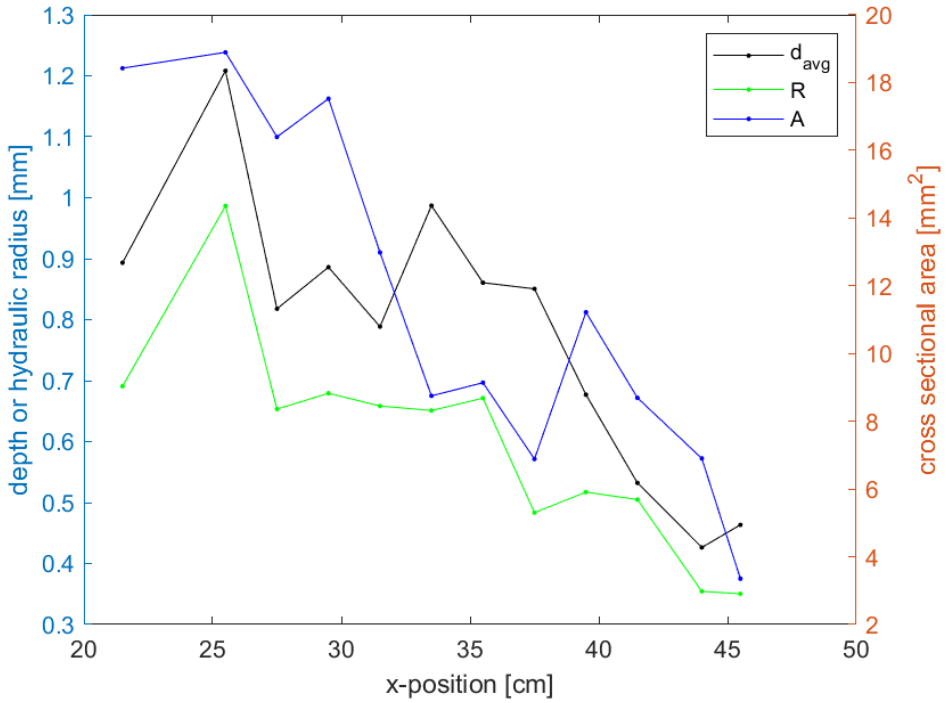

Figure 3.18: Area, depth, and hydraulic radius of the pipe related to the location (B25-229).

Figure 3.19 presents a top view of the pipe while indicating the depth. The deepest point of the pipe is almost 2 mm and is located between 25-30 centimetre from the top of the PVC box.

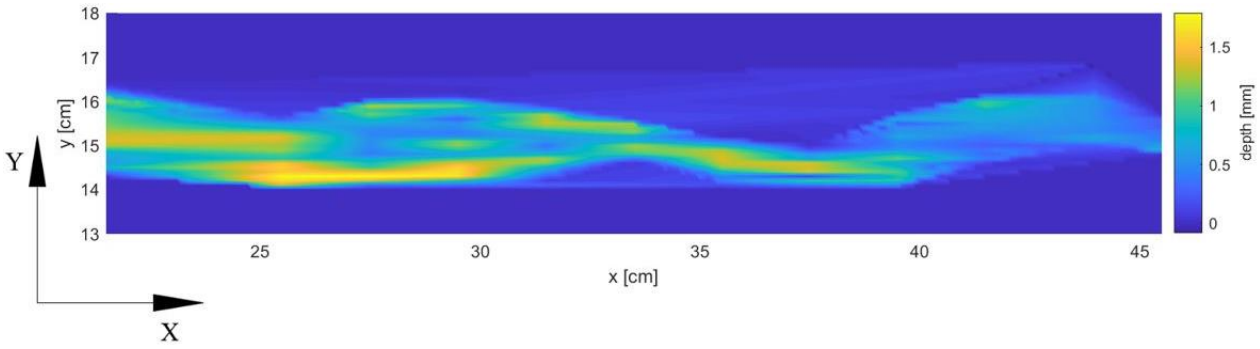

Figure 3.19: Top view of the pipe with a depth profile (B25-229).

3.4.3 Dye injection (B25-229)

At last, a red dye injection is performed to follow the flow through the pipe. With a single-lens reflex camera, a short video is made to analyse the flow velocity. This video is later cut up in short images to enlarge the movement of the colour. The dye injection is made at pressure sensor 14 near the end of the pipe. Figure 3.20 presents the start of the dye injection and Figure 3.21 shows the dye injection after 3 seconds.

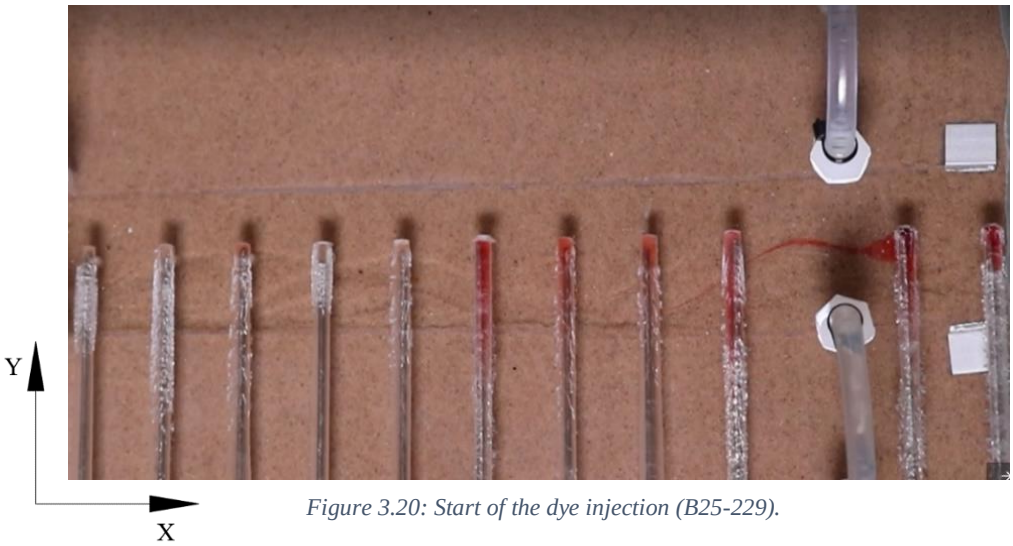

Figure 3.20: Start of the dye injection (B25-229).

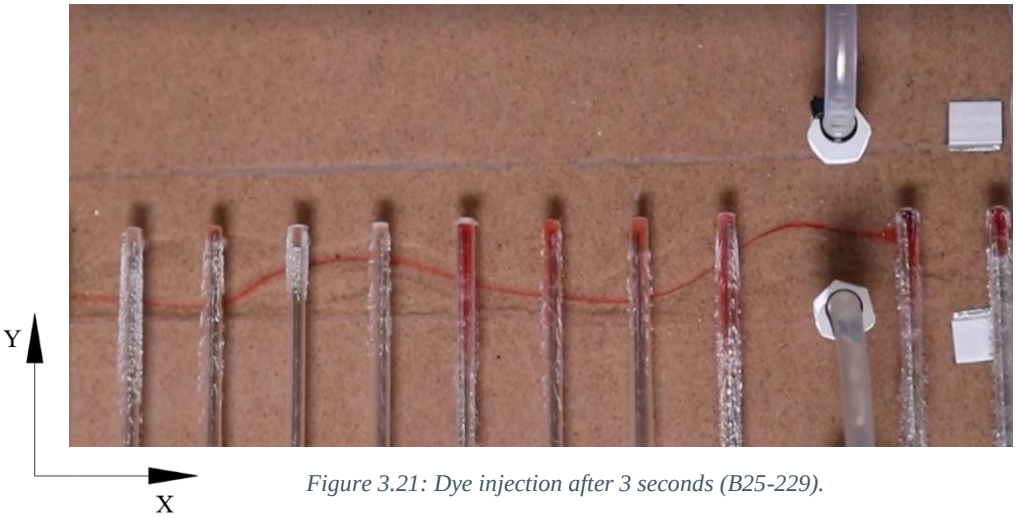

Figure 3.21: Dye injection after 3 seconds (B25-229).

3.4.4 Collecting the sand boil (B25-229)

Finally, the sand boil is collected. By collecting and measuring the soil boil, the sediment transport rate can be determined. The sand boil has the shape of a crater and contains the transported sand from the pipe. A larger crater equals more sediment transport, a smaller crater implies less sediment transport. The sediment transport rate is, therefore, a function of the crater mass.

When the pipe starts developing, a small crater is formed at the exit opening. The cylinder on top of the acrylate plate collects the sand from the pipe. After removing the lid of the cylinder, the sand is captured and measured. The sand crater of experiment B25-229 weights 65.05 g.

The weight of this crater is not representative of all experiments, because there was a small crater (radius=1.5 cm) formed in the preparation phase. The weight of the crater is, therefore, a combination of eroded sand from the pipe and sand from the sample. The height and radius of the crater are also measured after the experiment.

Experiment B25-229 has a crater radius of 4.3 cm and a height of 15.2 mm. Figure 3.22 presents the sand boil inside the cylinder during the experiment.

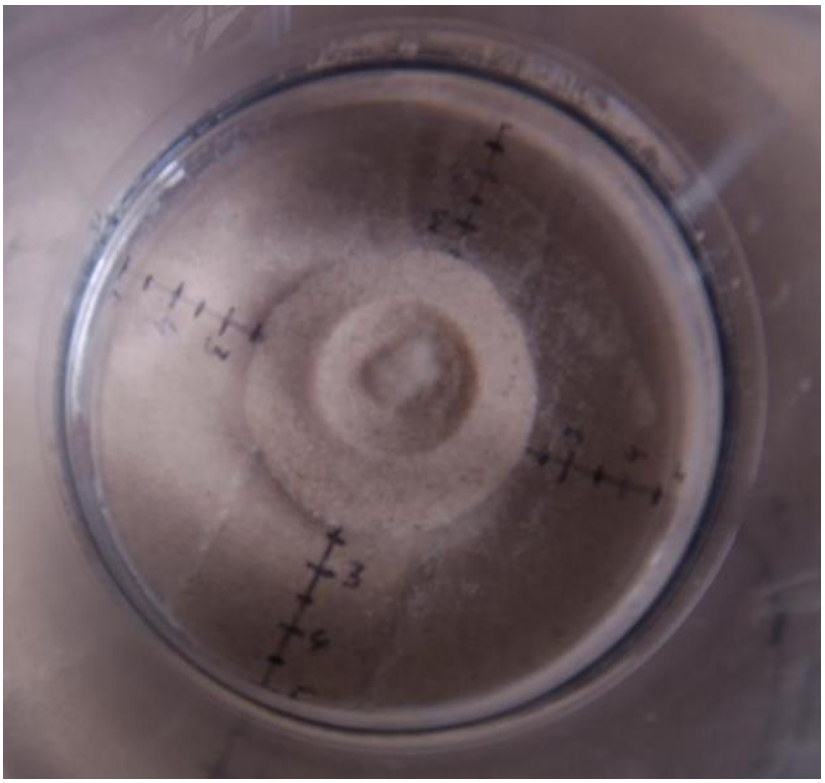

Figure 3.22: Top view of the sand boil inside the cylinder (B25-229).

3.5 Implications of the experiments

During the piping experiments, many challenges had to be overcome to collect the data and measure the dimensions of the pipe. This section describes the challenges and strengths of the experimental setup.

The experimental setup is adapted after several experiments to obtain the most optimal situation for the pipe to develop under the sensors. To measure the development of the pipe, the pipe was guided through the middle of the two filter-cloths. The most optimal situation is when the pipe develops through the middle of the two filer-cloths and directly below the pressure sensors. With this configuration, the pressure can be measured inside the pipe. Lines of silicon were placed near each pressure sensor to guide the pipe through the middle (Figure 3.10). This modification forces the pipe to develop in a straight line below the pressure sensors.

Another challenge was the functioning of the pressure sensors and the laser. In the first experiments, the laser was not able to measure the depth of the pipe. The signal that was sent from the diode was not received by the detector. This was probably due to the measuring range. After installing another laser with a smaller measuring range, the depth of the pipe could be measured.

During the first stages of the experiments, the pressure sensors displayed some uncommon values in the graphs. This was due to the high sensitivity of the sensors. In the preparing phase of the sample, water was often spilt on the floor and the wires of the system. After placing a layer of tape, the sensors were protected from water and performing better. What also influenced the measured values of the pressure sensors was trapped air inside the tubes. For this reason, the tubes were de-aired after approximately 5 experiments. After these adjustments and developments, the measurement equipment was up and running.

In contrast, the photographing and recording of the experiments went quite well and effective. In total two single-lens reflex cameras were applied are positioned above the setup and another GoPro camera was monitoring the sand boil. The first camera takes a photograph every 10 seconds and monitors the development of the pipe (top view). The second single-lens reflex camera was applied to record a macro video of the pipe. The development of the pipe is highly visible because of the high quality of the cameras.

Related to the monitoring of the sand boil is the removal of the plug in the exit hole. There can be pressure inside the soil sample, which is released when the plug is removed. If the plug is removed too rapidly a small sand boil is formed and sand is transported out of the exit. It is essential to remove the plug very carefully not to disrupt the soil sample.

The documentation of the crater dimensions and pipe length also went remarkably well. For every timestep during the experiment, the radius and length were documented to monitor the sediment transport of the pipe. What was observed during the experiments is that the sediment transport is influenced by the head difference. The critical head difference is found by raising the head difference in steps of 1.0, 0.5 and 0.2 cm. The head difference needed to be raised very carefully because in two or three experiments the head difference was raised too quickly and passed the critical head difference. This could later be observed by the dimensions of the crater and the sudden increase in pipe length. A head difference of 1 mm could already make the difference between continuous transport or not (very sensitive).

4. Results and Analysis

Chapter four presents the results and the analysis from the different experimental series. The results of the experiments are globally presented in the second section. In further sections, the results are presented and analysed on a more detailed level.

The former chapter explains the experimental setup in combination with the different measurement techniques. In addition to the last chapter, the results of the experiments are now analysed to answer the different research questions. To determine the relations between the progression and sediment transport rate the results of the experiments are compared amongst each other and related to the hypothesis beforehand.

This chapter includes the following topics:

- Presentation of the results
- Analysis of the effect of sand type (grain size, porosity)
- Analysis of experiment FPH-235
- Comparison of the results with the hypothesis

In experiment FPH-235 the pipe developed below several pressure sensors, which indicates that the local hydraulic gradient could be properly measured. Experiment FPH-235 is therefore selected for further analysis.

4.1 Strategy of the analysis

The analysis of the experimental results is divided into different phases. Phase one is the first phase out of four and consists of collecting data. There is a large quantity of data available which needs to be collected first, to be analysed later. There is chosen to analyse the first two experimental series (experiment 1-29). The overloading experiments mentioned in Table 3.3 are not further studied, but will be analysed in future work by J. Pol.

After the selection of the data, a global analysis can be applied to the selected experiments. From the different plots of the various parameters, relations can be observed around how the progression rate is influenced. The global analysis includes the calculation of the critical head difference (Sellmeijer) and calculating the mass of the sand crater.

For the extensive analysis, experiment FPH-235 is selected and calculated with the different models (Cheng sediment transport, dilatancy, mass). When all the results are gathered from the global analysis and the extensive analysis, the results are compared to the hypothesis. The relation with the shear stress is made as well. Figure 4.1 presents an overview of the analysis scheme.

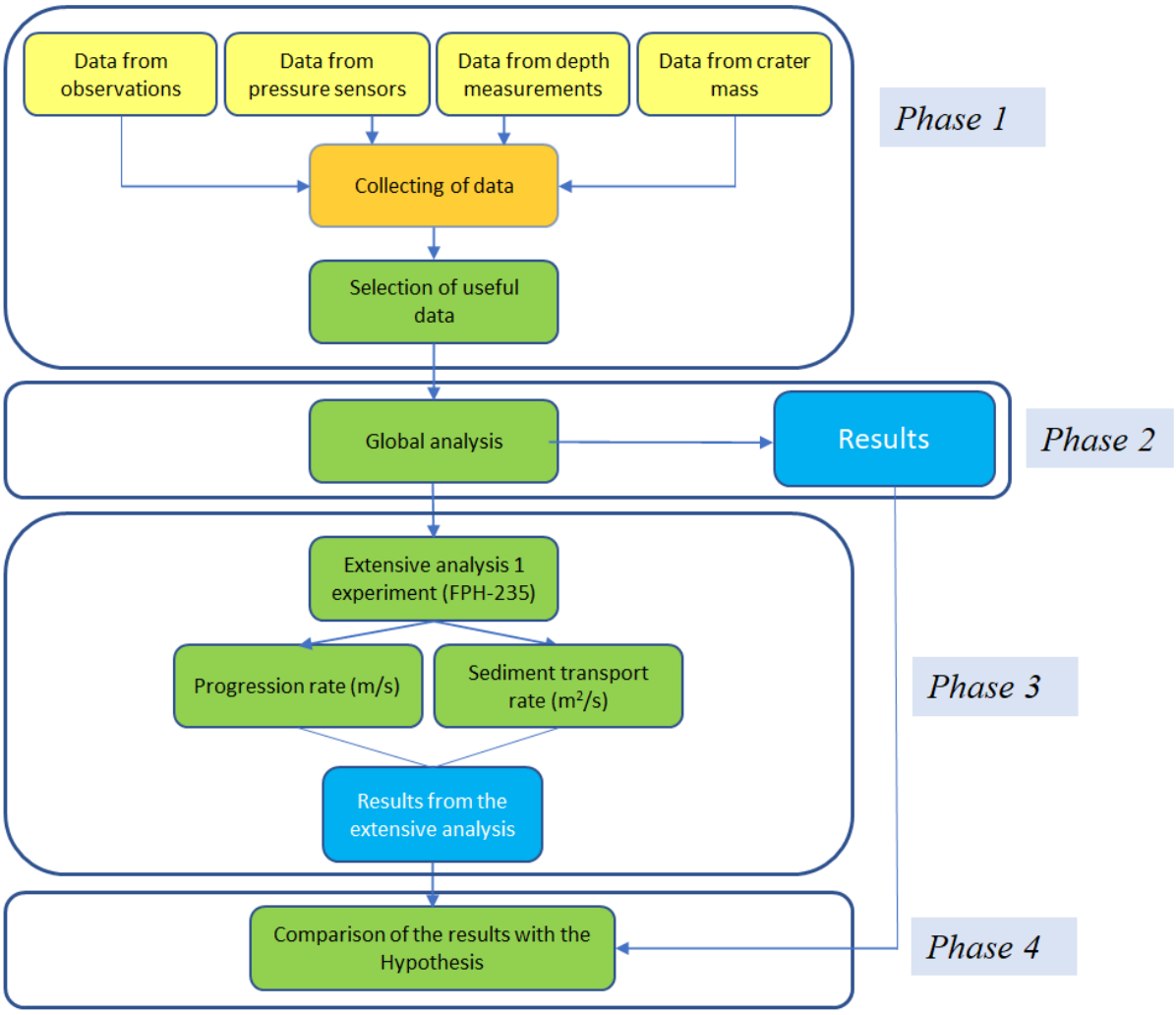

Figure 4.1: Overview of the analysis scheme.

4.2 Experimental results

In total 34 experiments were performed over a period of six months. Three different types of sand were used with a combination of two different values for the relative density (0.8 and ≈ 0.5). The experiments are designed to examine the influence of different parameters. Table 4.1 presents an overview of the selected experiments. The red marked experiments are not included in the analysis. In these experiments, the pipe developed sideward, which resulted in non-representative experiments.

Table 4.1 consists of two sections, an input and an output section. The input section presents the adjustable input parameters, such as the grain size, porosity and relative density *(RD)*. The output parameters are obtained by monitoring the development of the pipe during the experiments.

	Input				Output				
Experiment no.	**Sand type**	D_{50} (mm)	RD (-)	n (-)	ΔH_c (cm)	L_c (cm)	k (m/s)	$i_{c,global}$ (-)	$V_{c,avg}$ (m/s)
B25_217	Baskarp sand	0.22	0.802	0.376	6,40	14.00	3.00E-04	0,32	6,80E-05
B25_218	Baskarp sand	0.22	0.798	0.377	7,60	15.00	3.00E-04	0,4	7,37E-05
B25_219	Baskarp sand	0.22	0.806	0.376	7,80	8.50	3.00E-04	0,305882	1,53E-04
B25_220	Baskarp sand	0.22	0.803	0.376	6,60	14.50	3.00E-04	0,338462	7,10E-05
B25_221	Baskarp sand	0.22	0.792	0.378	6,50	18.50	3.00E-04	0,419355	9,20E-05
B25_222	Baskarp sand	0.22	0.807	0.376	6,90	9.00	3.00E-04	0,276	5,42E-05
B25_223	Baskarp sand	0.22	0.772	0.380	6,05	15.50	2.80E-04	0,327027	1,58E-04
B25_224	Baskarp sand	0.22	0.779	0.379	5,80	16.70	2.90E-04	0,33526	3,65E-05
B25_225	Baskarp sand	0.22	0.79	0.378	5,30	13.00	2.80E-04	0,252381	1,20E-04
B25_226	Baskarp sand	0.22	0.79	0.378	5,30	12.50	3.40E-04	0,246512	5,69E-05
B25_227	Baskarp sand	0.22	0.803	0.376	8,80	21.20	3.00E-04	0,6875	1,81E-04
B25_228	Baskarp sand	0.22	0.794	0.377	6,20	14.80	3.30E-04	0,322917	1,60E-04
B25_229	Baskarp sand	0.22	0.806	0.376	6,05	11.00	2.50E-04	0,263043	1,47E-04
B25_230	Baskarp sand	0.22	0.789	0.378	5,65	15.80	2.70E-04	0,31044	x
B25_231	Baskarp sand	0.22	0.797	0.377	5,60	13.50	3.00E-04	0,273171	1,11E-04
B25_232	Baskarp sand	0.22	0.796	0.377	6,60	14.6	2.70E-04	0,340206	1,02E-04
B25_233	Baskarp sand	0.22	0.545	0.405	6,30	11.7	3,50E-04	0,282511	1,68E-04
B25_234	Baskarp sand	0.22	0.545	0.406	5,40	16.40	3,70E-04	0,306818	9,46E-05
FPH_235	FPH sand	0.18	0.738	0.399	7,50	10.8	1,00E-04	0,323276	3,00E-05
B25_236	Baskarp sand	0.22	0.777	0.379	6,90	17.60	2,50E-04	0,420732	9,14E-05
FPH_237	FPH sand	0.18	0.791	0.392	7,50	18	8,00E-05	0,46875	6,35E-05
FS35_238	FS35 sand	0.42	0.671	0.381	6,7	17.9	1,00E-03	0,416149	3,21E-04
FS35_239	FS35 sand	0.42	0.768	0.370	6,60	12.9	9,00E-04	0,312796	8,53E-05
FS35_240	FS35 sand	0.42	0.490	0.399	6,40	20.30	1,15E-03	0,467153	1,39E-04
FS35_241	FS35 sand	0.42	0.492	0.399	6,35	17.6	1,10E-03	0,387195	1,44E-04
B25_243	Baskarp sand	0.22	0.792	0.378	6,3	15.8	2.50E-04	0,346154	5,17E-05
B25_244	Baskarp sand	0.22	0.558	0.404	12	24.8	3,50E-04	0,352941	x
B25_245	Baskarp sand	0.22	0.557	0.402	5,6	18.7	3,00E-04	0,366013	6,14E-05
FS35_246	FS35 sand	0.42	0.718	0.376	7,5	16.9	9,00E-04	0,438596	4,19E-04

Table 4.1: Overview of the performed experiments.

With:

d_{50} = 50%-fractile of grain size distribution (m)
RD = Relative density $((e_{max}-e)/(e_{max}-e_{min}))$ (-)
n = Porosity (volume of voids/total volume) (Vv/Vt) (-)
ΔH_c = Critical head difference (m)
L_c = Critical pipe length (cm)
k = Hydraulic conductivity (m/s)
$i_{c,global}$ = Global critical gradient $(\Delta H_c/(L-L_c))$ (-)
$v_{c,avg}$ = Averaged progression rate $((L-L_c)/(Tprogression))$ (m/s) (measured)

The output parameters are related to the progression phase of the pipe. In this phase, the pipe continuously grows until the pipe is fully developed (breakthrough).

The critical head difference and critical pipe length are measured from the moment of continuous development of the pipe. The averaged progression rate (m/s) is the total seepage length minus the critical seepage length divided by the progression time (dL/dt).

The hydraulic conductivity (k) of the soil sample is for each experiment determined by Darcy's law (Equation 4.1).

$$k = \frac{Q}{A\, i_{14,15}} \tag{4.1}$$

With:

k =	Hydraulic conductivity (m/s)
Q =	Discharge of water through the sample (m^3/s)
A =	Cross-section of the box (0.1 m * 0.3 m) (m^2)
$i_{14,15}$ =	Gradient between sensor 14 & 15 (end of the pipe) (-)

4.2.1 Graphical presentation of the results

For a more graphical presentation, different figures are presented to show the effects regarding the progression rate. The experiments are grouped by sand type and *RD* value. Different relations are expected between the progression rate, gradient, hydraulic conductivity and porosity.

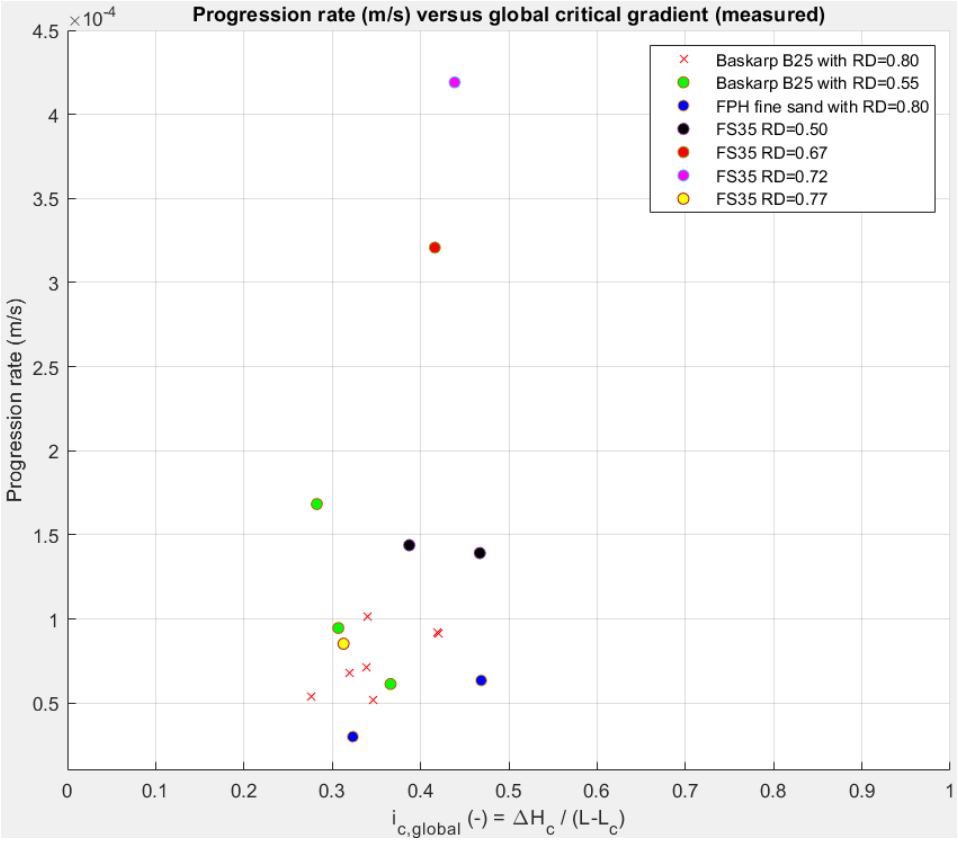

Figure 4.2: Progression rate versus global critical gradient.

Figure 4.2 shows that a larger gradient results in a larger progression rate (m/s) for the experiment group FPH fine sand (*RD*=0.8). A larger gradient *(H/L)* has a higher hydraulic head or a smaller seepage length. For the other two groups of sand Baskarp B25 (*RD=0.8*) and FS35, the same relation can be observed but the results are more scattered. Each datapoint represents one experiment.

The outlier in Figure 4.2 (red dot) presents experiment FS35_238. In this experiment, the head difference was increased too rapidly, which significantly influenced the critical pipe length and the progression rate. The second outlier (purple dot) presents experiment FS35_246 and was also subjected to a too rapid increase of the head difference.

Figure 4.3 presents the progression rate versus hydraulic conductivity. The hydraulic conductivity of the experiments with Baskarp B25 (*RD*=0.8) is plotted relatively close to each other. It can also be observed that the experiments with the coarser sand (FS35) have the highest hydraulic conductivity, and also the largest progression rate (m/s).

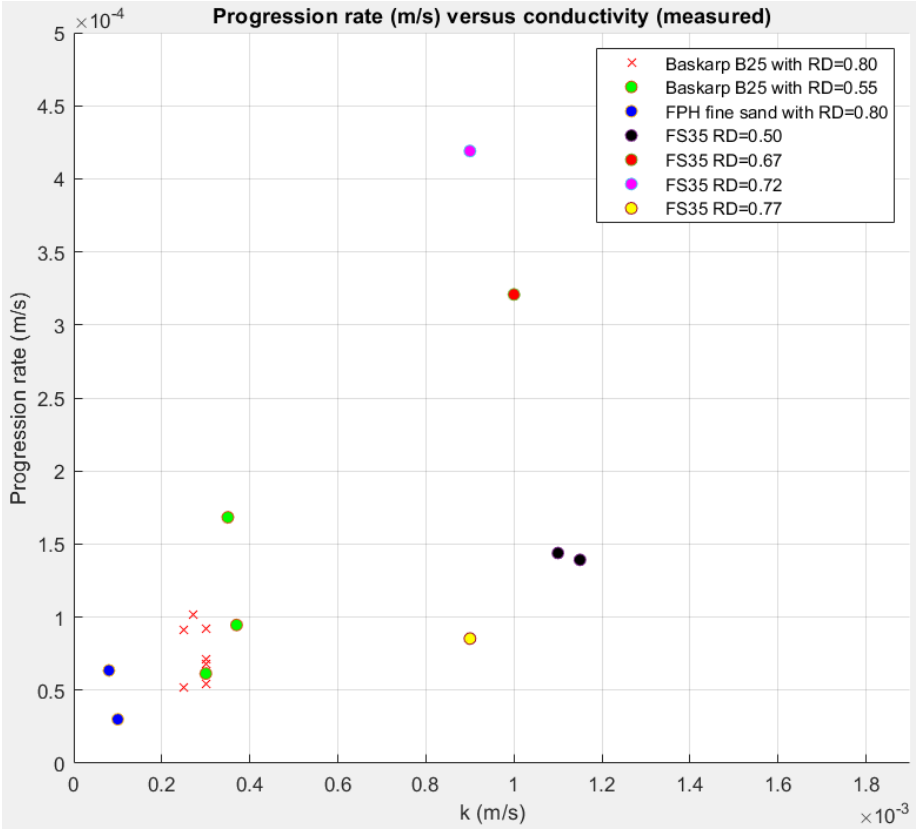

Figure 4.3: Progression rate versus hydraulic conductivity (k).

Figure 4.4 presents the critical hydraulic head versus the critical pipe length. Figure 4.4 shows a large range of values for the critical pipe length (between 8-20 cm). The critical pipe length is the length of the pipe where the pipe continuously grows until the breakthrough. Sellmeijer predicted that the critical pipe length is approximately 50% of the total seepage length. For the average critical pipe length (15/34 cm) a percentage is obtained of 44% which is in line with Sellmeijer's figure (Figure 2.11).

Another observation can be made about the FPH experiments (finer sand). Both FPH experiments have the same critical head difference. It shows that a finer sand type requires a larger critical head for the pipe to develop than a coarser sand type (Baskarp B25).

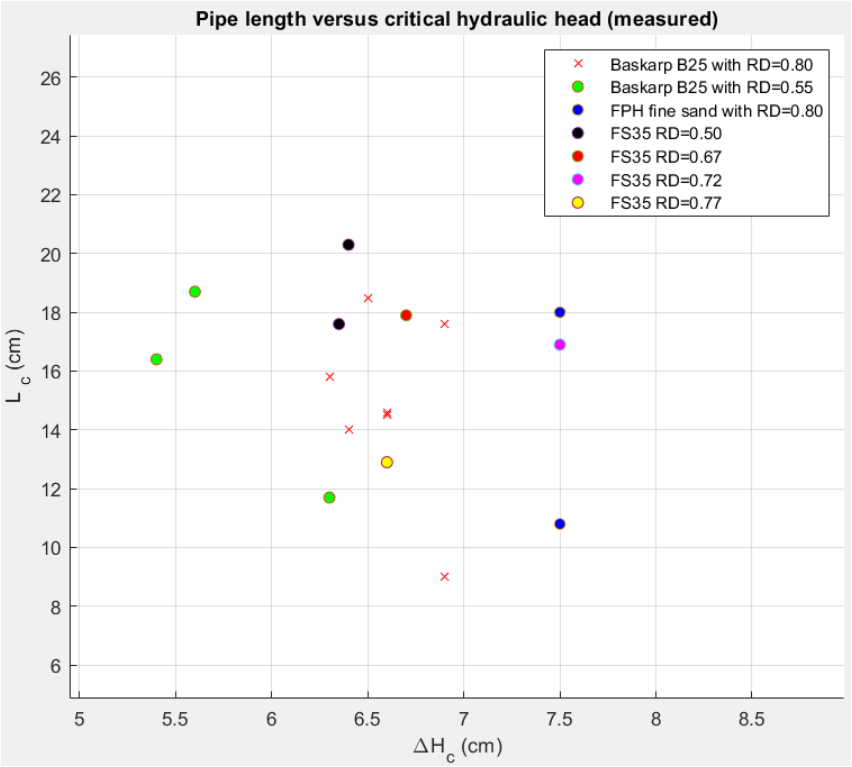

Figure 4.4: Critical pipe length versus critical hydraulic head.

Figure 4.5 presents the porosity related to the progression rate. The experiments with sand type Baskarp B25 have a minimum of scattering. Figure 4.5 also shows that there is no relation between the porosity and the progression rate. The datapoints are too scattered to observe a clear relation.

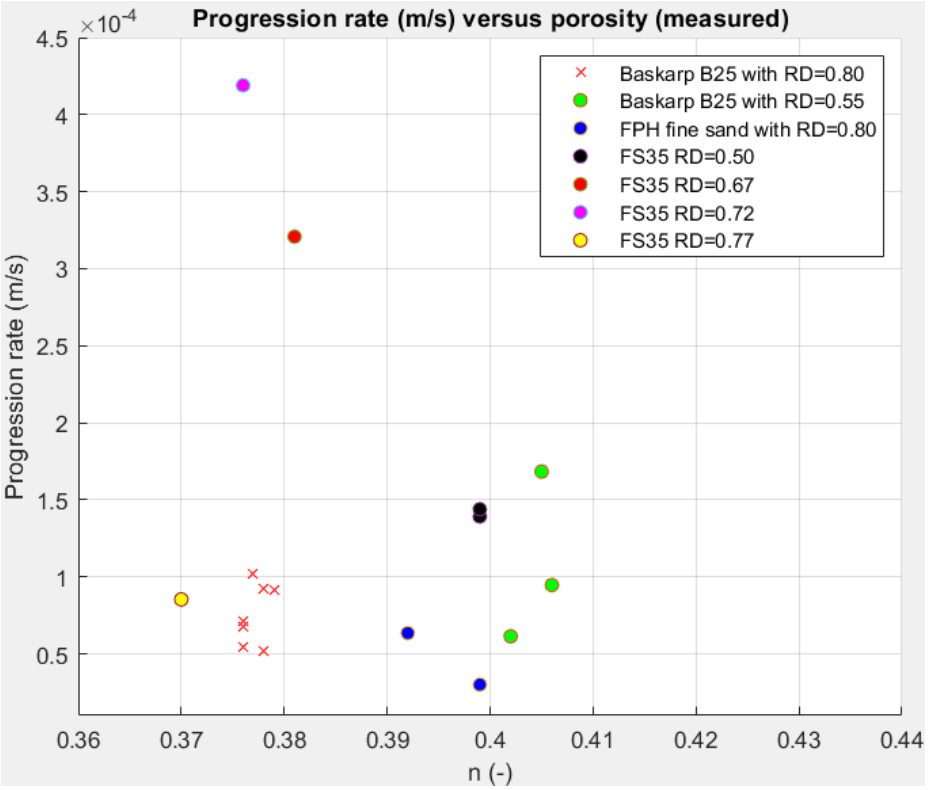

Figure 4.5: Progression rate versus porosity (n).

Figure 4.6 presents the progression rate versus the specific discharge. The specific discharge for the experiments with Baskarp B25 is almost equal to the progression rate (ratio 1:1), but for the coarser sand experiments (FS35) it is approximately 3 times larger. The specific discharge is derived from Darcy's law and presents the Darcy velocity.

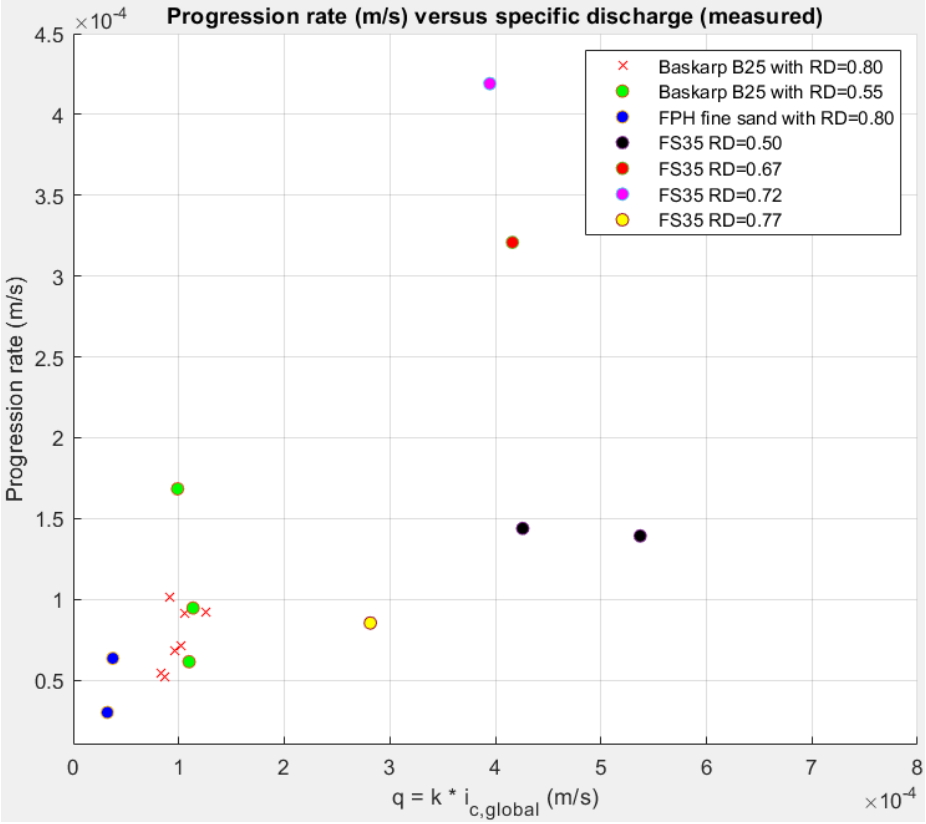

Figure 4.6: Progression rate versus specific discharge.

From the five figures presented, it can be observed that the hydraulic conductivity plays an important role in the progression rate. This in combination with the particle diameter. The finer sand experiments have a higher critical head difference, due to a lower hydraulic conductivity.

Figure 4.3 and Figure 4.5 indicate that the Baskarp B25 experiments have very little scatter. The experiments with the same characteristics are plotted relatively close to each other. The two experiments with sand type FS35 (*RD*=0.5) give almost identical results.

4.2.2 Calculation of the critical head (Sellmeijer)

Table 4.2 presents the results of the measured and calculated (Sellmeijer) critical head values. The measured critical head values are compared with the calculated values from the model of Sellmeijer. The table shows that all the measured results are lower than the predicted critical head value of Sellmeijer, approximately by a factor two.

In the small and medium-scale experiments of Van Beek (Van Beek, 2015) the same observation was made with a factor two between the measured results and the calculated values. Sellmeijer's model predicts the critical head difference for a 2D situation very well, but for a 3D configuration, Sellmeijer's model over-predicts the critical head difference.

Sand type	ΔH_c Sellmeijer (cm) (calculated)	ΔH_c measured (cm)	k (m/s)	d_{50} (mm)
Baskarp B25 *RD*=0.80	13.8	6.6	2.82E-04	0.22
Baskarp B25 *RD*=0.55	11.4	5.76	3.40E-04	0.22
FPH *RD*=0.74	16.6	7.5	1.00E-04	0.18
FPH *RD*=0.79	18.3	7.5	8.00E-05	0.18
FS35 *RD*=0.49	8.8	6.38	1,13E-03	0.42
FS35 *RD*=0.67	10.3	6.7	1,00E-03	0.42
FS35 *RD*=0.72	10.9	7.5	9,00E-04	0.42
FS35 *RD*=0.77	11.2	6.6	9.00E-04	0.42

Table 4.2: Overview of the different critical head values.

The critical head according to Sellmeijer's model is calculated with equations 2.4 to 2.7 and can be found in Appendix D.

$$\Delta H_{c,Sellmeijer} \approx 2 * \Delta H_{c,measured} \quad (4.2)$$

With:

$\Delta H_{c,Sellmeijer}$ = Critical head difference (m) calculated by model of Sellmeijer
$\Delta H_{c,measured}$ = Measured critical head difference (m)

4.2.3 Mass of the sand boil

The sand boils are measured after each experiment and are a function of time and mass. This includes the mass, inner and outer slope, the edge of the radius and the boil porosity. The measurements are used to calculate and predict the sediment transport rate for each experiment. A prediction of the sediment transport rate over time is presented in section 4.3.1.

Table E.1 (Appendix E) contains the measured mass (g) and predicted mass (g). To predict the mass of the sand boil, an equation is designed based on the volume of a cone. The predicted mass (g) calculation is based on averaged values of all experiments for the outer slope, inner slope and porosity. This results in a lower value for the predicted mass (g) than the weighted mass (g). Figure 4.7 presents a schematic cross-section of the sand boil.

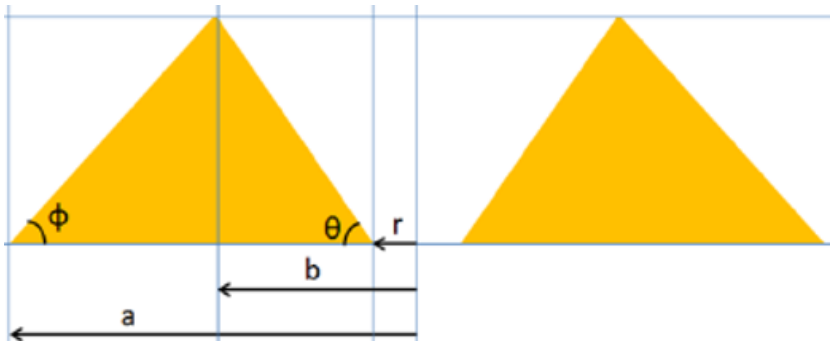

Figure 4.7: Schematic cross-section of the sand boil (Vandenboer, 2018).

4.3 Analysis of experiment FPH-235

The former section presents the results on a global scale. In this section, the results of experiment FPH-235 are presented and further analysed. This contains the progression and sediment transport rate of the pipe.

4.3.1 Sediment transport rate of Experiment FPH 235

In all experiments, the outer radius is monitored in timesteps of two and three minutes. Once the pipe enters the progression phase the outer radius is measured every minute. By measuring the radius of the sand boil, the increase in volume is monitored over time. This can be used to calculate the sediment transport rate of the pipe.

Appendix F presents the observation sheet of experiment FPH-235 and column D (cm) describes the outer radius of the sand boil. The ending radius for experiment FPH-235 is 2.1 cm. Figure 4.8 presents the top view of the sand boil.

Figure 4.8: Top view of the sand boil (Outer radius = 2.1 cm).

With applying the equations in Appendix E, the mass of the crater can be calculated during the experiment. Figure 4.9 presents the development of the crater mass over time. After differentiating (dy/dx) the line, the sediment transport rate is obtained. The red line in Figure 4.9 resents the gradient in the sediment transport rate for each datapoint. The values of the red line fluctuate from zero to peak values of 0.74 g/min.

The averaged sediment transport rate at the beginning of the experiment (from 0 - 120 min) is 0.0185 g/min. The averaged sediment transport rate during the progression phase (from 120 - 246 min.) is 0.037 g/min. It can be observed that during the progression phase the slope is steeper and more sediment is transported than at the beginning of the experiment.

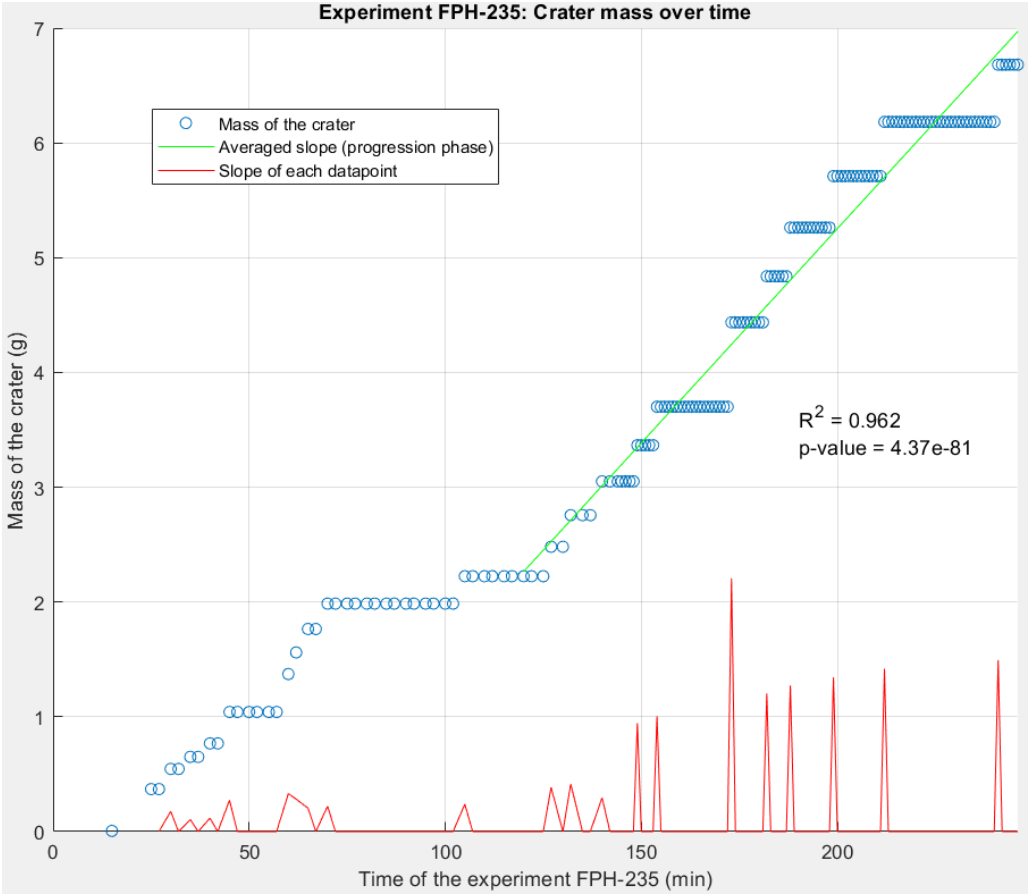

Figure 4.9: Development of the crater over time (Experiment FPH-235).

4.3.2 Primary erosion experiment FPH-235

The total sediment transport rate is a combination of primary and secondary erosion (section 2.4). By measuring the mass over time (crater radius), the total sediment transport rate is known. When the primary erosion rate is distracted by the total transport rate, the secondary erosion rate is obtained.

The primary erosion rate can be determined with equation 4.3, using the average depth and width at the tip of the pipe to calculate a weight per unit of time. Equation 4.3 couples the progression rate (pipe increases in length in longitudinal-direction) to a primary erosion rate (g/min).

Table 4.3 presents the results of the calculation.

$$q_{v,primary} = v_{c,avg}\,(1-n)\,d_{pipe,tip}\,w\,\rho_s\,1000\,60 \qquad (4.3)$$

With:

$q_{v,\ primary}$ =	Sediment transport rate (primary) (g/min)
$v_{c,avg}$ =	Averaged progression rate *((L-Lc)/(Tprogression))* (m/s)
n =	Porosity (volume of voids/total volume) *(Vv/Vt)* (-)
$d_{pipe,tip}$ =	Depth at the tip of the pipe (m)
w =	Width at the tip of the pipe (m)
ρ_s =	Particle density (kg/m^3)

Parameter	Symbol	Value
Progression rate FPH-235 (m/s)	$v_{c,avg}$	3.00E-05
Porosity FPH-235	n	0.399
Depth at the tip of the pipe (m)	$d_{pipe,tip}$	0.00021
Width at the tip of the pipe (m)	w	0.01
Density of the grains (kg/m^3)	ρ_s	2610
Sediment transport rate (primary) (g/min)	$q_{v,\ primary}$	0.0059

Table 4.3: Results of the $q_{v,\ primary}$ calculation.

The secondary sediment transport rate can be calculated with equations 4.4 and 4.5.

$$q_{v,total} = q_{v,primary} + q_{v,secondary} \quad (4.4)$$

$$q_{v,secondary} = q_{v,total} - q_{v,primary} \quad (4.5)$$

$$q_{v,secondary} = 0.037 - 0.0059 = 0.0311 \text{ g/min} \quad (4.5)$$

With:

$q_{v,\ total}$ = Sediment transport rate (total) (g/min) (Figure 4.9)
$q_{v,\ primary}$ = Sediment transport rate (primary) (g/min) (Equation 4.3)
$q_{v,\ secondary}$ = Sediment transport rate (secondary) (g/min)

Equation 4.4 indicates that the total erosion rate *($q_{v,\ total}$)* consists of 16% of primary erosion and 84% secondary erosion.
The primary erosion rate is obtained by the measured progression rate of experiment FPH-235. The dimensions of the tip of the pipe (front of the pipe) are obtained from Figure G.2.3 (Appendix G2).

Due to a constant pipe depth of 0.21 mm at the tip of the pipe, the primary erosion rate is relatively low compared to the secondary erosion rate. This is because a measured constant depth is used (0.21 mm) for the whole length of the pipe. The figure in Appendix G2 presents that the deepest point of the pipe is 0.8 mm closest to the sand boil. This point is deeper than the tip of the pipe because all the sand particles have to be transported through this point to enter the soil boil. When the pipe grows in length the depth at the tip remains constant, but the rest of the pipe is further deepened.
Figure G.2.3 shows that the deepest part of the pipe (d_{avg}) is at the beginning of the pipe (x=20-25) next to the exit (sand boil). The data in Figure G.2.3 (Appendix G) is measured after the breakthrough of the pipe. The deepest point is next to the exit, and the tip of the pipe (front of the pipe) is located at x=45 cm (sensor P15, Figure 3.10).

4.3.3 Results of the bed shear stress of experiment FPH-235

According to the equations mentioned in chapter two, numerous data were obtained during the experiments regarding the bed shear stress. To summarize the results of the last sections (FPH-235), the shear stress is calculated at several locations in the pipe for the equilibrium situation. The shear stress and the shields parameters are calculated with the equations below.

$$\tau_c = \rho_w \, g \, R \, S_1 \tag{4.6}$$

$$\Psi c = \frac{\tau_c}{(\rho_s - \rho_w) \, g \, d} = \frac{\rho_w \, g \, R \, S_1}{(\rho_s - \rho_w) \, g \, d} = \frac{R \, S_1}{\Delta \, \mathrm{d}} \tag{4.7}$$

With:

τ_c =	Critical shear stress (N/m^2)
Ψ_c =	Critical Shields parameter (-)
ρ_s =	Particle density (kg/m^3)
ρ_w =	Density of water (kg/m^3)
g =	Acceleration of gravity (m/s^2)
d =	Particle diameter (m)
Δ =	Relative density $(=(\rho_s - \rho_w)/\rho_w)$ (-)
R =	Hydraulic radius (area/perimeter) (m)
S_1 =	Local slope after breakthrough of the pipe (dh/dx) (-)

The Shields parameters are calculated for experiment FPH-235 after the breakthrough of the pipe. After the breakthrough of the pipe, the head was lowered to seek for the equilibrium head difference (no transport of particles). From this moment the gradients (Figure G.1.1) and the dimensions of the pipe were obtained (Appendix G1). After substituting the gradients in equation 4.7, the Shields parameters could be determined. Table G.1.1 shows that the Shields parameters vary from 0.03 to 0.33. This range of values is relatively large due to the differences in the hydraulic radius of the pipe along its length. Since the nominal discharge of water is constant, according to Darcy's law if the gradient is large in one section, the area of the section (i.e. the hydraulic radius) should be smaller. Figure 4.10 presents the measured gradient versus the hydraulic radius.

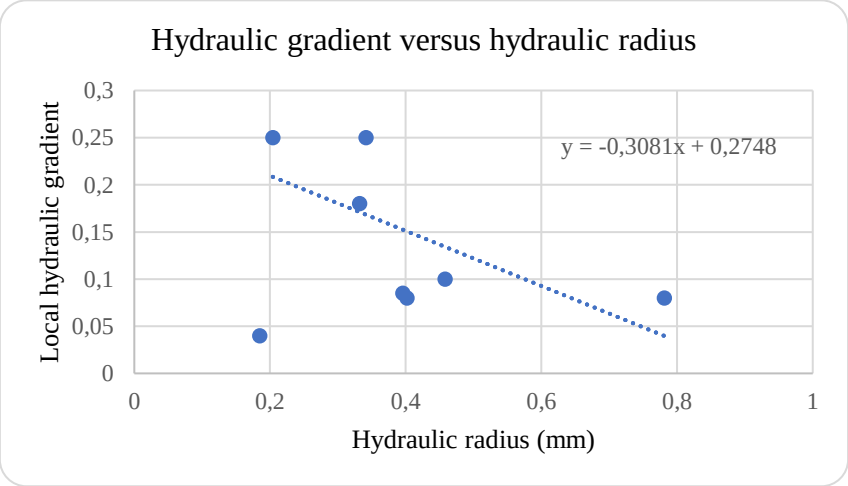

Figure 4.10: Local hydraulic gradient versus the hydraulic radius of experiment FPH-235.

From the 11 cross-sections of the pipe, only three points could be plotted on the Shields diagram. This was due to the fact that the pipe did not develop below every pressure sensor. The pipe in developed below six different sensors (P3, P4, P5, P8, P9, P10 and combined with the corresponding cross-section of the pipe three points could be plotted. The results of equation 4.7 are plotted in Figure 4.11.

The range of values can be explained by the range of the hydraulic radius. The first point is measured between P3 and P4 and has almost the deepest point of the pipe. The other two points are obtained halfway of the pipe at P8 and P10. The difference in depth plays a large role in the hydraulic radius (R). A larger depth equals a larger bed shear stress and a larger Shields parameter (highest point in the graph).

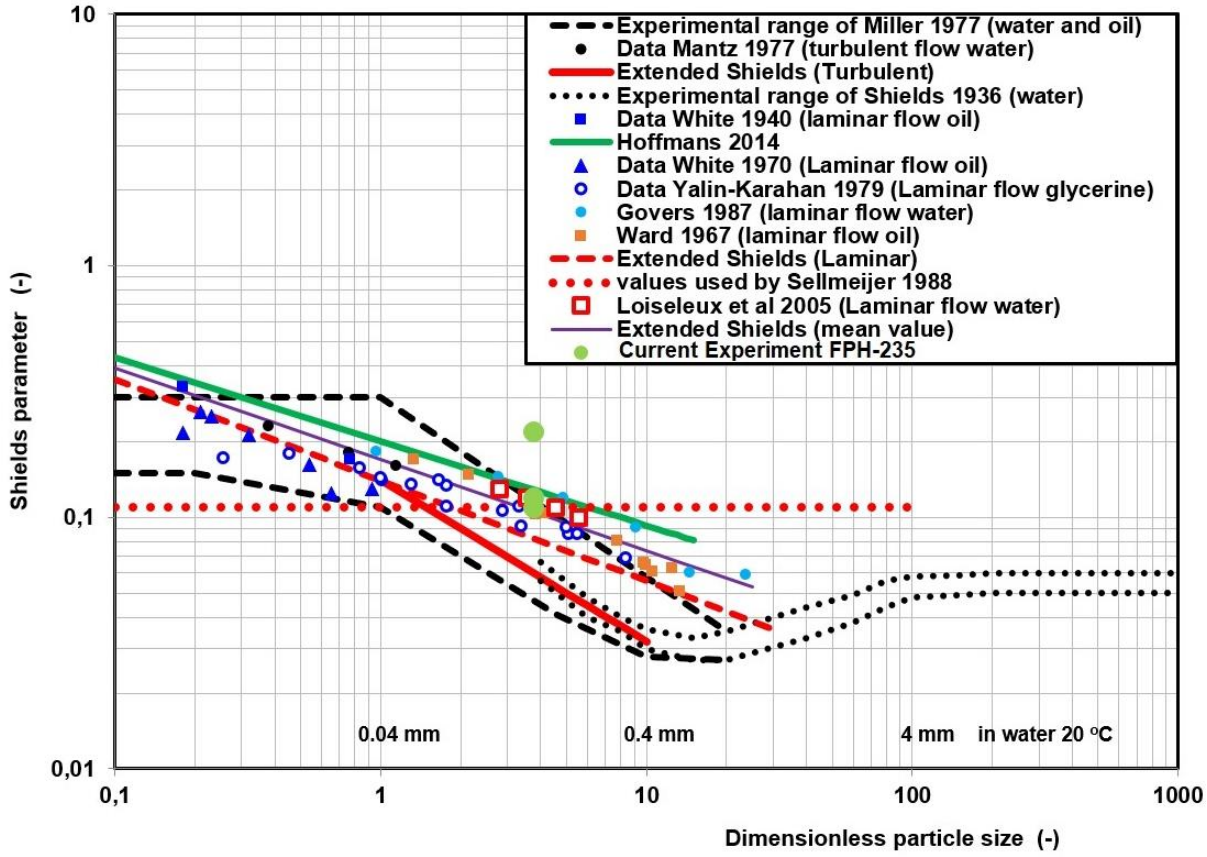

Figure 4.11: Shields diagram including experimental results FPH-235.

The average of the plotted Shields parameters of FPH-235 crosses the horizontal line of Sellmeijer (1988). Sellmeijer applied with equation 4.8 the concept of incipient motion in backward erosion piping. The combination of the approach of White and the critical Shields parameter is often used for the assessment of incipient motion (Van Beek et al., 2019).

(Sellmeijer)

$$\Psi c = \frac{\eta \frac{\pi}{6} \gamma'_p \, d \, tan\,(\theta)}{(\rho_s - \rho_w)\, g \, d} = \eta \frac{\pi}{6} tan\,(\theta) \qquad (4.8)$$

With:

η =	Constant of white (-)
γ'_p =	Submerged volumetric weight sand (kN/m^3)
d =	Particle diameter (m)
θ =	Bedding angle (°)
ρ_s =	Particle density (kg/m^3)
ρ_w =	Density of water (kg/m^3)
g =	Acceleration of gravity (m/s^2)

4.3.4 Sediment transport rate experiment FPH-235 (Cheng, 2004)

Equation 2.24 presents the adapted equation for the bedload sediment transport rate (m^2/s). The original equation (Equation 2.20) is derived by Cheng (Cheng, 2004). In the adapted equation is the shear velocity is expressed as a function of the bed shear stress and substituted. The averaged transport rate is calculated using the particle diameter (FPH sand), the hydraulic radius and the local gradient. Appendix G2 presents the different gradients of the pressure sensors. From the sediment transport rate, the mass and progression rate can be determined.

$$m = q_{v,C,adapted}\ \rho_s\ w\ T_{prog} \tag{4.9}$$

$$v_{progression} = \frac{q_{v,C,adapted}}{(d_{pipe} * (1-n))} \tag{4.10}$$

$$q_{v,measured} = v_{c,avg}\ (d_{pipe,tip} * (1-n)) \tag{4.11}$$

(Calculated)

$$\Phi_{calculated} = \frac{q_{v,C,adapted}}{d\sqrt{\Delta g d}} \tag{4.12}$$

(Measured)

$$\Phi_{measured} = \frac{q_{v,measured}}{d\sqrt{\Delta g d}} \tag{4.13}$$

With:

$q_{v,C,adapted}$ =	Adapted volumetric sediment transport rate per unit width (Equation 2.24) (m^2/s)
$q_{v,measured}$ =	Measured volumetric sediment transport rate per unit width (m^2/s)
d =	Particle diameter (m)
R =	Hydraulic radius (area/perimeter) (m)
S =	Local slope of the pipe (dh/dx) (i_pipe) (-)
Δ =	Relative density *(=(ρ_s- ρ_w)/ρ_w)* (-)
g =	Acceleration of gravity (m/s^2)
w =	Width at the tip of the pipe (m)
ρ_s =	Particle density (kg/m^3)
m =	Mass of the sand crater (g)
$T_{progression}$ =	Time of the progression phase (min)
$v_{progression}$ =	Progression rate velocity (m/s) (Cheng)
$v_{c,avg}$ =	Averaged progression rate *((L-L$_c$)/(Tprogression))* (m/s) (measured in FPH-235)
$d_{pipe,tip}$ =	Depth at the tip of the pipe (m)
n =	Porosity (volume of voids/total volume) *(Vv/Vt)* (-)
$\Phi_{calculated}$ =	Calculated bedload transport rate (Cheng adapted formula) (-)
$\Phi_{measured}$ =	Bedload transport rate from measured progression rate (FPH-235) (-)

Table 4.4 presents the results of the sediment and progression rate calculation using the equations above. A progression rate is obtained of 5.4E-04 m/s applying the mean values. The adapted formulation of Cheng (Equation 2.24) predicts a very large value for the progression rate than the measured value of 3.00E-05 m/s. Approximately by a factor 18.

Parameter	Symbol	Lower bound value	Value	Upper bound value	Explanation
Particle diameter FPH sand (m)	d	0.000177	0.00018	0.000183	Significance of 0.003 mm from sieve test (Appendix B2)
Relative density $(\rho_s-\rho_w)/(\rho_w)$ (-)	Δ	1.59	1.61	1.63	Combination of ranges parameters ρ_s and ρ_w
Acceleration of gravity (m/s^2)	g	9.81	9.81	9.81	-
Local averaged slope (dh/dx) of the pipe (-)	S	0.125	0.165	0.192	Gradients vary approximately 0.05 from the mean (Figure G.2.1)
Hydraulic radius (m)	R	0.00016	0.0002	0.00023	Measurement deviation cross-section of the pipe (Figure G.2.4 & G.2.5)
Width at the tip of the pipe (m)	w	0.008	0.01	0.012	Measurement deviation of 0.2 mm
Particle density (kg/m^3)	ρ_s	2560	2610	2660	Deviation of 50 kg/m^3 (Schiereck, 2012)
Density of water (kg/m^3)	ρ_w	990	1000	1010	Deviation of 10 kg/m^3 (Schiereck, 2012)
Averaged depth at the tip of the pipe (m)	$d_{pipe,tip}$	0.000166	0.00021	0.000235	Measurement deviation cross-section of the pipe (Figure G.2.4 & G.2.5)
Progression time (min)	$T_{progression}$	125	126	127	Measurement deviation of 1 minute
Porosity FPH-235 (volume of voids/total volume) (Vv/Vt)	n	0.398	0.399	0.40	Significance in porosity of 0.001
Shields parameter (-) (Equation 2.18)	Ψ	0.071	0.114	0.148	-
Calculated bedload transport rate (-)	$\Phi_{calculated}$	0.001	0.0071	0.021	-
Measured bedload transport rate from progression rate (FPH-235) (-)	$\Phi_{measured}$	0.00032	0.0004	0.00043	-
Measured volumetric sediment transport rate per unit width (m^2/s)	$q_{v,measured}$	2.998E-09	3.786E-09	4.230E-09	-
Adapted volumetric sediment transport rate per unit width (m^2/s)	$q_{v,C,adapted}$	9.5816E-09	6.8162E-08	2.0980E-07	-
Mass of the sand crater (g)	m	1.47	13.44	51.05	-
Progression rate velocity (m/s) (Cheng)	$v_{progression}$	9.59E-05	5.40E-04	1.5E-03	-

Table 4.4: Calculation of the sediment transport and progression rate (Equation 2.24, 4.9 to 4.13).

The lower and upper bound values show that the equations are very sensitive to the value of the input parameters. A larger particle diameter, lower relative density, a larger hydraulic radius and a larger gradient increases the sediment transport rate. The progression velocity is influenced by the depth of the pipe, the time of the progression phase and the porosity. The lower the depth of the pipe the higher the progression velocity and the longer the time of the progression phase, the more sediment is transported (Equation 4.10). Table 4.4 shows as well that a higher porosity increases the progression velocity.

The gradients measured inside the pipe have a range of approximately 0.05 for the lower and upper bound. This is due to the fluctuating of the measurements of the pressure sensors. The sensors are rather sensitive and vary constantly in time. Table 4.4 showed that the gradients (S) have a large influence on the results and the transported mass (Equation 2.24 and 4.9).

Gradient	Lower bound i_pipe	i_pipe (*S*)	Upper bound i_pipe
i_3,4	0.10	0.164166	0.20
i_4,5	0.05	0.076197	0.10
i_5,6	0.20	0.215912	0.25
i_8,9	0.10	0.13	0.15
i_9,10	0.10	0.131824	0.15
i_10,11	0.20	0.272833	0.30
	0.125	**0.165**	**0.192**

Table 4.5: Range of local pipe gradients (Experiment FPH-235 after passing of the pipe).

The bedload transport rate is calculated by equation 4.12 and 4.13. The calculated value is compared to the measured value from experiment FPH-235 and plotted in Figure 4.12. It shows that the calculated value is larger than the measured value, and therefore does not match the linear line. The calculated transport rate overpredicts the measured transport rate.

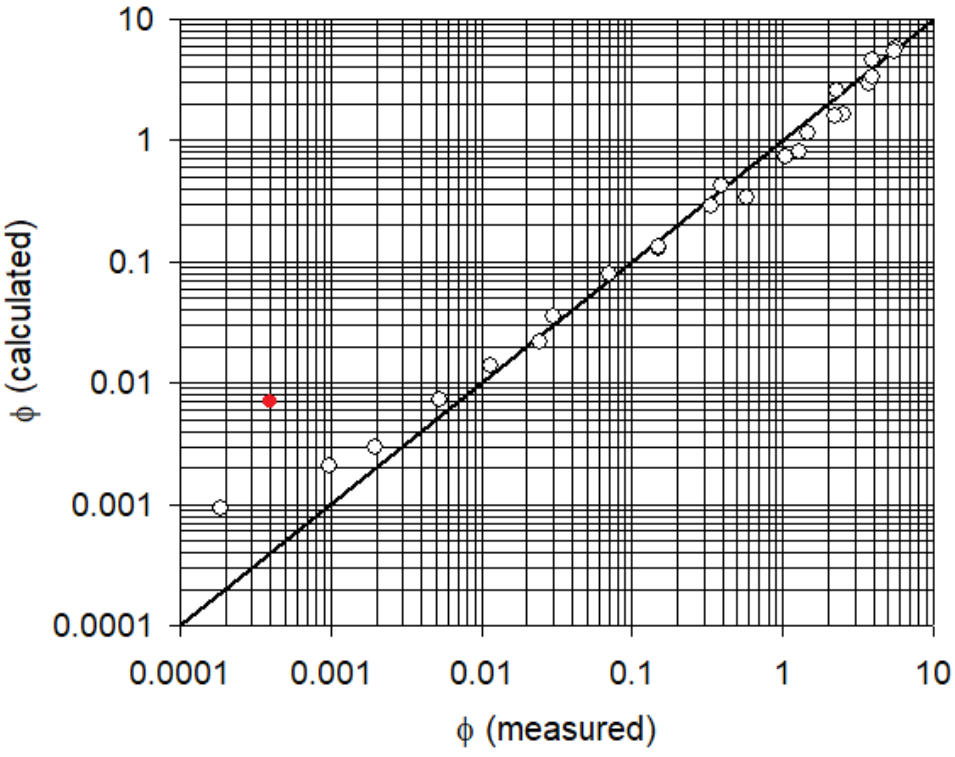

Figure 4.12: Calculated and measured dimensionless transport rate of experiment FPH-235 (Cheng, 2004).

4.3.5 Dilatancy results (Experiment FPH-235)

The wall velocity (m/s) is calculated by equation 2.14. The corresponding gradients for the different pressure sensors determine the wall velocity. In experiment FPH-235 the pipe developed below six pressure sensors (P3, P4, P5, P8, P9, P10), where six different gradients were measured (i_pipe and i_tip) during the experiment (Figure 4.13). When the pipe develops below a pressure sensor, the pressure inside the pipe can be directly measured. Table G.2.1 in Appendix G2 presents the gradients for experiment FPH-235.

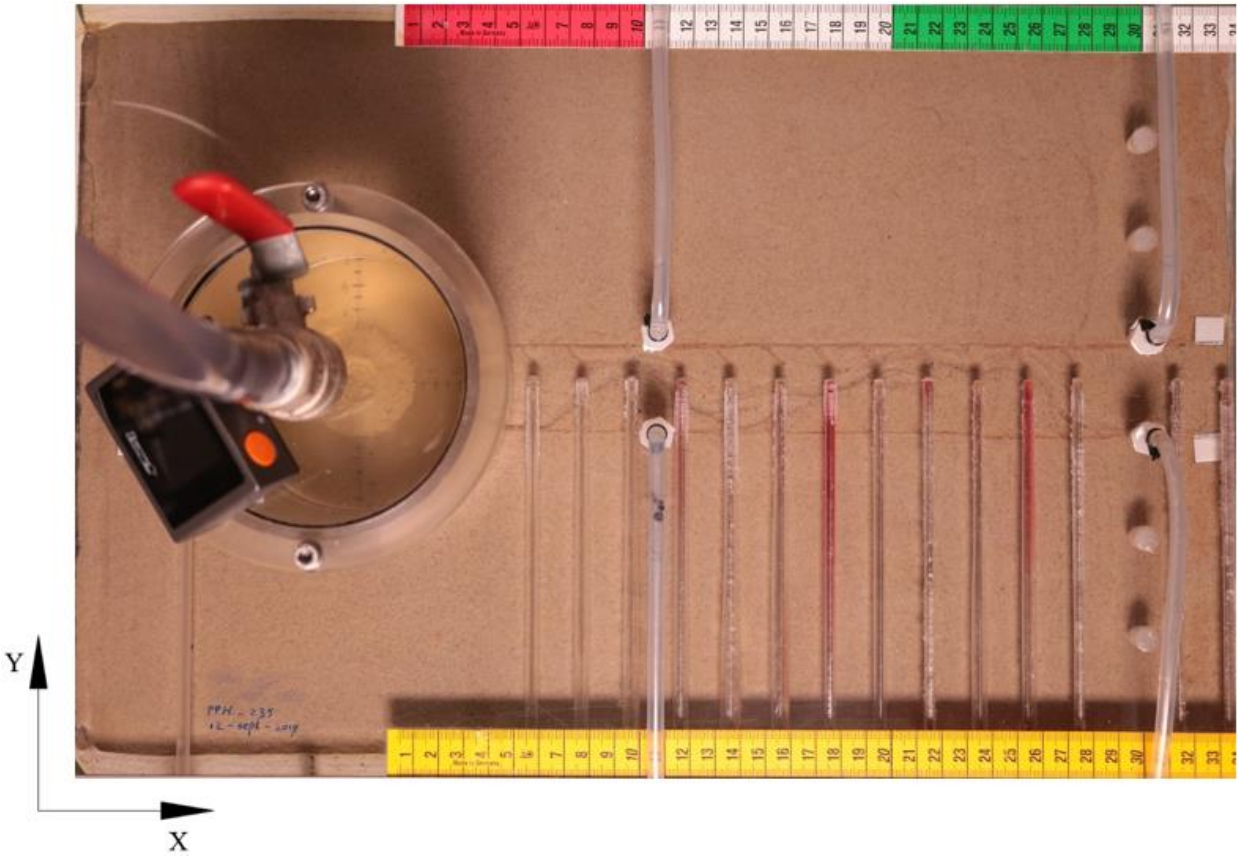

Figure 4.13: Top view of the pipe development (Experiment FPH-235).

The peak gradient (i_tip) shows a peak in the graph (Figure G.2.1). This peak is measured when the pipe arrives at the pressure sensor. When the pipe continues to the next sensor, the gradient drops. This gradient is called the local pipe gradient (i_pipe). For the calculation of the wall velocity, the local peak gradient (i_tip) is used.

Table 4.6 presents the measured gradients (dh/dx) from the six pressure sensors (P3, P4, P5, P8, P9, P10).

Transducer	Gradient	i_tip	t_i_tip (s)	t_i_tip (min)
P3	i_3,4	0.7334	5140.058	86
P4	i_4,5	0.6972	7021.045	117
P5	i_5,6	0.5665	7608.853	127
P8	i_8,9	0.6001	9751.089	163
P9	i_9,10	0.5807	10547.9	176
P10	i_10,11	0.6558	11318.58	189

Table 4.6: Gradients of the six pressure sensors of experiment FPH-235.

Table 4.7 presents the parameters for the wall velocity of experiment FPH-235. The maximum porosity is determined according to the method described in Appendix G.2.2 (Van der Linden, 2016).

Parameter	Symbol	Value
Local peak gradient (dh/dx) (i_tip) (-)	i_{loc}	0.56 - 0.73
Initial Porosity (-)	n_0	0.399
Maximum porosity (-)	n_{max}	0.485
Hydraulic conductivity (m/s)	k	1.0E-04
Averaged wall velocity of 6 sensors (cm/min)	$v_{wal,avg}$	2.30
Averaged measured progression rate (FPH-235) (cm/min)	$v_{c,avg}$	0.18

Table 4.7: Parameters for the dilatancy calculation (FPH-235).

Figure 4.14 presents the velocity along with the development of the pipe from sensor 3 till 10. The average wall velocity is 2.3 cm/min. The gradient at P3 was measured 86 minutes from the start of the experiment. From there the pipe developed further and arrived at sensor P10 just after 189 minutes. The head difference at P3 was one centimetre below the critical point. When the pipe developed below P4, the head difference was critical.

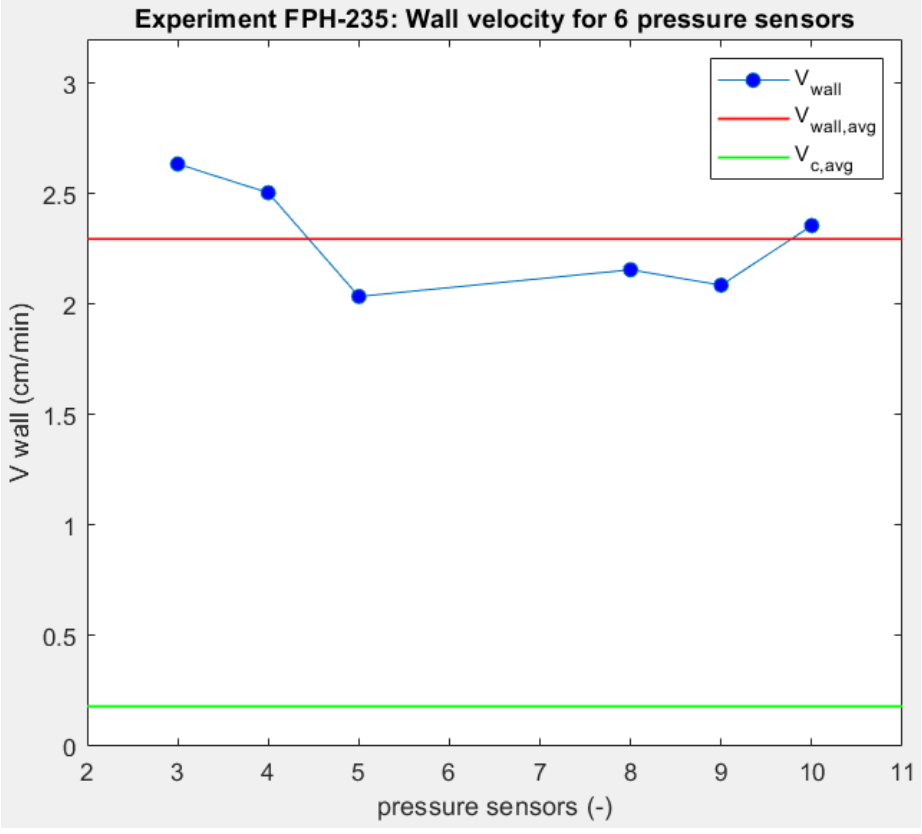

Figure 4.14: Wall velocity for the six pressure sensors (experiment FPH-235).

Before the pipe starts to develop in length, the porosity needs to increase to a critical value for the particle to be transported. The wall velocity ranges from ≈ 2.0 cm/min till 2.64 cm/min. Compared to the measured progression rate of experiment FPH-235 (0.18 cm/min), the averaged wall velocity is approximately 12 times larger.

Equation 2.14 describes the velocity of which a wall of sand, shifts towards the direction of the flow (De Groot et al., 2009). Also described as backward erosion of the wall. Before the wall is shifted, many sand particles whirl down and slide along the wall (white arrows, Figure 4.15). After a certain moment, the angle of the slope changes and fails. The wall shifts towards the east and from this moment the cycle can be repeated.

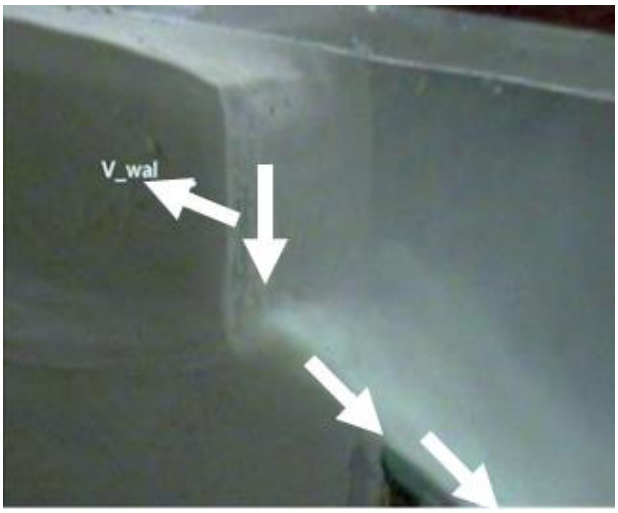

Figure 4.15: Schematization of the wall velocity for fine sand (De Groot et al., 2009).

Another observation is the range of the values in Figure 4.14. At the start of the pipe (P3, P4), the wall velocities are larger than the mean. When the pipe further develops and reaches P8 and P9, the peak gradients drop and result in a lower wall velocity. When the pipe continuously grows (progression phase) the velocities are lower. This results in that there is less shear stress required to change to volume of the pores.

4.4 Comparison of the results with the hypothesis

The hypothesis in section 2.4.1 presents a table with the expected effect of different parameters regarding the progression rate. In this section, the obtained results from the experiments are compared to the predictions and interpreted. The objective is to discover the differences and similarities in the experimental series.

Figure 4.2 to Figure 4.6 present an overview of the measured data of the selected experiments. Figure 4.3 shows that the FPH experiments have a lower progression rate than the experiments with Baskarp B25. Overall, the experiments with a larger particle diameter have a higher progression rate.

Table 4.8 presents the effects of the different parameters for each type of sand. For example, the finer sand experiments (FPH-sand) show for a larger gradient (Figure 4.2), a larger progression rate. A positive sign is given to the parameters which enhance the progression rate. A negative sign is given to the parameters which reduce the progression rate. The positive /negative sign is given to the parameters which are balancing between an increase and decrease of the progression rate.

In total, two FPH-sand experiments were performed which have the same hydraulic conductivity and relative density value. Therefore, the results could not be compared, and an X sign was placed in the table. The parameters relative density and porosity show no clear relation from the measured datapoints (Figure 4.3).

	FPH-sand finest type (d_{50}=0.18 mm)	**Baskarp B25-sand medium type (d_{50}=0.22 mm)**	**FS35-sand coarsest type (d_{50}=0.42 mm)**
Parameters	**Effect on the progression rate**	**Effect on the progression rate**	**Effect on the progression rate**
Gradient *(ΔH/L)* ↑*	+	+	+
Hydraulic conductivity *(k)*↑	-	+/-	+
Relative density *(RD)* ↑	x	No clear relation from datapoints	No clear relation from datapoints
Porosity/void ratio *(e)* ↑	-	No clear relation from datapoints	No clear relation from datapoints

↑* (Increase of parameters)

Table 4.8: Observed relations from measured results (for three types of sand).

Table 4.9 compares the hypothesis with the measured results regarding the progression rate. In this table, a comparison is made for all experiments. For example, an increase in particle diameter shows a higher progression rate, this equals a positive sign.

	Hypothesis prediction	**Measured results**	**Match the hypothesis?**
Parameters	**Effect on the progression rate**	**Effect on the progression rate**	
Particle diameter *(d)* ↑*	+/-	+	Partly
Gradient *(ΔH/L)* ↑	+	+	Yes
Relative density *(RD)* ↑	-	x	No clear relation from datapoints
Hydraulic conductivity *(k)*↑	+	+	Yes
Porosity/void ratio *(e)* ↑	+	x	No clear relation from datapoints

↑* (Increase of parameters)

Table 4.9: Comparison of the hypothesis and measured results (all experiments).

Figure 4.4 shows that the finest sand (FPH sand), requires the largest critical head difference (ΔH_c) for the pipe to develop. The experiments with FPH sand also have a very low hydraulic conductivity, in the range of 1E-04 m/s. For the experiments with rather fine sand (d_{50}=0.18 mm), it is difficult for the flow to go through the sample. Therefore, a larger head difference must be applied for the pipe to develop. The highest value for the ΔH_c belongs to the experiments with the smallest particle diameter and lowest progression rate. This shows that the experiments with a smaller particle diameter (FPH-235, FPH-237), require a larger hydraulic head difference.

Table 4.9 also indicates that the hypothesis is well supported for the coarser sand experiments, although the results of the progression rate are rather interesting. Figure 4.2 shows that the coarser sand experiments have the highest progression rate. This was not expected, because coarser sand particles are heavier due to a larger particle diameter (d_{50}=0.42 mm). Lighter particles are easier transported than heavier particles, due to a lower downforce by gravity. However, the FS35 experiments have the largest hydraulic permeability (Figure 4.3) which compensated this effect.

The experiments with Baskarp B25 (*RD=0.8*) show that a larger gradient results in a higher progression rate. This observation is presented in Figure 4.16. The Baskarp B25 experiments are plotted and a linear line is drawn through the points. Generally, a larger gradient has a positive influence on the progression rate. This is also supported by other types of sand and can be observed in Figure 4.2.

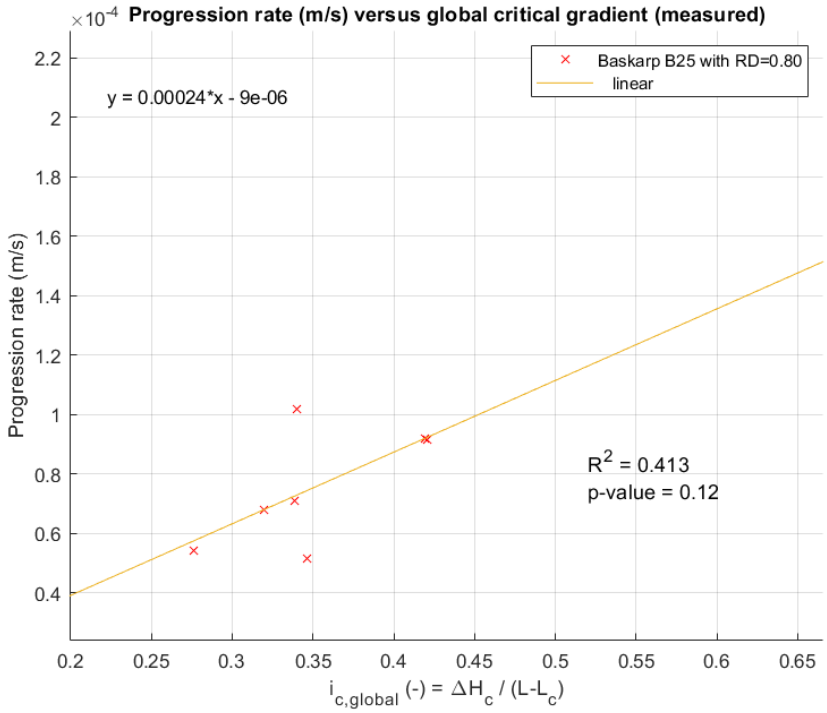

Figure 4.16: Progression rate versus global critical gradient (Baskarp B25).

The results of the selected experiments are analysed and evaluated in this chapter. From the measured data, the following two parameters show an influence of the progression rate:

- *d* Particle diameter (m)
- *k* Hydraulic conductivity (m/s)

The other two parameters (*RD* & *n)* does not show a direct influence on the progression rate, even though this was expected in the beginning of this thesis. The results in Figure 4.5 are too scattered to observe a clear relation.

5. Discussion

Section 5.1 focusses on the limitations of this research, highlighting the results, and where the results could be optimized. Section 5.2 discusses the applied models. In section 5.3 a more practical application of the progression rate is described.

5.1 Limitations of this research

In the experimental programme, three types of sand were applied: Baskarp B25, a common type of sand used in experiments, rather fine sand (FPH) and a coarser filter sand type (FS35). To answer the main research question which processes and parameters influence the progression and sediment transport rate, it was a bit ambiguous to answer this question for the three types of sand.

Amongst the three types of sand, there were differences in particle diameter, but also relative density (*RD*) and porosity. In the analysis, it was possible to examine the experiments with the same type of sand, but comparing the experiments with different sand characteristics was more complex. The two FPH experiments could only be compared to the Baskarp B25 experiments with relative density 0.8. FPH experiments with a relative density value of 0.5 were not performed, and could not be compared amongst the other sand types.

To create a broader reference, more experiments should be performed with different *RD* values. In total not many experiments were performed with the FS35 and FPH sand type, compared to the experiments with Baskarp B25.

During the monitoring of the experiments, many photographs and video recordings were performed to follow the development of the pipe. Although the monitoring was very valuable, it was difficult to observe the different processes during the pipe development. The increase in length is well documented, but the increase in depth and the different processes were difficult to distinguish. Especially difficult to distinguish were primary and secondary erosion and how these are influenced by different types of sand.

A suggestion is to study the different processes from the side of the pipe. There it should be possible to study the different processes and the depth of the pipe. All observations are now made from a top view. By knowing the instantaneous depth, the prediction of the primary sediment transport rate can be improved.

5.2 Applied models

While performing the experiments equation 2.19 was applied to calculate and describe the progression rate of the pipe. The pipe length was therefore monitored every timestep during the whole experiment. This equation is used to calculate the progression rate by dividing the length of the pipe over time and is presented in the last column ($v_{c,avg}$) of Table 4.1 (section 4.1).

Equation 2.19 gives a good presentation of the averaged progression rate but does not consider the instantaneous progression rate. Figure C.2.2 (Appendix C2) shows that the progression rate fluctuates during the progression phase. There are progression rate velocities of 2 cm/min, but

also 0.5 cm/min. A model which considers the variations of the progression rate at short timesteps could improve the estimations of pipe progression rate.

For the prediction of the primary sediment transport rate equation 4.3 is used. This equation transforms the velocity into a primary sediment transport rate. For the transformation, an averaged value for the depth and width is used. However, the pipe develops in time and therefore the width and the depth of the pipe vary in time as well. Consequently, in reality the sediment transport rate also varies in time.

Unfortunately, during the experiments, it was not possible to measure the instantaneous depth and width of the pipe because the laser measurements were performed after the moment of breakthrough. If the depth and width of the pipe are known during the development of the pipe a 3D model could be made as a function of time to monitor the development. There it could be observed that the averaged pipe depth is not constant, but increases when the pipe grows in length.

During the experiments, it is desired to measure the sediment transport rate and the critical flow velocity. This is all done in one experiment, to take advantage of the experimental setup. The sediment transport rate is calculated by collecting the sand accumulated in the sand boil during the development of a pipe (Figure 4.9). Right after the breakthrough of the pipe, the head is lowered in order to seek the critical flow velocity (dye injection).

However, the mass of the sand boil is not collected right after the breakthrough of the pipe, because this could negatively influence the conditions of the experiment setup. During the lowering of the head, particles were transported to the crater, biasing the results of the transport of mass. As an extra validation of the transported mass, the sand boil should be collected right after the moment of the breakthrough of the pipe. The downside of this approach is that the soil sample is affected by closing the valves and removing the sand boil. Also, the measuring of the equilibrium flow velocity is more challenging and probably affected by the removal of the sand boil.

The adapted model of Cheng (Equation 2.24) overestimates the sediment transport rate of the experiments. The results of the calculation are presented in Table 4.4 (section 4.3.4), including the lower and upper bound values. Equation 2.24 is very sensitive to the input of the parameters and therefore shows a large uncertainty in the results. The input of the parameters regards often averaged values, but also the formula of Cheng is based on the process of saltation of particles. During the experiments often sliding and rolling of the particles is observed. Still, it remains challenging to distinguish the different types of transport mechanisms on such a small-scale.

5.3. Application of the progression rate related to a real dike

From the performed experiments during this thesis, new knowledge is gained about the behaviour and shape of the pipe. If the averaged progression rate of the piping experiments is transformed to a real dike, the progression time can be calculated with equation 5.1. Table 5.1 presents the results of the calculation.

$$T_{progression} = \frac{L}{v_{c,avg}\, T_{day}} \tag{5.1}$$

With

$v_{c,avg}$ = Averaged progression rate (m/s)
L = Horizontal seepage length (m)
$T_{progression}$ = Time of the progression phase (days)
T_{day} = Time in seconds in a day (s) = 86400

Parameter	Symbol	Value
Progression rate Baskarp B25	$v_{c,avg}$	1.00E-04 m/s (8.64 m/day)
Seepage length real dike	L	80 m
Time of the progression phase	$T_{progression}$	9.25 days

Table 5.1: Results of the $T_{progression}$ calculation for a real dike.

If the results are compared to a historic flood wave in the Netherlands (Figure 5.1), it can be observed that the highest point in the graph has a duration of 1 or 2 days. The calculation shown above is performed for a constant critical head level; over a period of 9.25 days of continuous transport of sand for a dike with a d_{50}=0.22 mm (Baskarp B25).

The flood wave in Figure 5.1 has a duration of approximately 14 days. In this example, it cannot be concluded that the dike can withstand the flood wave concerning the failure mechanism of piping. This depends on the critical head difference (in Dutch= 'kritieke waterstand').

More study should be performed regarding the water levels on the inner and outer side of the dike. Depending on the critical water level of the dike, the critical flood period is shorter or longer than the progression rate of the pipe (9.25 days).

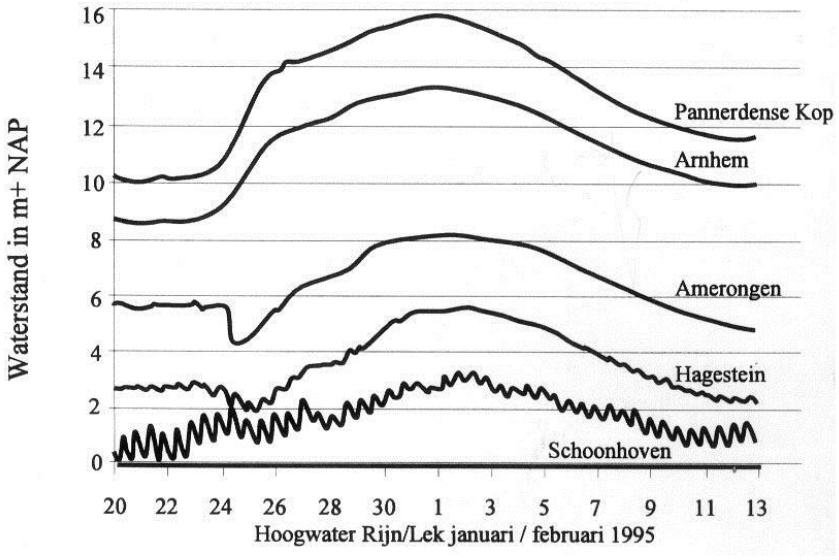

Figure 5.1: Flood wave from 1995 in the Netherlands (Lecture notes CTB3350).

All experiments were performed with rather uniform sand. In reality, the sand layers are more non-uniform. This is a preferred situation because the smaller particles will fill up the larger pores due to groundwater flow, which reduces the progression rate. This means that the required time for a pipe to develop is even more than the computed time in Table 5.1.

6. Conclusion

This chapter presents the main conclusions which were drawn in this thesis. Section 6.1 answers the sub-research questions and section 6.2 answers the main research question. The recommendations are presented in section 6.3.

6.1 Answers to sub-research questions

Sub-question 1: *Which experiments have already been performed concerning the progression rate of piping?*

The latest three piping experiments are extensively described in sections 2.2-2.4. The experiments from 2017 and 2018 contain the same type of piping experiments, applying a head difference through a soil sample, but differ in configuration and research objective. Robbins (Robbins et al., 2017) performed piping experiments in a large cylindrical setup, Allan (Allan, 2018) performed experiments in a medium-scale setup with the focus on overloading and Vandenboer (Vandenboer, 2018) used an equivalent setup but focussed on sudden supercritical loading. All three experiments are important for a better understanding of piping but have different objectives.

This research made a valuable contribution to past experiments by focussing on the sediment transport rate and the point of equilibrium ($\Delta H=\Delta H_c$). The past experiments present different results regarding the progression rate, but they do not provide a predictive model.

Sub-question 2: *How can the erosion process and the flow conditions be determined in the laboratory setup (adjusted setup of Van Beek)?*

For performing the piping experiments, the former small-scale setup of Vera van Beek (Van Beek, 2015) is used and modified. The top cover is modified by installing 15 pressure sensors perpendicular to the seepage path of the pipe. With this modification, it was possible to measure the pressure inside the pipe. Another adjustment was the installation of two filter-cloths. To ensure that the pipe was developing through the middle and below the pressure sensors.

For the measuring of the progression and sediment transport rates different measuring equipment (laser, single-lens reflex cameras, scale, dye injection) was installed to follow and measure the dimensions of the pipe. The amount of transported mass is known by measuring the weight of the sand boil. By monitoring the length of the pipe along with the experiment, the progression rate was determined. After the breakthrough of the pipe, the flow velocity was determined by monitoring a dye injection.

During experiments, it was unfortunately not possible to continuously measure the depth of the pipe and the flow velocity in the pipe. If this would have been possible, the bed shear stress could have been determined at every timestep and position. This could be very useful in the analysis of the sediment transport rate.

Sub-question 3: *How can the progression rate be modelled?*

The progression rate is measured by dividing the growth in length by the progression time (Equation 2.19). This initial approach calculates the measured averaged progression rate of the pipe during the progression phase. From the different plots in chapter four, it can be observed that the progression rate is influenced by the different parameters (K and d) of the soil sample.

Equation 4.9 and 4.10 present the adapted sediment transport equations derived by Cheng (Cheng, 2004). There it can be observed that the progression rate (Equation 4.10) is also a function of different soil characteristics (particle diameter). According to the results of the calculations, this model overpredicts the measured progression rate by a factor 18. This is partly due to the depth of the pipe, which has a significant influence on the progression rate. The smaller the depth, the higher the progression rate.

Equating 4.2 relates the calculated head difference with the measured head difference for the different groups of experiments. The results showed that the calculated head difference ($\Delta H_{c,Sellmeijer}$) overpredicts the measured head difference ($\Delta H_{c,measured}$) approximately by a factor 2. Sellmeijer's model (Equation 2.4 to 2.7) gives a good estimation in a 2D situation, but for the small-scale experiments (3D) the critical head difference is overpredicted.

In this thesis different models (v_{wal}, mass, Cheng) have been assessed and discussed. The measured results also present that the progression rate is governed by the hydraulic conductivity and the particle diameter. The experiments with a larger particle diameter have a higher progression rate and hydraulic conductivity. Experiments with a finer particle diameter result in a lower progression rate including a lower hydraulic conductivity.

6.2 Main research question

The main aim of this thesis is to answer the following research question:

How do the different parameters and processes influence the progression and the sediment transport rate in laboratory experiments of backward erosion piping?

From performing the experiments and subsequent analysis, two main parameters were obtained which influence the progression rate (Table 6.1). A green arrow is used to show an increase of the progression rate.

Parameter	Symbol	Effect on the progression rate
Particle diameter ↑*	d (m)	↑
Hydraulic conductivity ↑	k (m/s)	↑
Relative density $((e_{max}-e)/(e_{max}-e_{min}))$ ↑	RD (-)	No clear relation from datapoints
Porosity (volume of voids/total volume) (Vv/Vt) ↑	n (-)	No clear relation from datapoints

↑* (Increase of parameters)

Table 6.1: Overview of main parameters influencing the progression rate.

In general, it can be concluded that the experiments with finer sand have a lower progression rate than the experiments with coarser sands. This result goes against an initial hypothesis, by which coarser sands have a lower progression rate since they have a larger downforce due to

gravity. This is countered by the fact that the progression rate is not only a function of the particle diameter but also of the conditions of the soil such as the hydraulic conductivity. Influence of the porosity was also expected in the hypothesis (section 2.4.1), but could not be observed in the measurements (Figure 4.5).

Regarding the piping development processes; the local gradient plays an important role in the transportation of particles. During the development of the pipe, the pipe stops and continues for a constant applied head. When the gradient increases up to a certain value, the pores are filled with water until the pore pressure exceeds the friction between the grains, causing instability in the pipe. As a result, suddenly a large part of the sand sample is transported. This is a continuous cycle which was monitored during the development of the pipe and can also be seen in Figure 4.9. In the extensive analysis (section 4.3.5), it is shown that the averaged progression rate is lower than the wall velocity ($v_{c,avg} < v_{wal,avg}$). Therefore, the wall velocity (dilatancy) is not dominant in the progression rate.

The different calculations had two objectives: (1) to predict and quantify the sediment transport rate and (2) to understand the behaviour of the pipe. The experimental results deviate from the adapted model of Cheng (Figure 4.12). In the range of values, it can be seen that the model of Cheng is very sensitive to the input parameters and in addition, an averaged depth is applied rather than an instantaneous depth. Another factor is the shape of the pipe. It was observed that the pipe in Figure 4.13 has a meandering shape for a rather short length (i.e. 25 cm). This increases the complexity to predict a sediment discharge over a pipe shape that is different for all conducted experiments.

According to the experiments conducted in this research, the adapted formula of Cheng (Equation 2.24) overestimates the sediment transport rate in the pipe.

6.3 Recommendations

6.3.1 Formula to predict the progression rate

For a global and safe approximation of the progression rate equation 2.19 is a good definition, but for an extensive analysis equation 2.19 does not present detailed information regarding the total development of the pipe. It is recommended to derive a formula that contains the depending parameters of the progression rate.

To model and predict the progression rate, the parameter (hydraulic conductivity) which showed an influence is combined in an equation. The basis for this equation are the measured results of the three types of sand (fine, medium and coarser). By substituting a hydraulic conductivity, the averaged progression rate can be obtained (Figure 6.1).

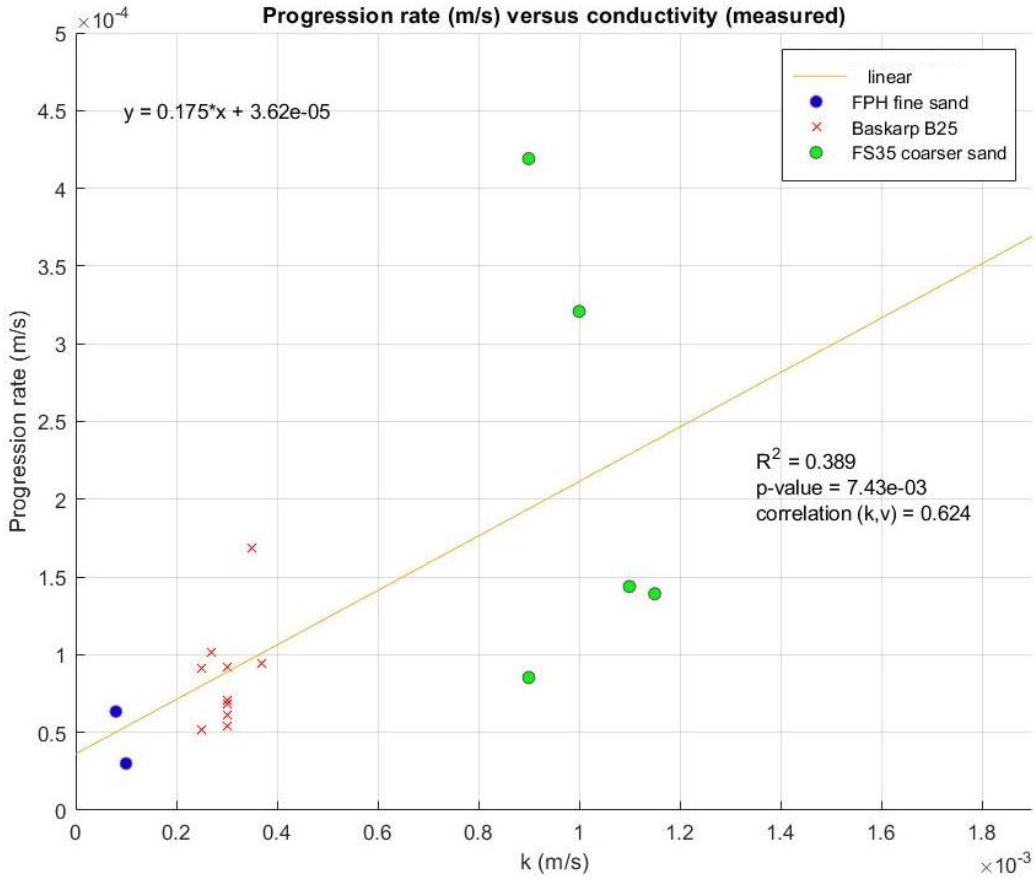

Figure 6.1: Linear relation for the hydraulic conductivity and progression rate.

Equation 6.1 predicts the progression rate by substituting the hydraulic conductivity into the formula. The equation is derived from the linear line.

$$v_{prediction} = 0.175\ k + 3.62\ 10^{-5} \tag{6.1}$$

With

$v_{prediction}$ = Predicted progression rate (m/s)
k = Hydraulic conductivity (m/s)

For further experiments and validation of this formula, equation 6.1 can be used as the first step to model the progression rate. When more points are added to the graph, it can be concluded if the linear fit (orange line) is the correct approach for the relation between the conductivity and the progression rate. Also, more parameters can be added, such as the particle diameter which showed an influence as well.

6.3.2 Medium-scale experiments

As an extra validation of the results, further research could be performed regarding medium-scale experiments. Performing medium-scale experiments would generate new data, which can be compared to the results of the small-scale experiments.

Due to the costs of medium-scale experiments, it is important to focus on 1 type of sand. The sand type Baskarp B25 can be used as a start. This is the same type of sand which is used in the small-scale experiments. Baskarp B25 is a commonly used sand type and available at Deltares.

The experiments with Baskarp B25 show almost identical results in the small-scale setup (Figure 6.1), therefore it is advised to compare this in the medium-scale setup. If there is more budget available, coarser sand experiments can also be performed (FS35 sand type). This additional research could lead to new insights regarding the behaviour of the pipe. It would also be interesting to know if the progression rate is influenced by a larger scale setup or not.

6.3.3 Experimental proposal small-scale experiments

From the 1st and 2nd experimental series (Table 3.1 and Table 3.2), only 17 experiments were selected for further analysis. A ratio of 17 out of 29 experiments is slightly low, remaining with 10 experiments Baskarp B25, 5 experiments FS35 sand and 2 experiments FPH sand. The other experiments were not selected, because the pipe developed sideward.

Since there are only 5 representative experiments with FS35 sand, more experiments can be performed with this type of sand. With more datapoints, the behaviour of this type of sand can be further studied, considering the fact that the results are now very scattered (Figure 6.1). It is advised to perform 10 more experiments with the sand type FS35 to create a wider base. Already expecting that a part of these experiments cannot be selected for further analysis.

Another valuable improvement is the measuring of the depth. If the depth can be constantly measured during the progression phase, more information is known during the development of the pipe (increase in length). With the instantaneous depth, the prediction of the primary sediment transport rate can be improved (Equation 4.2) and the calculation of the bed shear stresses. An option is to make a cross-section of the pipe (by laser), every minute during the progression phase.

Bibliography

Allan, R. J. (2018, April 12). *Backward Erosion Piping*. PhD Thesis, UNSW Australia, 2018.

Battjes, J. A., & Labeur, R. J. (2014). *Lecture notes CTB3350 Open Channel Flow*. Delft University of Technology, Faculty of Civil Engineering & Geosciences.

Cheng, N.-S. (2004). *Analysis of bedload transport in laminar flows*. School of Civil and Environmental Engineering, Nanyang Technological University.

De Groot, M. B., van der Ruyt, M. B., Mastbergen, D. R., & van den Ham, G. A. (2009). *Bresvloeiing in zand*. Geotechniek. July 2009, 34–39.

Delft Hydraulics. (1969). *Begin van beweging van bodemmateriaal*. Delft.

Einstein, H. A. (1950). *The bed-load function for sedimentation in open channel flows*. In: Shen HW, editor. Sedimentation. Fort Collins, Colorado, USA: Colorado State University; 1950.

Förster, U., van den Ham, G., Calle, E., & Kruse, G. (2012). *Onderzoeksrapport Zandmeevoerende wellen*. Deltares.

Fox, R. W., Pritchard, P. J., & McDonald, A. T. (2009). *Introduction to fluid mechanics*. John Wiley & Sons; New York.

Girgis, A. (1977). *Transport of fine bed sand by laminar and turbulent water flows*. PhD Thesis, University of London.

Hanses, U. (1985). *Zur Mechanik der Entwicklung von Erosionskanälen in geschichtetem Untergrund unter Stauanlagen*. Dissertation Grundbauinstitut der Technischen Universität Berlin, Germany.

Hoffmans, G., & Van Rijn, L. (2018). Hydraulic approach for predicting piping in dikes. *Journal of Hydraulic Research*, *56*(2), 268–281. https://doi.org/10.1080/00221686.2017.1315747

Jansen, P. Ph., van Bendegom, L., van den Berg, J., de Vries, M., & Zanen, A. (1979). *Principles of River Engineering*. Delftse Uitgevers Maatschappij b.v.

Jonkman, S. N., Jorissen, R. E., & Schweckendieck, T. (2017). *Lecture notes CIE5314 Flood defences—2nd edition 2017*. 375.

Nikuradse, J. (1933). *In Stromungsgesetz in rauhren rohren*. Tech. Rep. NACA Technical Memorandum 1292.

Pol, J. C., van Beek, V. M., Kanning, W., & Jonkman, S. N. (2019). *Progression rate of backward erosion piping in laboratory experiments and reliability analysis*. 6.

Pol, J., Kanning, W., & Jonkman, S. (2020). *Temporal development of backward erosion piping in a large scale experiment*. (In review).

Robbins, B. A., van Beek, V. M., López-Soto, J. F., Montalvo-Bartolomei, A. M., & Murphy, J. (2017). A novel laboratory test for backward erosion piping. *International Journal of Physical Modelling in Geotechnics*, *18*(5), 266–279. https://doi.org/10.1680/jphmg.17.00016

Rotunno, A. F., Callari, C., & Froiio, F. (2017). Computational Modeling of Backward Erosion Piping. In M. Frémond, F. Maceri, & G. Vairo (Eds.), *Models, Simulation, and Experimental Issues in Structural Mechanics* (Vol. 8, pp. 225–234). Springer International Publishing. https://doi.org/10.1007/978-3-319-48884-4_12

Schiereck, G. J. (2012). *Introduction to Bed, bank and shore protection* (2nd edition). ISBN 978-90-6562-306-5, Published by VSSD, Delft.

Schmertmann, J. H. (2000). *The non-filter factor of safety against piping through sands*. F.ASCE, Dept. Of Civil Engineering, University of Florida, Gainesville, FL.

Sellmeijer, H., Lopez de la Cruz, J., Van Beek, V. M., & Knoeff, H. (2011). *Fine-tuning of the backward erosion piping model through small-scale, medium-scale and IJkdijk experiments.* European Journal of Environmental and Civil Engineering 15(8). p1139-1154.

Shields, A. (1936). *Anwendung der Aenlichtkeitsmechanik und der Turbulenzforschung auf die Geschiebebewegung*. Preussischen Versuchsanstalt fur Wasserbouw.

Townsend, F. C., Bloomquist, D., Shiau, J.-M., Martinez, R., & Rubin, H. (1988). *Analytical and experimental evaluation of piping and filter design for sands*. Technical report, Department of Civil Engineering, University of Florida, Gainesville.

Van Beek, V., Knoeff, H., & Schweckendiek, T. (2011). *Piping: Over 100 years of experience: From empiricism towards reliability-based design*. Deltares select series (ISSN 1877-5608 ; vol. 7)

Van Beek, V. M., Bezuijen, A., & Sellmeijer, H. (2013). *Backward Erosion Piping*. In Bonelli, S. and Nicot, F., editors, Erosion in Geomechanics Applied to Dams and Levees, pages 193-269. John Wiley & Sons, Inc., Hoboken.

Van Beek, Vera M. (2015). *Backward Erosion Piping—Initiation and Progression*. PhD Thesis, Delft University of Technology, 2015.

Van Beek, V. M., & Hoffmans, G. J. C. M. (2017). *Evaluation of Dutch backward erosion piping models and a future perspective*. Deltares.

Van Beek, Vera M., Robbins, B. A., Hoffmans, G. J. C. M., Bezuijen, A., & van Rijn, L. C. (2019). Use of incipient motion data for backward erosion piping models. *International Journal of Sediment Research, 34*(5), 401–408. https://doi.org/10.1016/j.ijsrc.2019.03.001

Van Beek, V.M., Knoef, J. G., Rietdijk, J., Sellmijer, J. B., & Lopez De La Cruz, J. (2010). *Influence of sand and scale on the piping process: Experiments and multivariate analysis in Physical modelling in geotechnics*. L.S. Springman, editor. Taylor and Francis group: London. p.1221-1226.

Van der Linden, T. I. (2016). *Influence of Multiple Thin Soft Layers on the Cone Resistance in Intermediate Soils*. MSc Thesis, Delft University of Technology, Delft.

Van der Zee, R. (2011). *Influence of sand characteristics of the piping process- research to the influence of grain size and other sand characteristics on the critical head of piping*. MSc Thesis, Delft University of Technology, Delft.

Vandenboer, K. (2018). *A study on the mechanisms of backward erosion piping*. PhD Thesis, Ghent University, 2018.

Vanoni, V. A., American Society of Civil Engineers, & Environmental and Water Resources Institute (U.S.) (Eds.). (2006). *Sedimentation engineering* (2nd ed). American Society of Civil Engineers.

White, C. (1940). *The equilibrium of grains on the bed of a stream*. Proceedings of the Royal Society of London. Series A, Mathematical and Physical Sciences, 174:322-338.

Appendix A – Piping checklist

Piping Checklist:

1	Re-apply plasticine on top
2	Check green filter material in capillaries
3	Check sealing on container cover and apply silicone if required
4	Apply grease to container where container cover seals (brown strip)
5	Ensure grease-free container cover in areas with sand contact.
6	Check silicone film on top cover and cap (the “piping-exit” cap marked with a cross)
7	Grease top cylinder and cap
8	Place cap and top cylinder on container cover with sealing plug. Bolt-on the top cylinder with metal extender screws.
9	Bolt cover on container. Don’t forget metal square strip. Keep ~1.5mm gap between lid and container. Don’t overtighten.
10	Put container upright and fill with de-aired water from bottom.
11	De-air bottom filter by tamping.
12	De-air pressure transducer ports.
13	Fill container as per test requirements. Ensure enough water height, even at 0% rel. dens. Check for air trapped at the top block of the container. Use small amounts of sand at each time raining in to keep any air out. Weigh dry sand mass added
14	If you densify by compaction, make sure; you have a bottom drain open and at correct height.
15	Check sand infill at top (awkward construction hampers sand infill)
16	Trim any excess sand for closing the lid. There’s a special cut tool for this (looks like a “T”).
17	Weigh back any sediment in water you may have had to take out again.
18	Clean all bolt threads.
19	Grease Gardena connections
20	De-air filter stone at exit-cover and top capillary.
21	Grease top seal
22	Close container, use low amounts of torque for fastening the exit-cover and tighten in a repetitive circular manner.
23	Connect hose to outlet, fill with water and tap filter stone with thin needle to remove any remaining air.
24	Check if container seals correctly by increasing water pressure by means of hydraulic head.
25	Check for any residual air with top most capillary.
26	Tilt container to horizontal position.
27	Place laser frame if needed. Align the box with the laser frame.
28	Fill top container partly with water and lower pressure again.
29	Connect in- and outflow
30	Close top cylinder. Ensure o-ring is greased.
31	Fill out-flow up to Gardena valve
32	Fill remaining hose (in and out)
33	De-air capillaries at inflow and outflow. Check if the hydraulic head is zero.
34	Slowly (5 minutes) open out-flow by means of a hose-clamp, while inflow is closed.
35	Connect dye injection

36	Align for camera and laser. Check whether box is placed horizontally.
37	Place lighting
38	Check camera > lighting, zoom, focus.
39	Place scale and bucket for flow rate measurements
40	Start Test!

During experiment:

41	Head increase in steps of 1 cm, 0.5 cm and 0.2 cm.

After experiment is finished:

42	Close inflow valve
43	Close pressure transducers
44	Take last photos with stopwatch in view
45	Stop and move cameras.
46	Stop pressure monitoring
47	Empty exit hose and cylinder, open cylinder cap carefully
48	Measure sand cone dimensions. Collect sand from volcano > dry 24h in the oven at 105 degrees C
49	Insert the plug into the exit + fix with pin and bolts
50	Place container in the vertical position
51	Remove lid
52	Remove sand (leave pressure ports underwater)
53	Clean inner side of the container
54	Ready for the next test!

Appendix B – Sieve curve

B1. Baskarp B25

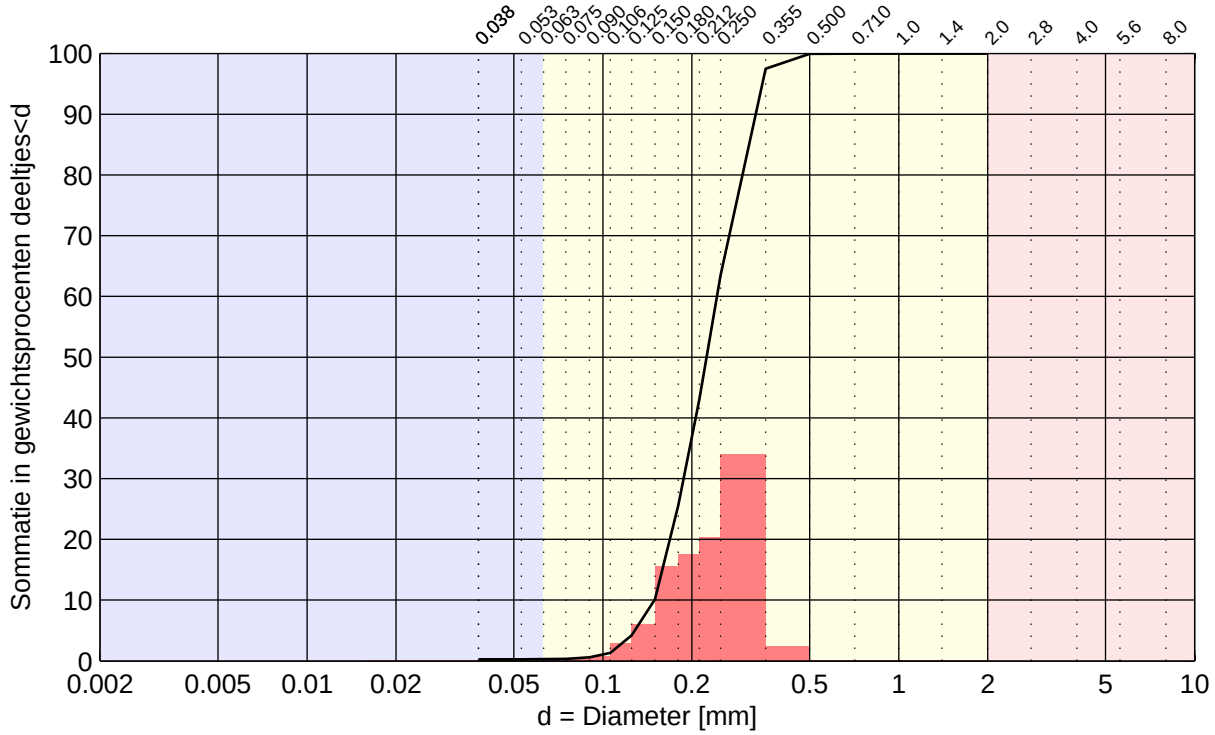

Kengetal	Waarde
d_{10} [mm]	0.149
d_{15} [mm]	0.159
d_{50} [mm]	0.224
d_{60} [mm]	0.243
d_{60}/d_{10} [−]	1.6
d_{90}/d_{10} [−]	2.2
C_c [−]	0.97
M_{63} [µm]	224
M_{2000} [mm]	–
D_m [mm]	0.230
F_m [−]	1.32
U [−]	47.5

Legenda	Boring	Monster	Diepte t.o.v. ma..
———	B25	6	0 − 0

Fijne fractie		Zandzeving: 159.35 g				Grind fractie: 0...	
d [mm]	%	d [mm]	%	d [mm]	%	d [mm]	%
–	–	–	–	0.180	25.6	–	–
0.001	–	0.038	0.2	0.212	43.1	2.8	–
0.002	–	0.053	0.2	0.250	63.4	4.0	–
0.004	–	0.063	0.3	0.355	97.5	5.6	–
0.006	–	0.075	0.3	0.500	100.0	8.0	–
0.008	–	0.090	0.6	0.710	100.0	11.2	–
0.010	–	0.106	1.3	1.0	100.0	16.0	–
0.016	–	0.125	4.2	1.4	100.0	31.5	–
0.030	–	0.150	10.1	2.0	100.0	63.0	–

Beschrijving proefuitvoering
Beschrijving volgens NEN5104: Zand, zwak siltig
Volumieke massa 2.65x10^3 kg/m^3. Aangenomen waarde
Methode: Deltares
Bepaling fijne fractie: Geen
Bepaling grove fractie: Geen

Commentaar
Analyse uitgevoerd door: Deltares
Boormethode: Graven
Mengmonster: nee

Deltares
Postbus 177, 2600 MH Delft
Boussinesqweg 1, 2629HV Delft
Telefoon (0)88 335 8273
Telefax (0)88 335 8582
Homepage:
www.deltares.nl

datum	get.
2017−10−11	hks

GeoHal
getechnische werkzaamheden
KORRELVERDELING

project	Versie
11000036.002	*)
bijlage	form.
K6	A4

B2. FPH and FS35 sand

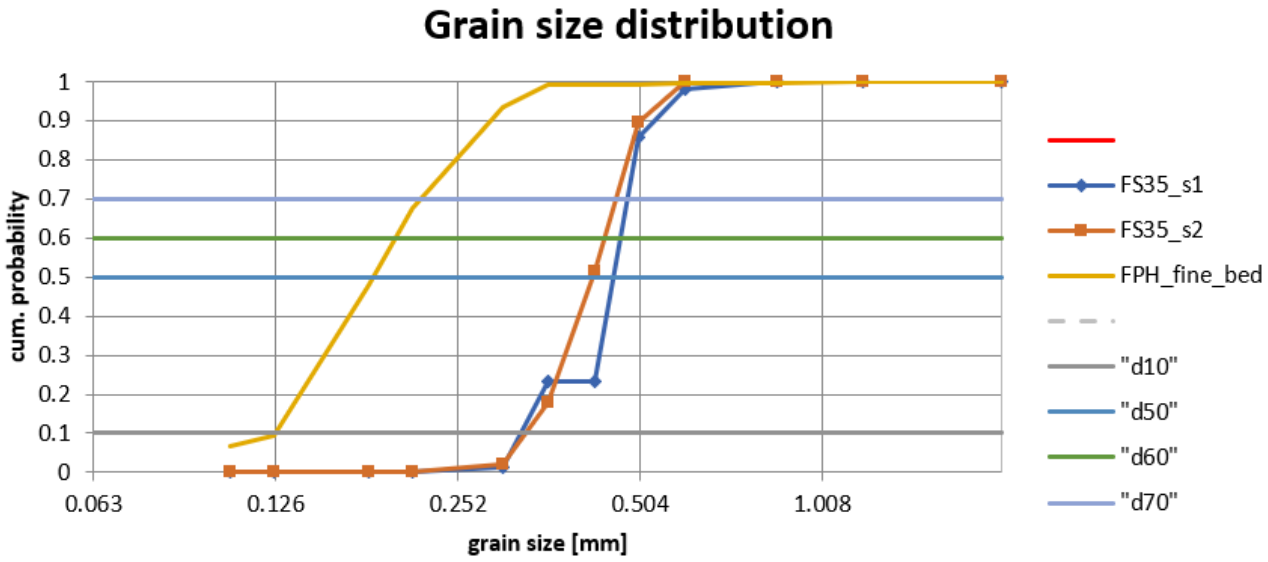

Appendix C – Reference experiment B25-229

C1. Observations experiment B25-229

Observations Experiment B25-229	**Date: 14-08-2019**
Time	**Observation**
8:57	Start
	P12 responds with some delay
	P13 is not as stable as the rest, but seems to give the right values on average.
	Flow directly at head increase to dH=1 cm. Previous times there was more delay.
	Initial sand crater of 1.5 cm from preparation
9:19	(dH=5) Sand boils over exit hole
9:37	Pipes grows along both filter guides and in both directions
	Pipe grows under P3
9:46	After 2.2 mm head increase, the head is lowered again with 2.2 mm
9:52	Pipe grows towards P4
9:53	P5 and P6 had the same head up till now. More resistance between P4 and P5.
10:02	Macro. Op T=3650 en t=3660. Particles are constantly moving, seem not to deposit in front of pipe tip.
10:20	Test dye injection (pipe breakthrough after 83 minutes)
10:23	Head adjusted, now equilibrium conditions found
10:30	Laser scan (equilibrium)
10:45	Dye injection in P14
	Widening
11:02	Head increased to 7 cm again
11:03	Dye injection P14 (tstart=7580)
11:07	Dye injection P15
11:09	Laser scan at 12.5 cm (tstart=7970, tend=8000)
11:12	Dye injection P14 (tstart=8135, tend=8205)
11:14	Laser scan at 12.5 cm (tstart=8220, tend=8274)
11:17	Dye injection P14 (tstart=8410, tend=8530)
11:23	Equilibrium. Large void at upstream filter.
11:30	Laser scan
11:51	Dye injection P15
11:53	Dye injection P14
11:55	Finished

C2. Results of the reference experiment B25-229

The characteristic results from the development of the pipe (experiment B25-229) are presented in this section. Different plots are shown regarding the pipe length, flow rate and progression rate.

Figure C.2.1 presents the head difference versus the length development of the pipe.
It can be seen that the pipe further progresses until failure when the head difference remains constant (at 7.05 cm).

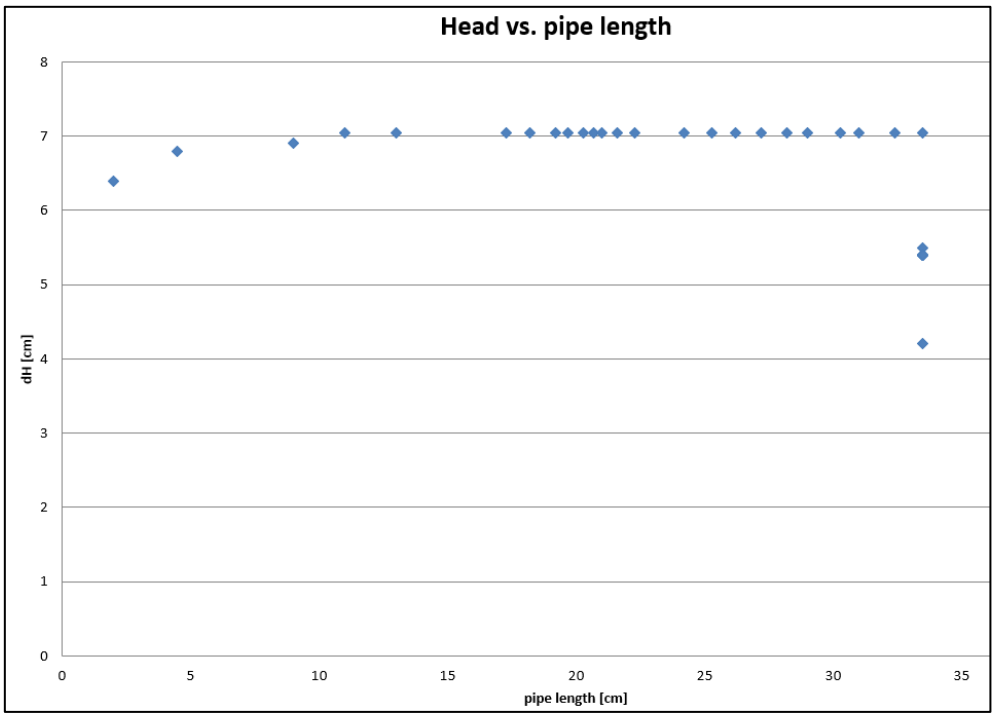

Figure C.2.1: Development of the head difference versus the pipe length (B25-229).

The head difference is increased in steps of 1 cm every 5 minutes. Figure C.2.1 represents the head difference versus the change in the slope of the progression rate. The change in slope is defined as a change in pipe length divided by change in time: $\Delta L/\Delta t$ [cm/min]. When the critical head difference has obtained the length of the pipe is measured every minute. At the beginning of the experiment, the length of the pipe is not measured in every single timestep. This results in empty cells in the observation sheet and produces some outliers.

Figure C.2.2 demonstrates the change in slope versus the time. The pipe length is measured every minute until the pipe is fully developed. The pipe length increases with an average value of 0.87 cm/min, neglecting the outliers. The change in slope (blue line) is defined as *dL/dt*. The increase of length divided by the timestep. The higher the slope, the steeper the red line in Figure 3.11

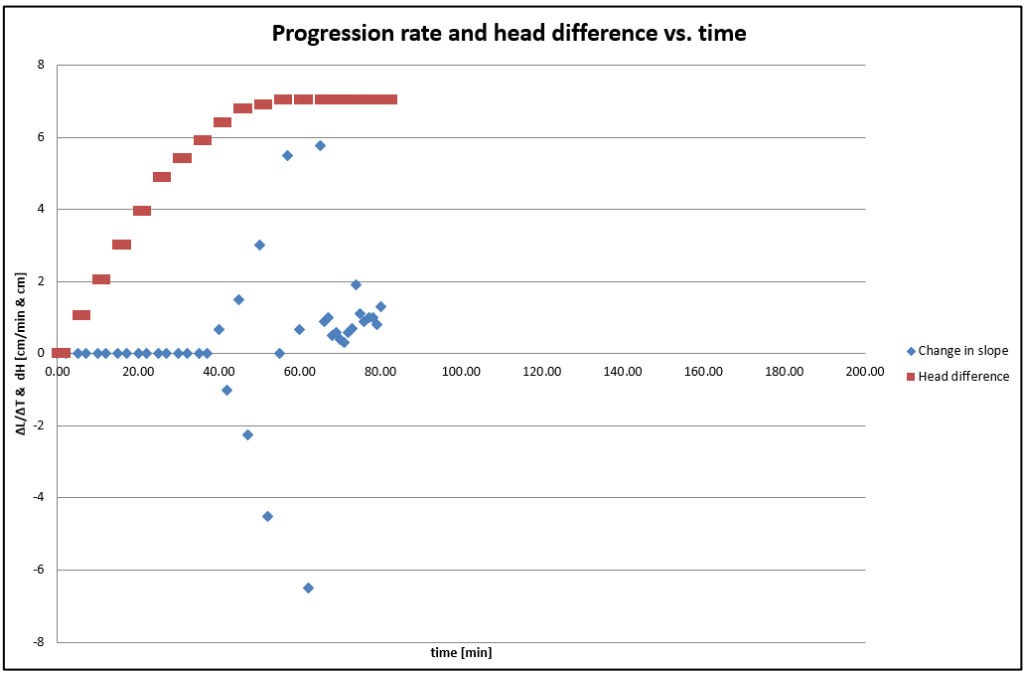

Figure C.2.2: Development of the head difference versus the change in slope (B25-229).

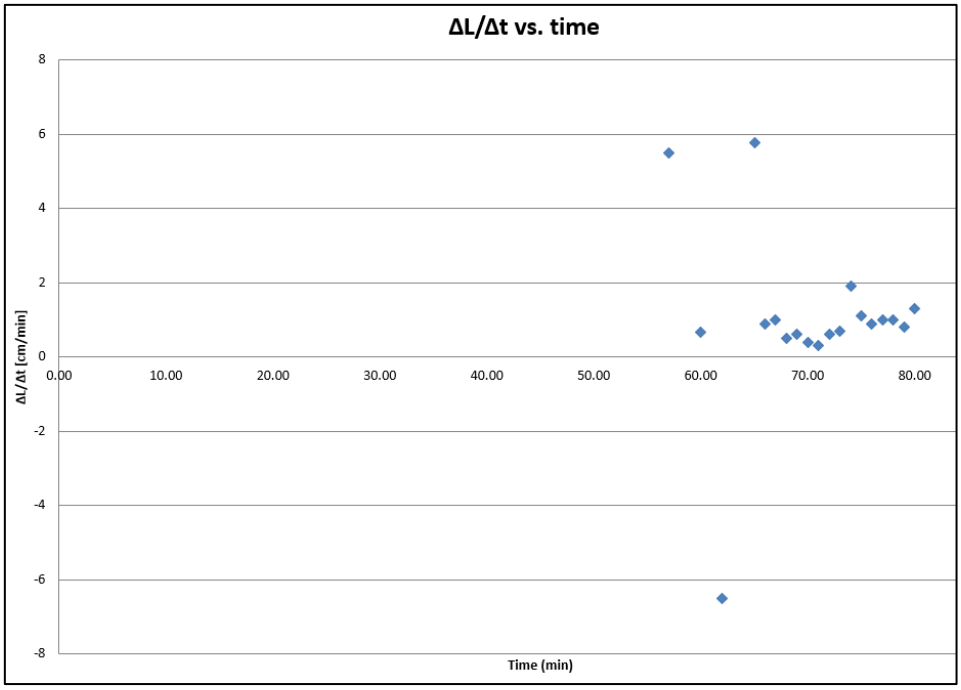

Figure C.2.3: Change in slope of the progression rate [cm/min] versus time (B25-229).

Flow rate

The flow rate is monitored during the experiment by measuring the weight of the outflow bucket. Figure C.2.4 presents the flow rate (ml/min) versus the head difference and Figure C.2.5 the development of the flow rate over time. When the pipe is fully developed the flow rate drops at t=83 minutes.

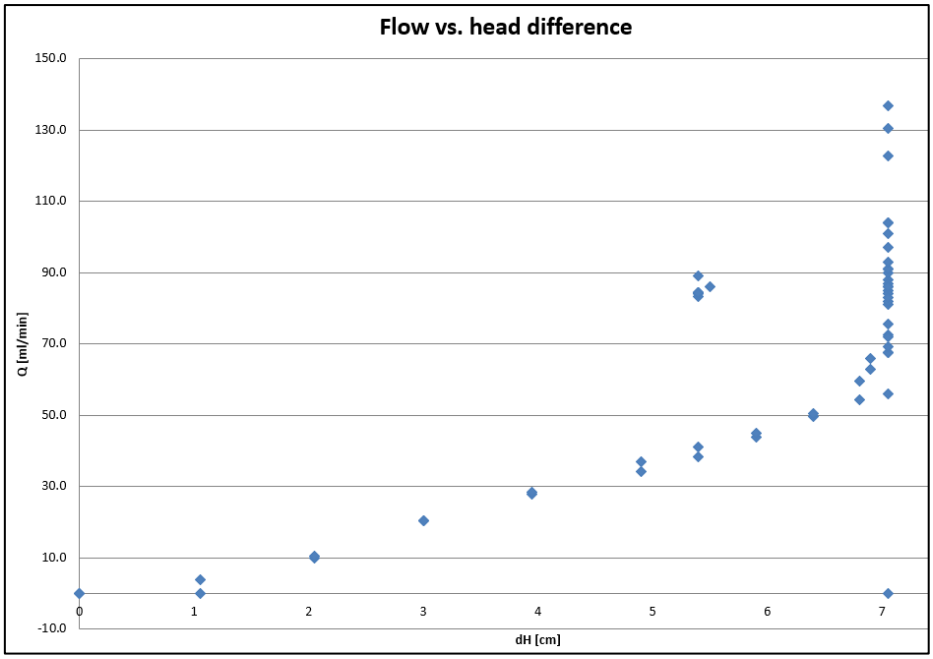

Figure C.2 4: The flow rate [ml/min] versus the head difference (B25-229).

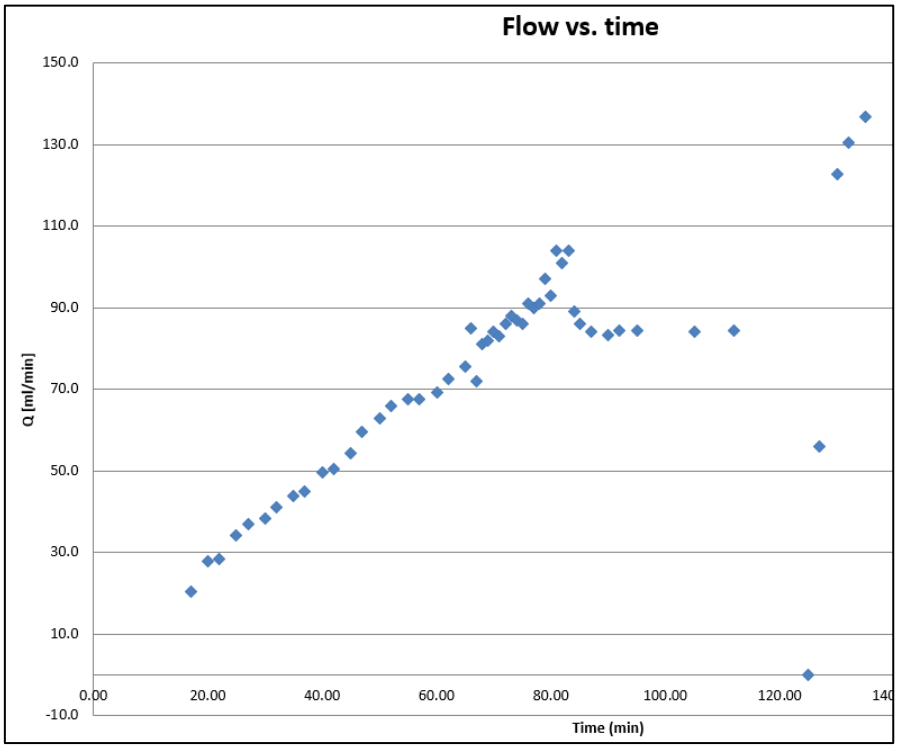

Figure C.2.5: Development of the flow rate over time (B25-229).

Appendix D – ΔH_c Sellmeijer calculation

This Appendix presents the results of the critical head calculations regarding Sellmeijer's model. To calculate the critical head the following equations are applied.

$$\Delta H_c = L\, F_r\, F_s\, F_g \tag{2.4}$$

$$F_{resistance} = \eta \left(\frac{\gamma'_p}{\gamma_w}\right) tan(\theta) \left(\frac{RD}{RD_m}\right)^{0.35} \tag{2.5}$$

$$F_{scale} = \frac{d_{70m}}{\sqrt[3]{kL}} \left(\frac{d_{70}}{d_{70m}}\right)^{0.4} \tag{2.6}$$

$$F_{geometry} = 0.91 * \left(\frac{D}{L}\right)^{\frac{0.28}{\left(\frac{D}{L}\right)^{2.8}-1}+0.04} \tag{2.7}$$

With:

ΔH_c =	*Critical head difference (m)*
L =	*Horizontal seepage length (m)*
γ'_p =	*Submerged volumetric weight sand (kN/m^3)*
γ_w =	*Volumetric weight water (kN/m^3)*
θ =	*Bedding angle (°)*
D =	*Aquifer thickness (m)*
η =	*Constant of white (-)*
κ =	*Intrinsic permeability of the aquifer (m^2)*
RD =	*Relative density ($(e_{max}-e)/(e_{max}-e_{min})$) (-)*
RD_m =	*Averaged relative density in small-scale tests (0,725)*
$d70$ =	*70%-fractile of grain size distribution (m)*
$d70_m$ =	*Reference value for d_{70} in small-scale tests (2.08*10^{-4} m)*

D1. ΔH_c Sellmeijer (1)

Type of sand		Baskarp B25	Baskarp B25	FPH	FPH
Parameter	**Symbol**	**Value**	**Value**	**Value**	**Value**
Seepage length	L	0.345 m	0.345 m	0.345 m	0.345 m
Submerged volumetric weight sand	γ'_p	16.5 kN/m^3	16.5 kN/m^3	16.1 kN/m^3	16.1 kN/m^3
Volumetric weight water	γ_w	10 kN/m^3	10 kN/m^3	10 kN/m^3	10 kN/m^3
Bedding angle	θ	37 °	37 °	37 °	37 °
Aquifer thickness	D	0.1	0.1	0.1	0.1
Constant of white	η	0.25	0.25	0.25	0.25
Intrinsic permeability of the aquifer (m^2)	κ	3.823E-11 m^2	4.609E-11 m^2	1.355E-11 m^2	1.085E-11 m^2
Kinematic viscosity	υ	1.33E-06 m^2/s	1.33E-06 m^2/s	1.33E-06 m^2/s	1.33E-06 m^2/s
Acceleration of gravity	g	9.81 m/s^2	9.81 m/s^2	9.81 m/s^2	9.81 m/s^2
Hydraulic conductivity	k	2.82E-04 m/s	3.40E-04 m/s	1.00E-04 m/s	8.0E-05 m/s
Relative density ((e_{max}-e)/(e_{max} – e_{min}))	RD	0.8	0.55	0.74	0.79
Averaged relative density in small-scale tests	RD_m	0.725	0.725	0.725	0.725
70%-fractile of grain size distribution	$d70$	2.9*10^{-4} m	2.9*10^{-4} m	2.2*10^{-4} m	2.2*10^{-4} m
Reference value for d_{70} in small-scale tests	$d70_m$	2.08*10^{-4} m	2.08*10^{-4} m	2.08*10^{-4} m	2.08*10^{-4} m
F resistance	$F_{resistance}$	0.3217	0.2822	0.3055	0.3126
F scale	F_{scale}	1.005	0.9447	1.3702	1.3702
F geometry	$F_{geometry}$	1.2387	1.2387	1.2720	1.2387
Critical head difference	$\boldsymbol{\Delta H_c}$	**0.138 m**	**0.114 m**	**0.166 m**	**0.183 m**

$$\kappa = \frac{\upsilon}{g} k$$

With:

κ = *Intrinsic permeability of the aquifer (m^2)*
υ = *Kinematic viscosity (1.33E-06 m^2/s)*
g = *Acceleration of gravity (m^2/s)*
k = *Hydraulic conductivity (m/s)*

D2. ΔH_c Sellmeijer (2)

Type of sand		FS35	FS35	FS35	FS35
Parameter	**Symbol**	**Value**	**Value**	**Value**	**Value**
Seepage length	L	0.345 m	0.345 m	0.345 m	0.345 m
Submerged volumetric weight sand	γ'_p	16.5 kN/m^3	16.5 kN/m^3	16.5 kN/m^3	16.5 kN/m^3
Volumetric weight water	γ_w	10 kN/m^3	10 kN/m^3	10 kN/m^3	10 kN/m^3
Bedding angle	θ	37 °	37 °	37 °	37 °
Aquifer thickness	D	0.1	0.1	0.1	0.1
Constant of white	η	0.25	0.25	0.25	0.25
Intrinsic permeability of the aquifer (m^2)	κ	1.532E-10 m^2	1.3550E-10 m^2	1.220E-10 m^2	1.220E-10 m^2
Kinematic viscosity	υ	1.33E-06 m^2/s	1.33E-06 m^2/s	1.33E-06 m^2/s	1.33E-06 m^2/s
Acceleration of gravity	g	9.81 m/s^2	9.81 m/s^2	9.81 m/s^2	9.81 m/s^2
Hydraulic conductivity	k	1.13E-03 m/s	1.0E-03 m/s	9.0E-04 m/s	9.0E-04 m/s
Relative density ((e_{max}-e)/(e_{max} – e_{min}))	RD	0.49	0.67	0.72	0.77
Averaged relative density in small-scale tests	RD_m	0.725	0.725	0.725	0.725
70%-fractile of grain size distribution	$d70$	4.62*10^{-4} m	4.62*10^{-4} m	4.62*10^{-4} m	4.62*10^{-4} m
Reference value for d_{70} in small-scale tests	$d70_m$	2.08*10^{-4} m	2.08*10^{-4} m	2.08*10^{-4} m	2.08*10^{-4} m
F resistance	$F_{resistance}$	0.2710	0.3024	0.3101	0.3175
F scale	F_{scale}	0.7627	0.7944	0.8228	0.8228
F geometry	$F_{geometry}$	1.2387	1.2387	1.2387	1.2387
Critical head difference	$\boldsymbol{\Delta H_c}$	**0.088 m**	**0.103 m**	**0.1090 m**	**0.1116 m**

Appendix E – Calculation of the crater mass

Overview of the collected data of all experiments

Experiment	Outer radius (r_b) (cm)	Edge radius (r_c) (cm)	Outer slope (α_0) (°)	Inner slope (α_i) (°)	Boil porosity (-) (n_{crater})	Particle density (g/cm3)	Measured mass (g)	Predicted volume (cm^3)	Predicted mass (g)
B25_232	3.2	1.5	36.33	21.80	0.407	2.65	33.37	15.810	25.705
B25_233	2.45	1.6	44.66	27.14	0.451	2.65	12.77	6.824	11.094
B25_234	2.1	1.3	42.38	23.68	0.432	2.65	8.64	4.172	6.784
FPH_235	3	1.4	36.18	24.23	0.419	2.61	26.2	12.920	20.689
B25_236	2.4	1.2	34.99	29.18	0.413	2.65	12.23	6.391	10.391
FPH_237	2.05	1.1	41.14	19.52	0.449	2.61	8.88	3.861	6.183
FS35_239	3.1	1.7	34.44	26.29	0.311	2.65	27.98	14.316	23.277
FS35_240	3.8	1.95	34.47	37.59	0.388	2.65	45.67	26.985	43.875
FS35_241	3.15	1.65	36.75	39.68	0.370	2.65	28.45	15.051	24.471
Averaged value			**35.2**	**33.1**	**0.386**				

Table E.1: Overview of the measured data for all experiments.

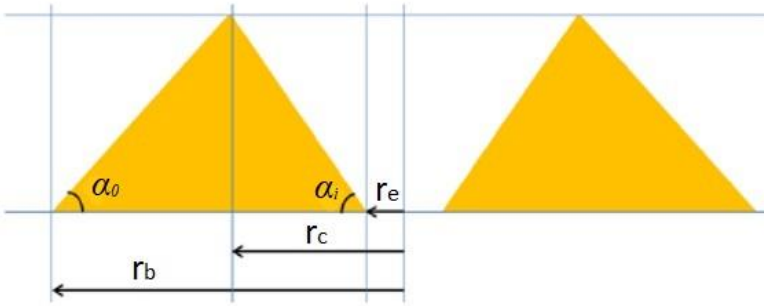

Figure E.1: Schematic cross-section of the crater.

$$m = V\,(1 - n_{crater})\,\rho_s \tag{E.1}$$

$$V = \frac{\pi}{3}\left[tan(\alpha_0)(r_b^3 - r_c^3) + tan(\alpha_i)(r_e^3 - r_c^3)\right] \tag{E.2}$$

$$r_c = \frac{r_b\,tan(\alpha_0) + r_e\,tan(\alpha_i)}{tan(\alpha_0) + tan(\alpha_i)} \tag{E.3}$$

With:

m =	*Mass of the sand crater(g)*
V =	*Volume of the sand crater (cm^3)*
n_{crater} =	*Averaged porosity of the sand craters (-)*
ρ_s =	*Particle density (kg/m^3)*
α_0 =	*Averaged outer slope (°)*
α_i =	*Averaged Inner slope (°)*
r_b =	*Outer radius of the sand boil (cm)*
r_e =	*Exit radius (0.3 cm)*
r_c =	*Edge radius of the crater (cm)*

Appendix F – Observation sheet Experiment FPH – 235

General information

Test name	FPH-235	
Date	12-9-2019	
Temp room	21	degC
Temp water	20.8	degC

Setup

Setup	ss box, 6 mm hole exit, smooth cover	
Guides	guides 3.5 cm apart, 1.5 cm filter fabric + 2 mm silicon with sand, diagonal silicon	
Seepage length	0.35	m
L	0.48	m
D	0.1	m
W	0.3	m
Volume box	0.0144	m3
Monitoring	2 riser tubes, pwp sensors, DSLR camera top, ISAW exit, manual balance, dye	

Sand properties

Sand type	FPH_fine	
Dry mass sand	22.59336	kg
Particle density	2610	kg/m3
porosity	0.399	-
void ratio	0.663	-
nmin	0.361	-
emin	0.565	-
nmax	0.485	-
emax	0.942	-
Dr	0.738	-
dry mass sand b	26.200	g

Results

Hcrit	8.65
Lcrit	10.800
vc,avg	0.180

Observations

actual time	time stopwatch	t [min]	h1 [cm]	h2 [cm]	dH [cm]	mass scale [g]	cumulative mass w	End weight bucket	D [cm]	L [cm]	dye?	laser?	Flow [ml/min]	Q/H [cm2/min]	DL/Dt [cm/min]	
13:18:00	00:00:00	0.00	43.35	43.35	0	0	0		0	0						
	00:02:00	2.00	43.35	43.35	0	0	0									0
	00:05:00	5.00	43.35	44.35	1	0	0									0
	00:07:00	7.00	43.35	44.35	1	0	0									0
	00:10:00	10.00	43.35	45.4	2.05	0	0									0
	00:12:00	12.00	43.35	45.4	2.05	0	0									0
	00:15:00	15.00	43.35	46.3	2.95	0	0		0.4							0
	00:17:00	17.00	43.35	46.3	2.95	0	0									0
	00:20:00	20.00	43.35	47.4	4.05	0	0									0
	00:22:00	22.00	43.35	47.4	4.05	11	11									0
	00:25:00	25.00	43.35	48.3	4.95	37	37		0.9				8.7	1.75		0
	00:27:00	27.00	43.35	48.3	4.95	55	55		0.9				9.0	1.82		0
	00:30:00	30.00	43.35	48.85	5.5	88	88		1				11.0	2.00		0

00:32:00	32.00	43.35	48.85	5.5	111	111	1		11.5	2.09	0
00:35:00	35.00	43.35	49.3	5.95	153	153	1.05		14.0	2.35	0
00:37:00	37.00	43.35	49.3	5.95	180	180	1.05		13.5	2.27	0
00:40:00	40.00	43.35	49.8	6.45	236	236	1.1		18.7	2.89	0
00:42:00	42.00	43.35	49.8	6.45	274	274	1.1		19.0	2.95	0
00:45:00	45.00	43.35	50.35	7	341	341	1.2		22.3	3.19	0
00:47:00	47.00	43.35	50.35	7	385	385	1.2		22.0	3.14	0
00:50:00	50.00	43.35	50.5	7.15	454	454	1.2		23.0	3.22	0
00:52:00	52.00	43.35	50.5	7.15	501	501	1.2		23.5	3.29	0
00:55:00	55.00	43.35	50.7	7.35	573	573	1.2		24.0	3.27	0
00:57:00	57.00	43.35	50.7	7.35	620	620	1.2	5	23.5	3.20	2.5
01:00:00	60.00	43.35	50.7	7.35	693	693	1.3	7.2	24.3	3.31	0.733333333
01:02:00	62.00	43.35	50.7	7.35	743	743	1.35	7.6	25.0	3.40	0.2
01:05:00	65.00	43.35	50.7	7.35	817	817	1.4	7.6	24.7	3.36	0
01:07:00	67.00	43.35	50.7	7.35	868	868	1.4	7.6	25.5	3.47	0
01:10:00	70.00	43.35	50.7	7.35	945	945	1.45	7.8	25.7	3.49	0.066666667
01:12:00	72.00	43.35	50.7	7.35	994	994	1.45	7.8	24.5	3.33	0
01:15:00	75.00	43.35	50.7	7.35	1070	1070	1.45	7.8	25.3	3.45	0
01:17:00	77.00	43.35	50.7	7.35	1120	1120	1.45	7.8	25.0	3.40	0
01:20:00	80.00	43.35	51	7.65	1198	1198	1.45	8.1	26.0	3.40	0.1
01:22:00	82.00	43.35	51	7.65	1250	1250	1.45	8.1	26.0	3.40	0
01:25:00	85.00	43.35	51.15	7.8	1328	1328	1.45	8.7	26.0	3.33	0.2
01:27:00	87.00	43.35	51.15	7.8	1382	1382	1.45	8.8	27.0	3.46	0.05
01:30:00	90.00	43.35	51.15	7.8	1462	1462	1.45	9.1	26.7	3.42	0.1
01:32:00	92.00	43.35	51.15	7.8	1515	1515	1.45	9.4	26.5	3.40	0.15
01:35:00	95.00	43.35	51.15	7.8	1594	1594	1.45	9.8	26.3	3.38	0.133333333
01:37:00	97.00	43.35	51.15	7.8	1647	1647	1.45	9.8	26.5	3.40	0
01:40:00	100.00	43.35	51.35	8	1730	1730	1.45	10	27.7	3.46	0.066666667
01:42:00	102.00	43.35	51.35	8	1785	1785	1.45	10	27.5	3.44	0
01:45:00	105.00	43.35	51.55	8.2	1869	1869	1.5	10.2	28.0	3.41	0.066666667
01:47:00	107.00	43.35	51.55	8.2	1925	1925	1.5	10.2	28.0	3.41	0
01:50:00	110.00	43.35	51.55	8.2	2010	2010	1.5	10.2	28.3	3.46	0
01:52:00	112.00	43.35	51.55	8.2	2067	2067	1.5	10.2	28.5	3.48	0
01:55:00	115.00	43.35	51.8	8.45	2155	2155	1.5	10.2	29.3	3.47	0
01:57:00	117.00	43.35	51.8	8.45	2213	2213	1.5	10.2	29.0	3.43	0
02:00:00	120.00	43.35	52	8.65	2302	2302	1.5	10.8	29.7	3.43	0.2
02:02:00	122.00	43.35	52	8.65	2362	2362	1.5	11.3	30.0	3.47	0.25
02:05:00	125.00	43.35	52	8.65	2451	2451	1.5	12.2	29.7	3.43	0.3
02:07:00	127.00	43.35	52	8.65	2512	2512	1.55	12.6	30.5	3.53	0.2
02:10:00	130.00	43.35	52	8.65	2604	2604	1.55	13.3	30.7	3.55	0.233333333
02:12:00	132.00	43.35	52	8.65	2666	2666	1.6	13.6	31.0	3.58	0.15
02:15:00	135.00	43.35	52	8.65	2759	2759	1.6	15.1	31.0	3.58	0.5
02:17:00	137.00	43.35	52	8.65	2821	2821	1.6	15.5	31.0	3.58	0.2
02:20:00	140.00	43.35	52	8.65	2914	2914	1.65	15.6	31.0	3.58	0.033333333
02:22:00	142.00	43.35	52	8.65	2978	2978	1.65	16.3	32.0	3.70	0.35
02:24:00	144.00	43.35	52	8.65	3041	3041	1.65	16.3	31.5	3.64	0
02:25:00	145.00	43.35	52	8.65	3073	3073	1.65	16.5	32.0	3.70	0.2
02:26:00	146.00	43.35	52	8.65	3106	3106	1.65	16.6	33.0	3.82	0.1
02:27:00	147.00	43.35	52	8.65	3138	3138	1.65	16.7	32.0	3.70	0.1
02:28:00	148.00	43.35	52	8.65	3169	3169	1.65	16.9	31.0	3.58	0.2

02:29:00	149.00	43.35	52	8.65	3201	3201	1.7	16.9	32.0	3.70	0
02:30:00	150.00	43.35	52	8.65	3233	3233	1.7	16.9	32.0	3.70	0
02:31:00	151.00	43.35	52	8.65	3264	3264	1.7	17.3	31.0	3.58	0.4
02:32:00	152.00	43.35	52	8.65	3301	3301	1.7	17.5	37.0	4.28	0.2
02:33:00	153.00	43.35	52	8.65	3331	3331	1.7	17.8	30.0	3.47	0.3
02:34:00	154.00	43.35	52	8.65	3364	3364	1.75	18.2	33.0	3.82	0.4
02:35:00	155.00	43.35	52	8.65	3395	3395	1.75	18.3	31.0	3.58	0.1
02:36:00	156.00	43.35	52	8.65	3429	3429	1.75	18.4	34.0	3.93	0.1
02:37:00	157.00	43.35	52	8.65	3461	3461	1.75	18.4	32.0	3.70	0
02:38:00	158.00	43.35	52	8.65	3494	3494	1.75	18.4	33.0	3.82	0
02:39:00	159.00	43.35	52	8.65	3526	3526	1.75	18.5	32.0	3.70	0.1
02:40:00	160.00	43.35	52	8.65	3560	3560	1.75	18.6	34.0	3.93	0.1
02:41:00	161.00	43.35	52	8.65	3593	3593	1.75	18.6	33.0	3.82	0
02:42:00	162.00	43.35	52	8.65	3623	3623	1.75	18.6	30.0	3.47	0
02:43:00	163.00	43.35	52	8.65	3657	3657	1.75	18.7	34.0	3.93	0.1
02:44:00	164.00	43.35	52	8.65	3692	3692	1.75	18.8	35.0	4.05	0.1
02:45:00	165.00	43.35	52	8.65	3725	3725	1.75	18.9	33.0	3.82	0.1
02:46:00	166.00	43.35	52	8.65	3760	3760	1.75	18.9	35.0	4.05	0
02:47:00	167.00	43.35	52	8.65	3793	3793	1.75	19	33.0	3.82	0.1
02:48:00	168.00	43.35	52	8.65	3826	3826	1.75	19.2	33.0	3.82	0.2
02:49:00	169.00	43.35	52	8.65	3860	3860	1.75	19.3	34.0	3.93	0.1
02:50:00	170.00	43.35	52	8.65	3894	3894	1.75	19.5	34.0	3.93	0.2
02:51:00	171.00	43.35	52	8.65	3928	3928	1.75	19.6	34.0	3.93	0.1
02:52:00	172.00	43.35	52	8.65	3962	3962	1.75	19.9	34.0	3.93	0.3
02:53:00	173.00	43.35	52	8.65	3998	3998	1.85	20	36.0	4.16	0.1
02:54:00	174.00	43.35	52	8.65	4030	4030	1.85	20	32.0	3.70	0
02:55:00	175.00	43.35	52	8.65	4060	4060	1.85	20	30.0	3.47	0
02:56:00	176.00	43.35	52	8.65	4098	4098	1.85	20	38.0	4.39	0
02:57:00	177.00	43.35	52	8.65	4130	4130	1.85	20	32.0	3.70	0
02:58:00	178.00	43.35	52.15	8.8	4163	4163	1.85	20.2	33.0	3.75	0.2
02:59:00	179.00	43.35	52.15	8.8	4197	4197	1.85	20.3	34.0	3.86	0.1
03:00:00	180.00	43.35	52.15	8.8	4233	4233	1.85	20.5	36.0	4.09	0.2
03:01:00	181.00	43.35	52.15	8.8	4266	4266	1.85	21	33.0	3.75	0.5
03:02:00	182.00	43.35	52.15	8.8	4302	4302	1.9	21.1	36.0	4.09	0.1
03:03:00	183.00	43.35	52.15	8.8	4338	4338	1.9	21.1	36.0	4.09	0
03:04:00	184.00	43.35	52.15	8.8	4370	4370	1.9	21.1	32.0	3.64	0
03:05:00	185.00	43.35	52.15	8.8	4405	4405	1.9	21.2	35.0	3.98	0.1
03:06:00	186.00	43.35	52.15	8.8	4440	4440	1.9	21.2	35.0	3.98	0
03:07:00	187.00	43.35	52.15	8.8	4474	4474	1.9	21.4	34.0	3.86	0.2
03:08:00	188.00	43.35	52.15	8.8	4510	4510	1.95	21.6	36.0	4.09	0.2
03:09:00	189.00	43.35	52.15	8.8	4544	4544	1.95	22.3	34.0	3.86	0.7
03:10:00	190.00	43.35	52.15	8.8	4581	4581	1.95	22.3	37.0	4.20	0
03:11:00	191.00	43.35	52.15	8.8	4615	4615	1.95	22.3	34.0	3.86	0
03:12:00	192.00	43.35	52.15	8.8	4650	4650	1.95	22.3	35.0	3.98	0
03:13:00	193.00	43.35	52.15	8.8	4685	4685	1.95	22.3	35.0	3.98	0
03:14:00	194.00	43.35	52.15	8.8	4718	4718	1.95	22.5	33.0	3.75	0.2
03:15:00	195.00	43.35	52.15	8.8	4754	4754	1.95	22.7	36.0	4.09	0.2
03:16:00	196.00	43.35	52.15	8.8	4790	4790	1.95	22.8	36.0	4.09	0.1
03:17:00	197.00	43.35	52.15	8.8	4823	4823	1.95	22.8	33.0	3.75	0
03:18:00	198.00	43.35	52.15	8.8	4860	4860	1.95	22.8	37.0	4.20	0

	03:19:00	199.00	43.35	52.15	8.8	4896	4896	2	22.8	36.0	4.09	0
	03:20:00	200.00	43.35	52.15	8.8	4935	4935	2	22.8	39.0	4.43	0
	03:21:00	201.00	43.35	52.15	8.8	4968	4968	2	23.2	33.0	3.75	0.4
	03:22:00	202.00	43.35	52.15	8.8	5003	5003	2	23.2	35.0	3.98	0
	03:23:00	203.00	43.35	52.15	8.8	5040	5040	2	23.2	37.0	4.20	0
	03:24:00	204.00	43.35	52.15	8.8	5077	5077	2	23.2	37.0	4.20	0
	03:25:00	205.00	43.35	52.15	8.8	5113	5113	2	23.4	36.0	4.09	0.2
	03:26:00	206.00	43.35	52.15	8.8	5150	5150	2	23.4	37.0	4.20	0
	03:27:00	207.00	43.35	52.15	8.8	5186	5186	2	23.5	36.0	4.09	0.1
	03:28:00	208.00	43.35	52.15	8.8	5223	5223	2	23.5	37.0	4.20	0
	03:29:00	209.00	43.35	52.15	8.8	5260	5260	2	24.1	37.0	4.20	0.6
	03:30:00	210.00	43.35	52.15	8.8	5297	5297	2	24.1	37.0	4.20	0
	03:31:00	211.00	43.35	52.15	8.8	5340	5340	2	24.1	43.0	4.89	0
	03:32:00	212.00	43.35	52.15	8.8	5371	5371	2.05	24.4	31.0	3.52	0.3
	03:33:00	213.00	43.35	52.15	8.8	5408	5408	2.05	24.6	37.0	4.20	0.2
	03:34:00	214.00	43.35	52.15	8.8	5442	5442	2.05	24.6	34.0	3.86	0
	03:35:00	215.00	43.35	52.15	8.8	5481	5481	2.05	24.6	39.0	4.43	0
	03:36:00	216.00	43.35	52.15	8.8	5518	5518	2.05	24.6	37.0	4.20	0
	03:37:00	217.00	43.35	52.15	8.8	5555	5555	2.05	24.6	37.0	4.20	0
	03:38:00	218.00	43.35	52.15	8.8	5591	5591	2.05	24.6	36.0	4.09	0
	03:39:00	219.00	43.35	52.15	8.8	5629	5629	2.05	24.6	38.0	4.32	0
	03:40:00	220.00	43.35	52.15	8.8	5663	5663	2.05	25.2	34.0	3.86	0.6
	03:41:00	221.00	43.35	52.15	8.8	5702	5702	2.05	26.1	39.0	4.43	0.9
	03:42:00	222.00	43.35	52.15	8.8	5737	5737	2.05	26.2	35.0	3.98	0.1
	03:43:00	223.00	43.35	52.15	8.8	5774	5774	2.05	26.3	37.0	4.20	0.1
	03:44:00	224.00	43.35	52.15	8.8	5811	5811	2.05	26.4	37.0	4.20	0.1
	03:45:00	225.00	43.35	52.15	8.8	5850	5850	2.05	26.6	39.0	4.43	0.2
	03:46:00	226.00	43.35	52.15	8.8	5885	5885	2.05	26.8	35.0	3.98	0.2
	03:47:00	227.00	43.35	52.15	8.8	5922	5922	2.05	27.2	37.0	4.20	0.4
	03:48:00	228.00	43.35	52.15	8.8	5960	5960	2.05	27.6	38.0	4.32	0.4
	03:49:00	229.00	43.35	52.15	8.8	5999	5999	2.05	27.6	39.0	4.43	0
	03:50:00	230.00	43.35	52.15	8.8	6034	6034	2.05	27.7	35.0	3.98	0.1
	03:51:00	231.00	43.35	52.15	8.8	6073	6073	2.05	27.7	39.0	4.43	0
	03:52:00	232.00	43.35	52.15	8.8	6110	6110	2.05	27.7	37.0	4.20	0
	03:53:00	233.00	43.35	52.15	8.8	6150	6150	2.05	27.7	40.0	4.55	0
	03:54:00	234.00	43.35	52.15	8.8	6188	6188	2.05	27.7	38.0	4.32	0
	03:55:00	235.00	43.35	52.15	8.8	6227	6227	2.05	27.7	39.0	4.43	0
	03:56:00	236.00	43.35	52.15	8.8	6267	6267	2.05	27.7	40.0	4.55	0
	03:57:00	237.00	43.35	52.15	8.8	6305	6305	2.05	27.7	38.0	4.32	0
	03:58:00	238.00	43.35	52.15	8.8	6347	6347	2.05	28	42.0	4.77	0.3
	03:59:00	239.00	43.35	52.15	8.8	6387	6387	2.05	28.5	40.0	4.55	0.5
	04:00:00	240.00	43.35	52.15	8.8	6427	6427	2.05	29.4	40.0	4.55	0.9
	04:01:00	241.00	43.35	52.15	8.8	6467	6467	2.1	30.3	40.0	4.55	0.9
	04:02:00	242.00	43.35	52.15	8.8	6505	6505	2.1	30.6	38.0	4.32	0.3
	04:03:00	243.00	43.35	52.15	8.8	6545	6545	2.1	31.4	40.0	4.55	0.8
	04:04:00	244.00	43.35	52.15	8.8	6587	6587	2.1	32.4	42.0	4.77	1
	04:05:00	245.00	43.35	52.15	8.8	6625	6625	2.1	33	38.0	4.32	0.6
	04:06:00	246.00	43.35	52.15	8.8	6667	6667	2.1	33.5	42.0	4.77	0.5
breakthrough	04:07:00	247.00	43.35	52.15	8.8	6708	6708	2.1	33.5	41.0	4.66	0
	04:08:00	248.00	43.35	52.15	8.8	6742	6742	2.1	33.5	34.0	3.86	0

04:09:00	249.00	43.35	52.15	8.8	6776	6776	2.1	33.5	34.0	3.86		0
04:10:00	250.00	43.35	52.15	8.8	6810	6810	2.1	33.5	34.0	3.86		0
04:11:00	251.00	43.35	52.15	8.8	6840	6840	2.1	33.5	30.0	3.41		0
04:12:00	252.00	43.35	52.15	8.8	6879	6879	2.1	33.5	39.0	4.43		0
04:13:00	253.00	43.35	52.15	8.8	6910	6910	2.1	33.5	31.0	3.52		0
04:14:00	254.00	43.35	51	7.65		0	2.1	33.5				0
04:15:00	255.00	43.35	51	7.65		0	2.1	33.5				0
04:16:00	256.00	43.35	51	7.65		0	2.1	33.5				0
04:17:00	257.00	43.35	51	7.65		0	2.1	33.5				0
04:18:00	258.00	43.35	51	7.65		0	2.1	33.5				0
04:19:00	259.00	43.35	50.8	7.45	7130	7130	2.1	33.5				0
04:20:00	260.00	43.35	50.8	7.45	7163	7163	2.1	33.5	33.0	4.43		0
04:21:00	261.00	43.35	50.8	7.45	7198	7198	2.1	33.5	35.0	4.70		0
04:22:00	262.00	43.35	50.8	7.45	7232	7232	2.1	33.5	34.0	4.56		0
04:23:00	263.00	43.35	50.8	7.45	7266	7266	2.1	33.5	34.0	4.56		0
04:24:00	264.00	43.35	50.8	7.45	7300	7300	2.1	33.5	34.0	4.56		0
04:25:00	265.00	43.35	50.8	7.45	7335	7335	2.1	33.5	35.0	4.70		0
04:26:00	266.00	43.35	50.8	7.45	7369	7369	2.1	33.5	34.0	4.56		0

Appendix G – Gradients of Experiment FPH – 235

G1. Measured data regarding the Shields parameter (Experiment FPH-235)

x-location tape measure (cm)	*d (mm)*	*R (mm)*	*A (mm^2)*	*P_{sensor}*	*Gradient (S_1)*	*τ_c (N/m^2)*	*Ψ_c*
9	0,84253	0,78111	13,5350	3 4	0,08	0,6130	0,22
13	0,62169	0,52414	10,6390	5 6	0,18	0,9255	0,33
15	0,64238	0,59886	12,7650	6 7	0,04	0,2350	0,08
17	0,59978	0,48316	7,5753	7 8	0,11	0,5214	0,18
19	0,52194	0,40161	8,5679	8 9	0,08	0,3152	0,11
21	0,46884	0,3956	10,4120	9 10	0,085	0,3299	0,12
23	0,40772	0,33191	6,4449	10 11	0,18	0,5861	0,21
25	0,22022	0,18478	3,5741	11 12	0,04	0,0725	0,03
27	0,50106	0,45805	9,1837	12 13	0,1	0,4493	0,16
29	0,35414	0,34142	4,6549	13	0,25	0,8373	0,29
31,5	0,21642	0,20416	2,6920	13	0,25	0,5007	0,18

Table G.1.1: Overview of obtained data for the Shields parameter (FPH-235).

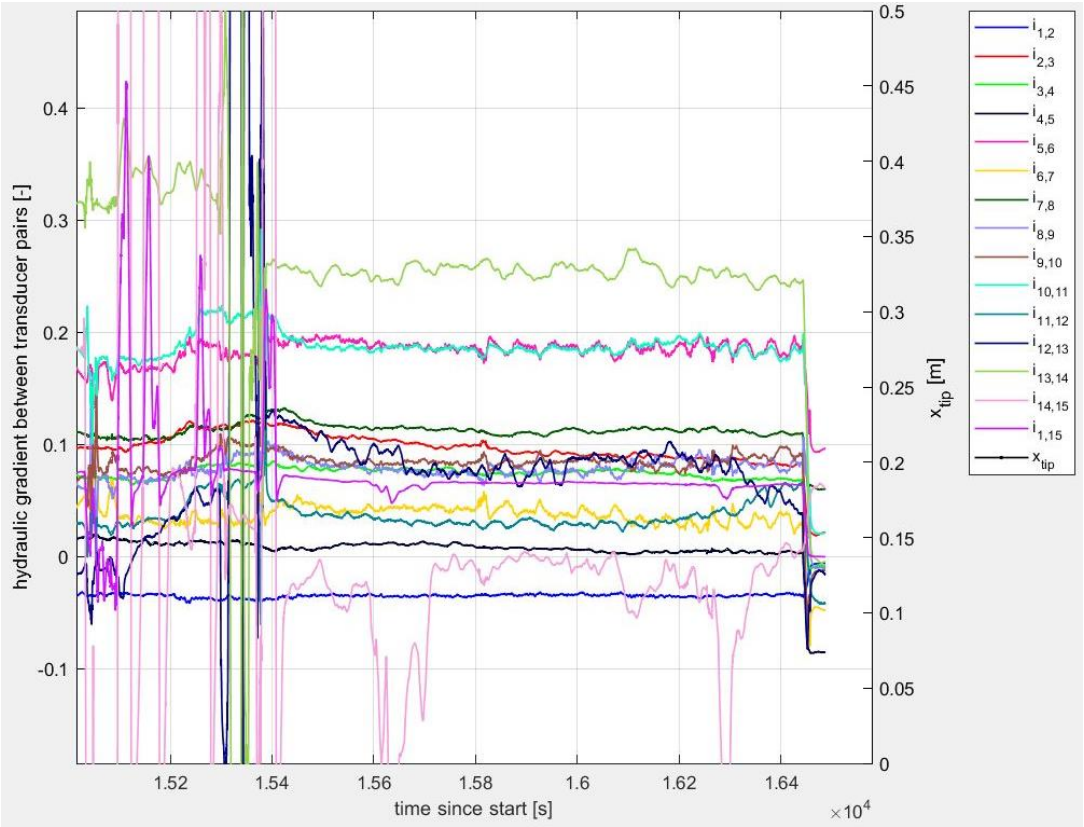

Figure G.1.1: Gradients (S_1) of the pressure sensors after breakthrough of the pipe (FPH-235).

G2. Passing gradients for the dilatancy calculation (FPH-235)

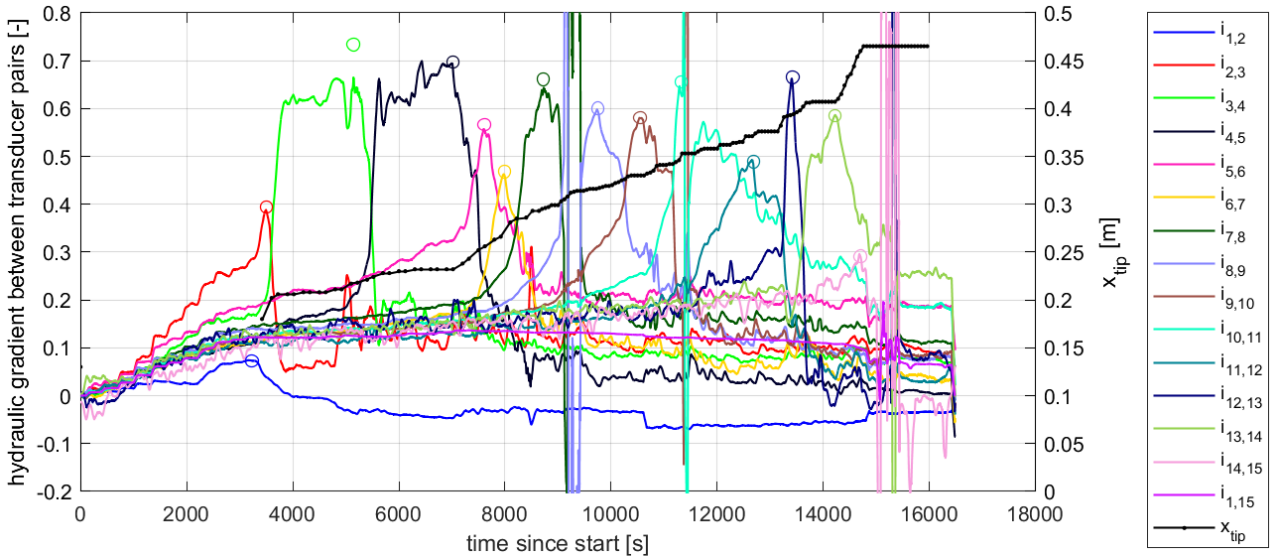

Figure G.2.1: Graphical presentation of the gradients during the experiment.

Transducer	Gradient	Passed? [0=no,1=yes]	Equilibrium [0=no,1=yes]	i_pipe [-] *(S)*	t_i_pipe [s]	i_tip [-] *(i_{loc})*	t_i_tip [s]
P3	i_3,4	1	1	0.164166	5688.6792	0.7334	5140.058
P4	i_4,5	1	1	0.076197	8549.3469	0.6972	7021.045
P5	i_5,6	1	0	0.215912	8719.1582	0.5665	7608.853
P8	i_8,9	1	0	0.13	11919	0.6001	9751.089
P9	i_9,10	1	0	0.131824	11919.448	0.5807	10547.9
P10	i_10,11	1	0	0.272833	13787.373	0.6558	11318.58

Table G.2.1: Overview of different gradients related to the position (P3-P10) (S and i_{loc}).

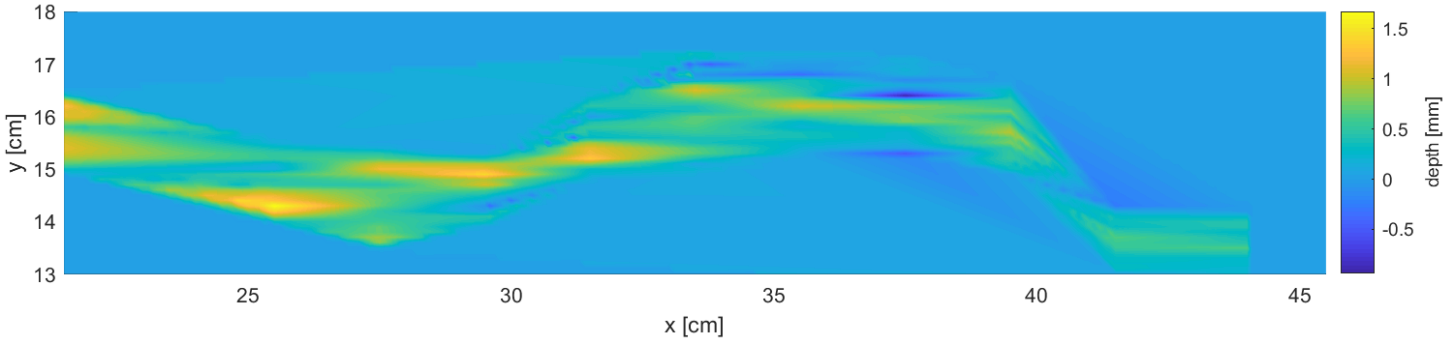

Figure G.2.2: Top view of the pipe (Experiment FPH-235).

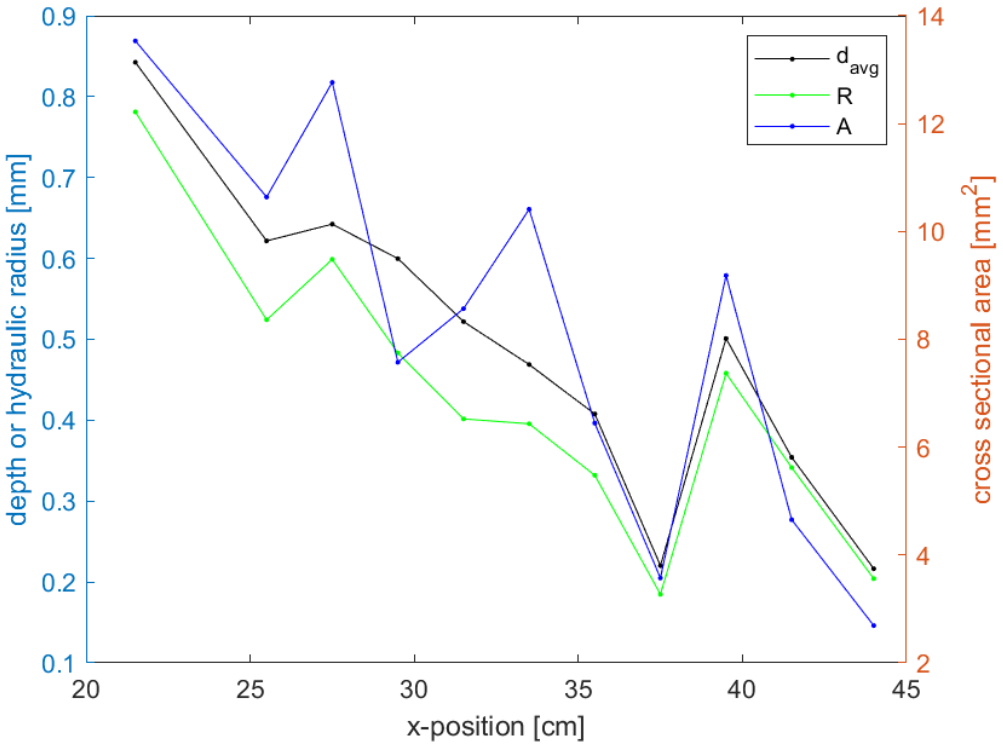

Figure G.2.3: Dimensions of the pipe for experiment FPH-235 (depth, hydraulic radius and cross-sectional area).

Lower and upper bound cross-sections of the pipe (experiment FPH-235)

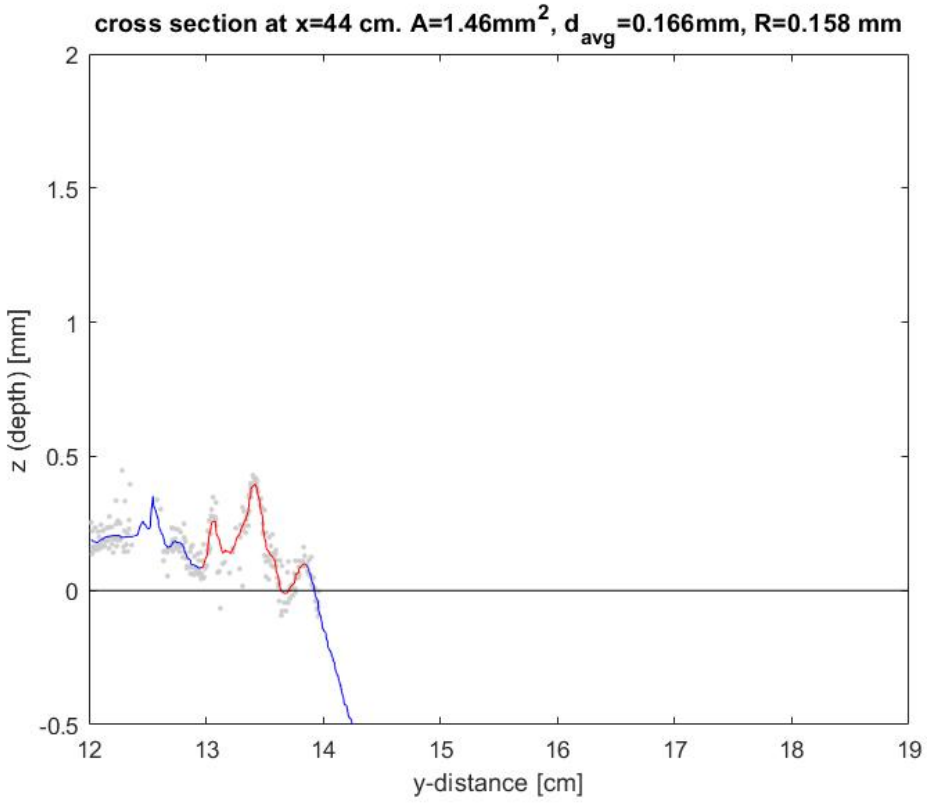

Figure G.2.4: Cross-section of the pipe at location x=44, Lower bound value FPH-235 (depth and hydraulic radius).

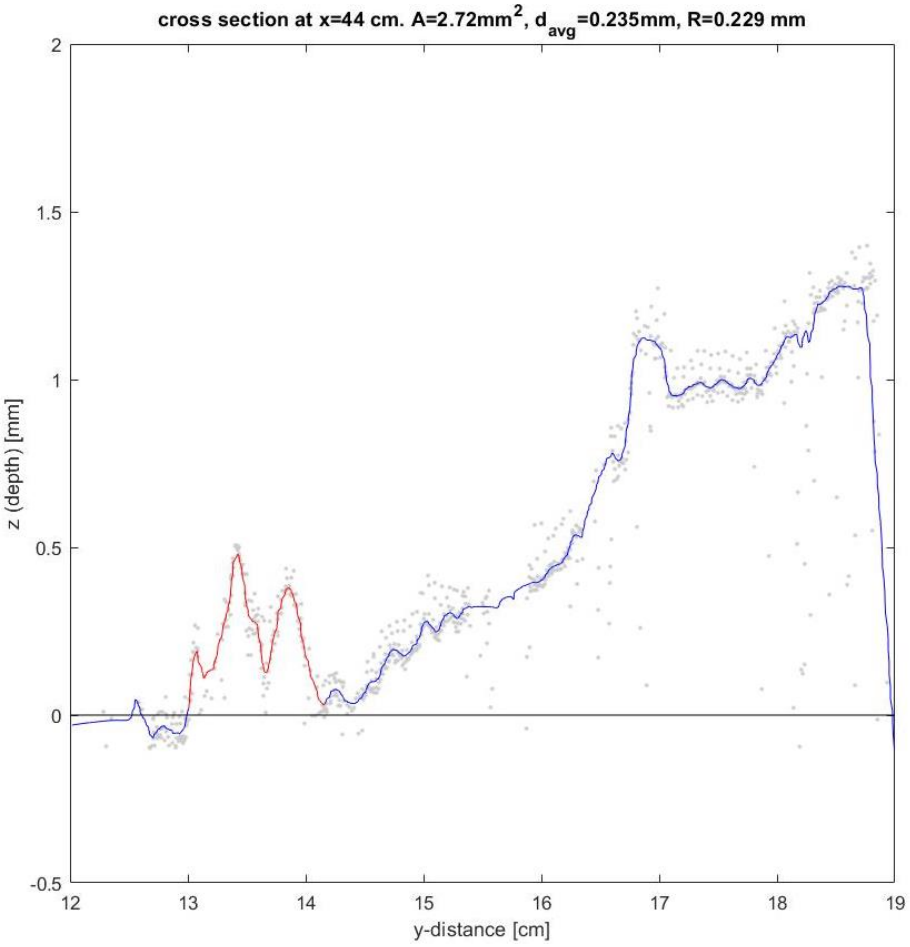

Figure G.2.5: Cross-section of the pipe at location x=44, Upper bound value FPH-235 (depth and hydraulic radius).

List of symbols

A =	Cross-section of the box (0.1 m * 0.3 m) (m^2)
a =	Horizontal distance from force till point of rotation (m)
b =	Distance from force till point of rotation (m)
C_F =	Drag coefficient of force F (-)
C_{Lane} =	Bligh factor (depending on the material)
D =	Aquifer thickness (m)
d_1 =	Thickness of the hinterland aquitard (m)
d =	Particle diameter (m)
$d_{pipe,tip}$ =	Depth at the tip of the pipe (m)
D_* =	Dimensionless particle diameter (-)
d_{50} =	50%-fractile of grain size distribution (m)
$d70$ =	70%-fractile of grain size distribution (m)
$d70_m$ =	Reference value for d_{70} in small-scale tests ($2.08*10^{-4}$ m)
e =	Void ratio (volume of voids/volume of solids) (Vv/Vs) or (n/(1-n))
F =	Resultant force (N)
g =	Acceleration of gravity (m/s^2)
ΔH =	Head difference
ΔH_c =	Critical head difference (m)
$\Delta H_{c,Sellmeijer}$ =	Critical head difference (m) calculated by model of Sellmeijer
$\Delta H_{c,measured}$ =	Measured critical head difference (m)
h =	Water level at the entry point (high water side) (m)
h_p =	Water level at exit point (low water side) (m)
i =	Gradient $(\Delta H/L)$
$i_{c,global}$ =	Global critical gradient $(\Delta H_c/(L-L_c))$ (-)
i_{loc} =	Local peak gradient (dh/dx) (i_tip) (-)
$i_{14,15}$ =	Gradient between sensor 14 & 15 (end of the pipe) (-)
k =	Hydraulic conductivity (m/s)
L =	Horizontal seepage length (m)
L_c =	Critical pipe length (cm)
L_h , L_v =	Seepage length (length of the erosion path vertical or horizontal)
m =	Mass of the sand crater(g)
n_{crater} =	Averaged porosity of the sand craters (-)
n_0 =	Initial Porosity (-)
n =	Porosity (volume of voids/total volume) (Vv/Vt) (-)
n_{max} =	Maximum porosity (-)
Q =	Discharge of water through the sample (m^3/s)
q =	Specific discharge $(k*i_{c,global})$ (m/s)
q_v =	Volumetric sediment transport rate per unit width (m^2/s)
$q_{v,C}$ =	Volumetric sediment transport rate per unit width (m^2/s) (Cheng)
$q_{v,C,adapted}$ =	Adapted volumetric sediment transport rate per unit width (m^2/s)
$q_{v,measured}$ =	Measured volumetric sediment transport rate per unit width (m^2/s)
$q_{v,\ total}$ =	Sediment transport rate (total) (g/min)
$q_{v,\ primary}$ =	Sediment transport rate (primary) (g/min)
$q_{v,\ secondary}$ =	Sediment transport rate (secondary) (g/min)
R =	Hydraulic radius (area/perimeter) (m)
RD =	Relative density $((e_{max}-e)/(e_{max} - e_{min}))$ (-)
RD_m =	Averaged relative density in small-scale tests (0,725)
r_b =	Outer radius of the sand boil (cm)

r_e =	Exit radius (0.3 cm)
r_c =	Edge radius of the crater (cm)
S =	Local slope of the pipe (i_pipe) (dh/dx) (-)
S_1 =	Local slope after breakthrough of the pipe (dh/dx) (-)
T_{day} =	Time in seconds in a day (s) = 86400
$T_{progression}$ =	Time of the progression phase (min)
U_b =	Flow velocity (m/s)
u_* =	Shear velocity (m/s)
$u*_c$ =	Critical shear velocity (m/s)
V =	Volume of the sand crater (cm^3)
V_{wal} =	Wall velocity (m/s)
$V_{wal,avg}$ =	Averaged wall velocity (m/s)
$v_{c,avg}$ =	Averaged progression rate *($(L-L_c)/(Tprogression)$)* (m/s) (measured)
$v_{prediction}$ =	Predicted progression rate (m/s)
$v_{progression}$ =	Progression rate velocity (m/s) (Cheng)
w =	Width at the tip of the pipe (m)

α =	Particle/eccentricity coefficient (-)
α_0 =	Outer slope (°)
α_i =	Inner slope (°)
Δ =	Relative density *($=(\rho_s-\rho_w)/\rho_w$)* (-)
γ'_p =	Submerged volumetric weight sand (kN/m^3)
γ_w =	Volumetric weight water (kN/m^3)
Ψ_c =	Critical Shields parameter (-)
Ψ =	Shields parameter (-)
θ_1 =	Angle of repose (°)
θ =	Bedding angle (°)
κ =	Intrinsic permeability of the aquifer (m^2)
η =	Constant of white (-)
Φ =	Bedload transport rate (-)
$\Phi_{calculated}$ =	Calculated bedload transport rate (Cheng adapted formula) (-)
$\Phi_{measured}$ =	Bedload transport rate from measured progression rate (FPH-235) (-)
ρ_s =	Particle density (kg/m^3)
ρ_w =	Density of water (kg/m^3)
ν =	Kinematic viscosity ($=\mu/\rho$) (m^2/s)
τ_c =	Critical shear stress (N/m^2)
τ =	Bed shear stress (N/m^2)

List of figures

Figure 1.1: Overview of the piping mechanism. 1
Figure 1.2: Overview of the methodology. 3
Figure 1.3: Flowchart of the different experimental series. 4
Figure 2.1: Schematic overview of the most common failure mechanisms (TAW, 1998). 6
Figure 2.2: Sand boil in a ditch (TAW, 1994). 7
Figure 2.3: The different phases of piping (Van Beek, 2015). 7
Figure 2.4: Sand boil without soil particles (l), Sand boil with soil particles (r) (Vandenboer, 2018). .. 8
Figure 2.5: Dike breach in the IJkdijk experiments (Van Beek et al., 2011). 9
Figure 2.6: The mud fountain as observed at the location of the sand boil, Zalk 1926 (Van Beek et al, 2011). 10
Figure 2.7: Observations of piping boils in the Netherlands (Zwang & Bos, 2009). 11
Figure 2.8: Schematization of Bligh's rule (Jonkman et al., 2017). 12
Figure 2.9: Schematization of Lane's rule (Förster et al., 2012). 13
Figure 2.10: Schematization of the model of Sellmeijer (Sellmeijer, 1989). 14
Figure 2.11: Equilibrium head difference as a function of the l/L ratio (Förster et al., 2012). 14
Figure 2.12: Dimensions of experimental tubes and locations of pressure transducers (Robbins et al., 2017). 17
Figure 2.13: Photograph of experimental set-up (Robbins et al., 2017). 17
Figure 2.14: Relation between maximum Darcy velocity and progression rate (Robbins et al., 2017). 18
Figure 2.15: Pipe development velocity as a function of different void ratio's (Robbins et al., 2017). 18
Figure 2.16: Medium-scale flume set-up (Allan, 2018). 19
Figure 2.17: Tip progression speed with applied head difference above critical loading (Allan, 2018). 20
Figure 2.18: Set-up for small-scale experiments (Vandenboer, 2018). 21
Figure 2.19: Top view of the small-scale box filled with sand (l), Overview of the full experimental set-up (r) (Vandenboer, 2018). 21
Figure 2.20: Progression rate of the pipe related to the applied ratio (Vandenboer, 2018). 22
Figure 2.21: Process of particle transport for backward erosion piping (Vandenboer, 2018). 24
Figure 2.22: Forces acting on a particle on the bed (Jansen, 1979). 24
Figure 2.23: Shields curve (Vanoni et al., 2006). 26
Figure 2.24: The 7 stages of motion presented in the Shields diagram (Schiereck, 2012). 27
Figure 2.25: Equilibrium of forces on a soil particle (White, 1940). 28
Figure 2.26: Shields diagram for laminar and turbulent flows (Hoffmans et al., 2018). 29
Figure 2.27: Shields parameter related to the particle Reynolds number for laminar flow (Van Beek et al., 2019). 30
Figure 2.28: Slope failure due to horizontal gradient (Allan, 2018). 31
Figure 2.29: Mechanism of the vertical gradient (Allan, 2018). 31
Figure 2.30: Dilatancy principle change in volume (Acsess library: Soil survey horizons, 2015). 32
Figure 2.31: Comparison of predicted and measured dimensionless transport rate (Cheng, 2004). 34
Figure 2.32: Schematization of the processes governing the progression of the pipe (Van Beek, 2015). 34
Figure 2.33: Influence chart of the different parameters. 36
Figure 2.34: Experimental setup (Pol et al., 2019). 37
Figure 3.1: Cross-section of the experimental setup with the cylinder placed on top (Van Beek, 2015). 39

Figure 3.2: Photograph of the experimental setup filled with sand (Photographed by Van Klaveren, 2019)..... 40
Figure 3.3: Schematisation of the water flow through the setup (Van Beek, 2015)..... 40
Figure 3.4: Outflow point of the experimental setup (Photographed by Van Klaveren, 2019)..... 41
Figure 3.5: Sprinkling of the sand grains into the box (l), Filled setup with the lid on top (r) (Photographed by Van Klaveren, 2019)..... 42
Figure 3.6: Box filled with sand and placed horizontally (Photographed by Van Klaveren, 2019)..... 43
Figure 3.7: Laser triangulation principle (Azosensors, 2014)..... 43
Figure 3.8: Experimental setup including measuring equipment (lights, cameras, scale, laser including frame) (Photographed by Van Klaveren, 2019)..... 44
Figure 3.9: Top view of the pipe without filter cloths in the middle (Experiment B25-221)..... 47
Figure 3.10: Schematization of the acrylate plate including two filter cloths and 19 pressure sensors (Drawn by Pol)..... 48
Figure 3.11: Development of the pipe length related to the head difference (B25-229)..... 50
Figure 3.12: Top view including the location of the pressure sensors (bottom metal strip)..... 51
Figure 3.13: Measured head difference by the pressure sensors (B25-229)..... 51
Figure 3.14: Hydraulic gradient between two transducers (B25-229)..... 52
Figure 3.15: Example of measured head difference (l) and hydraulic gradient for 2 sensors (r)..... 52
Figure 3.16: Hydraulic gradient between two transducers (B25-232)..... 53
Figure 3.17: Cross-section of the pipe at location x=25.5 (l) and x=35.5 (r)..... 53
Figure 3.18: Area, depth, and hydraulic radius of the pipe related to the location (B25-229)..... 54
Figure 3.19: Top view of the pipe with a depth profile (B25-229)..... 54
Figure 3.20: Start of the dye injection (B25-229)..... 55
Figure 3.21: Dye injection after 3 seconds (B25-229)..... 55
Figure 3.22: Top view of the sand boil inside the cylinder (B25-229)..... 56
Figure 4.1: Overview of the analysis scheme..... 59
Figure 4.2: Progression rate versus global critical gradient..... 61
Figure 4.3: Progression rate versus hydraulic conductivity (k)..... 62
Figure 4.4: Critical pipe length versus critical hydraulic head..... 63
Figure 4.5: Progression rate versus porosity (n)..... 63
Figure 4.6: Progression rate versus specific discharge..... 64
Figure 4.7: Schematic cross-section of the sand boil (Vandenboer, 2018)..... 65
Figure 4.8: Top view of the sand boil (Outer radius = 2.1 cm)..... 66
Figure 4.9: Development of the crater over time (Experiment FPH-235)..... 67
Figure 4.10: Local hydraulic gradient versus the hydraulic radius of experiment FPH-235..... 69
Figure 4.11: Shields diagram including experimental results FPH-235..... 70
Figure 4.12: Calculated and measured dimensionless transport rate of experiment FPH-235 (Cheng, 2004)..... 73
Figure 4.13: Top view of the pipe development (Experiment FPH-235)..... 74
Figure 4.14: Wall velocity for the six pressure sensors (experiment FPH-235)..... 75
Figure 4.15: Schematization of the wall velocity for fine sand (De Groot et al., 2009)..... 76
Figure 4.16: Progression rate versus global critical gradient (Baskarp B25)..... 78
Figure 5.1: Flood wave from 1995 in the Netherlands (Lecture notes CTB3350)..... 81
Figure 6.1: Linear relation for the hydraulic conductivity and progression rate..... 85
Figure C.2.1: Development of the head difference versus the pipe length (B25-229)..... 95
Figure C.2.2: Development of the head difference versus the change in slope (B25-229)..... 96
Figure C.2.3: Change in slope of the progression rate [cm/min] versus time (B25-229)..... 96
Figure C.2 4: The flow rate [ml/min] versus the head difference (B25-229)..... 97
Figure C.2.5: Development of the flow rate over time (B25-229)..... 97
Figure E.1: Schematic cross-section of the crater..... 102
Figure G.1.1: Gradients (S_1) of the pressure sensors after breakthrough of the pipe (FPH-235)..... 104

Figure G.2.1: Graphical presentation of the gradients during the experiment. 105
Figure G.2.2: Top view of the pipe (Experiment FPH-235) 105
Figure G.2.3: Dimensions of the pipe for experiment FPH-235 (depth, hydraulic radius and cross-sectional area).....106
Figure G.2.4: Cross-section of the pipe at location x=44, Lower bound value FPH-235 (depth and hydraulic radius).....106
Figure G.2.5: Cross-section of the pipe at location x=44, Upper bound value FPH-235 (depth and hydraulic radius).....107

List of tables

Table 2.1: C_{Bligh} factor related to foundation material (Vandenboer, 2018). 12
Table 2.2: C_{Lane} factor related to foundation material (Vandenboer, 2018). 13
Table 2.3: Overview of performed experiments related to the progression rate (Van Beek, 2015). 16
Table 2.4: Results of the experiments above critical loading (Allan, 2018). 20
Table 2.5: Overview experiments with supercritical hydraulic loads (Vandenboer, 2018). 22
Table 2.6: Overview of different types of particles in laminar flow (Van Beek et al., 2019). 29
Table 2.7: Parameters categorized by group. 35
Table 2.8: Overview of expected effects for the different parameters. 36
Table 3.1: Overview of the first set of experiments: Comparing different configurations of the setup. 45
Table 3.2: Overview of the second set of experiments: Comparing different sand properties. 46
Table 3.3: Overview of the third series of experiments: Effect of hydraulic loading. 46
Table 3.4: Overview of used sand types. 46
Table 4.1: Overview of the performed experiments. 60
Table 4.2: Overview of the different critical head values. 65
Table 4.3: Results of the $q_{v,\ primary}$ calculation. 68
Table 4.4: Calculation of the sediment transport and progression rate (Equation 2.24, 4.9 to 4.13). 72
Table 4.5: Range of local pipe gradients (Experiment FPH-235 after passing of the pipe). 73
Table 4.6: Gradients of the six pressure sensors of experiment FPH-235. 74
Table 4.7: Parameters for the dilatancy calculation (FPH-235). 75
Table 4.8: Observed relations from measured results (for three types of sand). 77
Table 4.9: Comparison of the hypothesis and measured results (all experiments). 77
Table 5.1: Results of the $T_{progression}$ calculation for a real dike. 81
Table 6.1: Overview of main parameters influencing the progression rate. 83
Table E.1: Overview of the measured data for all experiments. 102
Table G.1.1: Overview of obtained data for the Shields parameter (FPH-235). 104
Table G.2.1: Overview of different gradients related to the position (P3-P10) (S and i_{loc}) 105